

**Autoinhibition and Chloride Sensing
in the WNK1 Kinase**

APPROVED BY SUPERVISORY COMMITTEE

Elizabeth Goldsmith, Ph.D., Supervisor

Luke Rice, Ph.D., Chair

Melanie Cobb, Ph.D.

Chad Brautigam, Ph.D.

To my wife, my parents, and my late father.

Autoinhibition and Chloride Sensing
in the WNK1 Kinase

by

Thomas Matthew Moon

DISSERTATION

Presented to the Faculty of the Graduate School of Biomedical Sciences

The University of Texas Southwestern Medical Center at Dallas

in Partial Fulfillment of the Requirements

for the Degree of

DOCTOR OF PHILOSOPHY

The University of Texas Southwestern Medical Center at Dallas

Dallas, TX

April 2012

Copyright

by

Thomas Matthew Moon, 2012

Autoinhibition and Chloride Sensing in the WNK1 Kinase

Thomas Matthew Moon, Ph.D.

The University of Texas Southwestern Medical Center at Dallas, 2012

Elizabeth Goldsmith, Ph.D.

Protein kinases control diverse cellular pathways and have are the subject of intensive study regarding how they maintain specificity toward substrates. The research presented here focuses on a 230kDa serine/threonine protein kinase known as WNK1 (with no lysine {k}). The protein was first cloned by Melanie Cobb's laboratory, and its isoforms have been associated with a monogenic form of hypertension as well as with breast and prostate cancer. Recent data have also shown that WNK1 is necessary for maintaining spindle polarity in mitosis and plays a role in post-mitotic abscission. The function of WNK1 is most commonly associated with the regulation of CCCs via the activation of the WNK1 substrates OSR/SPAK. Prior investigation of the system has demonstrated that CCCs are activated by increasing concentrations of extracellular salt and by intracellular phosphorylation from the OSR/SPAK kinases. Due to its ubiquity in mammalian cell types, a question has arisen as to how the pathway responds to changes in osmolarity. Further,

because of the involvement of WNK1 in a diverse set of cellular mechanisms, how is WNK1 activity and substrate specificity controlled?

An autoinhibitory domain of WNK1 was characterized by the Cobb Lab regarding its ability to inhibit the kinase *in cis* and *in trans*. In this study, we find that the solution structure of the autoinhibitory domain retains a conserved RFXV binding site from the PASK/FRAY homology 2 (PF2) domain present in OSR/SPAK. Titration data shows that incubation with a 5-mer and a 20-mer peptide derived from the WNK1 kinase domain displays extensive chemical shift perturbation as assessed by $^1\text{H},^{15}\text{N}$ -HSQC.

Expression of this autoinhibitory domain *in cis* with the WNK1 kinase domain followed by size-exclusion chromatography shows substantial conformational changes when dialyzed from high to low salt. A measurement of the activity of the WNK1 kinase domain in the presence of increasing amounts of sodium chloride indicate an IC_{50} of 130mM. Further biophysical investigation using differential scanning fluorimetry with the kinase domain shows that the domain undergoes substantial increases in domain stabilization as the concentration of salt is increased. Continued analysis of this phenomena has pointed toward evidence of anion sensing by the WNK1 kinase domain. Other protein kinases studied in our lab do not exhibit this salt sensitivity.

To determine the binding site of chloride in the WNK1 kinase domain, the inactive WNK1 kinase was cocrystallized in the presence of sodium bromide. A dataset was collected using the bromine anomalous edge (0.92 Å). The anomalous difference fourier map was calculated and a 5.2 σ peak was

observed at the N-terminus of the 3.10 helix present in the DLG motif of the activation loop. To corroborate these data, the structure of the inactive kinase domain previously crystallized in sodium chloride was re-refined. A similar binding site corroborated by a $2mF_o - DF_c$ peak of 5.5σ was observed in subunit A near the N-terminus of the 3.10 helix. When the structure was refined in with a chloride ion placed in the observed density, similar hydrogen bonding interactions between the amide backbone and the chloride ion were observed compared to that in the bromide-soaked structure. The presence of this chloride ion appears to favor sequestration of E268 in α C and R348 in the catalytic loop and promotes an inactive kinase structure.

Finally, the crystal structure of the activated WNK1 kinase domain was determined under low-salt conditions. The term 'activated' and not active is used to describe this structure of the WNK1 kinase domain because, although it is phosphorylated at S378 and S382 in the activation-loop during expression, the structure adopts an inactive conformation due to the placement E268 in helix C. The structure displays disorder of many key structural elements such as the N-terminus of α C. A key observation is the lack of a 3.10 helix in the N-terminus of the activation loop and the lack of water or any atom that could be chloride near the amide backbone near the chloride binding site.

Based upon the literature surrounding the activation of WNK1 and the data presented in this thesis, we predict a three-tiered regulation of WNK1 driven by a) autophosphorylation b) chloride binding and c) autoinhibitory domain occlusion of the nucleotide and/or docking interfaces present in the

WNK1 kinase domain. The coupling of the information that we have gathered on the autoinhibitory and kinase domains appear to point to an overall mechanism of salt sensing and self-contained signaling control in the WNK1 kinase cascade.

Table of Contents

Abstract	v
List of Tables	xiii
List of Figures	xiv
List of Abbreviations	xvii
Chapter 1. Introduction	1
1.1 The WNK1 Protein Kinase	2
1.2 WNK1 Biochemical Pathway Involvement	13
1.2.1 NKCC Regulation	13
1.2.2 Responses to Changes in Osmolarity	18
1.2.3 Incompletely Characterized Functions	21
1.3 Description of Dissertation Research	24
Chapter 2. Expression and Purification of the WNK1 Autoinhibitory Domain	26
2.1 Introduction	26
2.2 Bioinformatic analysis of the WNK1 autoinhibitory domains	27
2.2.1 Sequence alignment	27
2.2.2 Secondary and tertiary structure prediction	28
2.2.3 Discussion	28
2.3 Construct design	30
2.4 Expression	31
2.4.1 Expression Trials	31
2.4.2 Uniform ^{13}C , ^{15}N labeling in M9 minimal media	34
2.5 Purification	35
2.6 Materials	39

Chapter 3. NMR Data Collection and Structure Calculation of the WNK1 Autoinhibitory Domain	40
3.1 Introduction	40
3.2 Theory	40
3.2.1 Spin	40
3.2.2 A single pulse experiment	43
3.2.3 The chemical shift	47
3.2.4 Many spin systems	48
3.2.5 3D experiments for backbone and sidechain assignments	52
3.3 Materials and Methods	61
3.3.1 Data collection and manipulation	61
3.3.2 Structure calculation	64
Chapter 4. Solution Structure and Biochemical Characterization of the WNK1 Autoinhibitory Domain	66
4.1 Introduction	66
4.2 Results	67
4.2.1 Bioinformatic approach	67
4.2.2 NMR data collection and the solution structure of the WNK1 autoinhibitory domain	71
4.2.3 The autoinhibitory domain interaction with RFXV motifs	75
4.3 Discussion	83
Chapter 5. Expression, Purification and Crystallization of the Active WNK1 Kinase Domain	90
5.1 Introduction	90
5.2 Expression	90
5.3 Purification	91
5.3.1 Materials	94
5.4 Crystallization of WNK1 (209-483 S378* S378*)	95

Chapter 6. Structure Determination and Analysis of the Activated WNK1 Kinase Domain	100
6.1 Theory	100
6.1.1 Diffraction by crystalline substances	100
6.1.2 The phase problem	102
6.2 Data Collection	102
6.2.1 Map Calculation	106
6.2.2 Model Building and Refinement	107
6.3 Structure of the activated WNK1 kinase domain	108
6.3.1 General topology	108
6.3.2 The active site	116
6.3.3 Comparison to the inactive kinase domain	116
6.3.4 Comparison of WNK1 Kinase Domain Structures to Active PKA	119
Chapter 7. Biochemical and Biophysical Analysis of the WNK1 Kinase Domain	123
7.1 Biochemical analysis of the WNK1 kinase	124
7.1.1 Mass spectrometry analysis of the WNK1 kinase domain and associated mutants	124
7.1.2 Activity assays of the WNK1 kinase domain	128
7.2 Biophysical analysis of the WNK1 kinase domain by Differential Scanning Fluorimetry	130
7.3 Discussion	135
7.4 Experimental design and protocol	139
7.4.1 Mass spectrometry	139
7.4.2 Activity assays	139
7.4.3 Differential scanning fluorimetry	143
7.4.4 Expression and purification of WNK1 constructs	145
Chapter 8. Structure Determination and Analysis of the placement of Chloride in the Inactive WNK1 Kinase Domain	149
8.1 Introduction	149
8.2 Cocrystallization of WNK1 194-483 S382A, in sodium bromide	150

8.2.1	Expression	150
8.2.2	Purification of WNK1 194-483 S382A	150
8.2.3	Crystallization of WNK1 194-483 S382 in NaBr	151
8.3	Data Collection	152
8.3.1	Map Calculation and Refinement	153
8.4	Structure of the mutant, inactive WNK1 kinase domain bound to Bromide	156
8.5	Discussion	162
Chapter 9.	Discussion	167
9.1	A mechanism of salt sensing by the WNK1 kinase domain	167
9.2	The chloride ion sensor WNK1 acts as a negative feedback loop regulator in cells	168
9.2.1	How WNK1 may act to control chloride levels in cellular environments	170
9.3	Inhibition by the WNK1 autoinhibitory domain may be linked to the salt sensitivity of the kinase domain	174
9.4	Future directions for investigation of the WNK family of protein kinases	178
9.4.1	Short-term goals addressing the chloride-sensitivity of the WNK1 kinase domain	180
9.4.2	Long-term goals	181
Appendices		183
Appendix A.	Supplementary Figures for Chapter 1	184
Appendix B.	Supplementary Figures for Chapter 4	186
Appendix C.	Supplementary Figures for Chapter 8	189
Appendix D.	Supplementary Figures for Chapter 9	190
Bibliography		191

List of Tables

2.1	PCR Protocol for WNK1 (480-572)	30
2.2	Digest of WNK (480-572) and pHis-Parallel (empty)	32
2.3	Ligation of WNK (480-572) and pHis-Parallel (empty)	32
2.4	Buffers for Purification of WNK1 (480-572)	39
5.1	Buffers for Purification of WNK1 (209-483)	94
5.2	WNK1 (209-483) PEG Screen	99
6.1	Data collection and Refinement Statistics for WNK1 (209-483)	109
7.1	Protocol for activity assays of the WNK1 kinase domain	144
7.2	Protocol for DSF of the WNK1 kinase domain	146
8.1	Data collection and Refinement Statistics for WNK1 (194-483 S382A)	155
A.1	WNK1 pHis-parallel Plasmids: X. Min Inventory c. 2004	185
B.1	Table of Statistics for Structure Calculation of WNK1 (480-572)	188

List of Figures

1.1	Lysine exchange	4
1.2	Autoinhibition of WNK1 a) <i>in cis</i> and b) <i>in trans</i>	6
1.3	Phosphorylation state of the WNK1 kinase	8
1.4	Crystal structure of the mutant, inactive WNK1 kinase domain	10
1.5	Structural comparison of monomers in the ASU of the mutant, inactive WNK1 kinase domain	11
1.6	Structure of the OSR-PF2 domain	17
2.1	Sequence Alignment of WNK Autoinhibitory Domains with OSR- PF2 Domains	29
2.2	Ni ²⁺ -sepharose of U- ¹³ C, ¹⁵ N-WNK1 (480-572)	36
2.3	MonoQ of U- ¹³ C, ¹⁵ N-WNK1 (480-572)	36
2.4	Superdex 75 (16/60) of U- ¹³ C, ¹⁵ N-WNK1 (480-572)	37
3.1	Graphic display of a one pulse experiment	44
3.2	Energy levels in a 2-spin coupled system	50
3.3	General outline of a multidimensional experiment	50
3.4	Outline of a ¹ H, ¹⁵ N-HSQC experiment	50
3.5	HNCACB of U- ¹⁵ N, ¹³ C-WNK1 (480-572)	53
3.6	CBCA(CO)NH of U- ¹⁵ N, ¹³ C-WNK1 (480-572)	54
3.7	Sample connectivity for backbone assignment of U- ¹⁵ N, ¹³ C-WNK1 (480-572)	57
3.8	(H)C(CO)NH-TOCSY of U- ¹⁵ N, ¹³ C-WNK1 (480-572)	58
3.9	H(CCO)NH-TOCSY of U- ¹⁵ N, ¹³ C-WNK1 (480-572)	59
3.10	HCCH-TOCSY of U- ¹⁵ N, ¹³ C-WNK1 (480-572)	60
3.11	¹⁵ N-NOESY of U- ¹⁵ N, ¹³ C-WNK1 (480-572)	62
3.12	¹³ C-NOESY of U- ¹⁵ N, ¹³ C-WNK1 (480-572)	63
4.1	WNK1 (480-572) Sequence Alignment and Analysis	69

4.2	$^1\text{H}, ^{15}\text{N}$ -HSQC of WNK1 (480-572)	72
4.3	Solution structure of WNK1 (480-572)	73
4.4	Structure comparison of WNK1 (480-572) and OSR-PF2	76
4.5	$^1\text{H}, ^{15}\text{N}$ -HSQC of WNK1 (480-572) titrated with 5-mer peptide	78
4.6	$\Delta\delta$ ppm by residue number from figure 4.5	79
4.7	$^1\text{H}, ^{15}\text{N}$ -HSQC of WNK1 (480-572) titrated with 20-mer peptide	81
4.8	$^1\text{H}, ^{15}\text{N}$ -HSQC of WNK1 (480-572) titrated with 19-mer peptide	82
4.9	Structural alignment of calculated and solution structure of WNK1-AI	85
4.10	$\beta 3/\alpha B$ interaction in the OSR-PF2 domain	88
4.11	$\beta 1/\alpha B$ interaction in the WNK1-AI domain	89
5.1	Ni^{2+} -sepharose of WNK1 (209-483 S378* S382*)	92
5.2	MonoQ of WNK1 (209-483 S378* S382*)	93
5.3	Superdex 75 (16/60) of WNK1 (209-483 S378* S382*)	93
5.4	Initial crystallization of WNK1 (209-483 S378* S382*)	97
5.5	Crystallization of WNK1 (209-483 S378* S382*) (KH_2PO_4)	98
6.1	Diffraction Pattern of WNK1 (209-483 S378* S382*)	104
6.2	Crystal scaling and integration data	105
6.3	Refinement plot for WNK1 (209-483 S378* S382*)	108
6.4	Ramachandran map for WNK1 (209-483 S378*, S382*)	110
6.5	Crystal structure of the activated WNK1 kinase domain	113
6.6	Crystal packing for the activated WNK1 kinase domain	114
6.7	Phosphate interaction with $\alpha E/\alpha I$ in C-terminus	115
6.8	Active site of the activated WNK1 kinase domain	117
6.9	Comparison of the activated WNK1 kinase domain to the mutant, inactive structure	120
6.10	Comparison of the structure of the WNK1 kinase domain to Active PKA	121
7.1	ESI/MS of WNK1 194-483	125
7.2	ESI/MS of WNK1 194-483 S378D	126
7.3	ESI/MS of WNK1 194-483 S382D	127

7.4	WNK1 kinase (194-483) activity while titrated with WNK1 (480-572)	129
7.5	WNK1 kinase (194-483) activity while titrated with NaCl	130
7.6	DSF raw data curves of WNK1 kinase domain while titrated with NaCl	133
7.7	DSF curve of WNK1 kinase domain while titrated with NaCl	134
7.8	DSF curve of WNK1 and MAP kinases titrated with NaCl	136
7.9	DSF curve of WNK1 kinase domain titrated with different salts	137
7.10	Raw sample activity data for WNK1 194-483	142
8.1	Diffraction Pattern for WNK1 194-483 S382A in NaBr	154
8.2	Structure of bromide-bound WNK1 194-483 S382A	157
8.3	Binding site of bromide and chloride	159
8.4	Comparison of 2.8 Å to 1.8 Å structure	160
8.5	Comparison of the activated structure of the WNK1 kinase domain with the inactive, chloride bound form	164
8.6	Comparison of the activated and chloride-bound WNK1 kinase domain structures to active PKA	165
9.1	Proposed mechanism of cell volume regulation by the putative chloride sensor, WNK1	172
9.2	Model of allosteric linkage of the autoinhibitory domain to the kinase domain under the control of sodium chloride concentration	179
B.1	MALLS of U ¹³ C, ¹⁵ N-WNK1-(480-572)	186
B.2	Negative titration controls for WNK1 (480-572)	187
C.1	Comparison of 3.10 helices in subunit A and B from structure solved by Min et al (2004)	189
D.1	Size exclusion chromatography of WNK1 194-573 WT and S378A mutant	190

List of Abbreviations

Å	Angstrom
ATP	Adenosine-Triphosphate
WNK	With No Lysine (K) protein kinase
OSR	Oxidative Stress Responsive protein kinase
SPAK	Serine/threonine Proline-Alanine rich protein Kinase
CCC	Cation Chloride Cotransporter
RFXV	Arg - Phe - Xxx - Val
PHAI	Pseudohypoaldosteronism type II
MAPK	Mitogen-Activating Protein Kinase
ERK2	Extracellular signal-Regulated Kinase 2
MBP	Myelin Basic Protein
HEK	Human Embryonic Kidney cell line
<i>E. coli</i>	<i>Escherichia coli</i>
GST	Glutathione S-transferase
SDS-PAGE	Sodium Dodecyl Sulfate-Polyacrylamide Gel Electrophoresis
HEPES	4-(2-hydroxyethyl)-1-piperazineethanesulfonic acid
RMSD	Root mean square deviation
PKA	Protein Kinase A
DCT	Distal convoluted tubule
PP1	Protein Phosphatase 1
JNK	c-Jun N-terminal Kinase
MALDI-TOF	Matrix-assisted laser desorption ionization, time-of-flight mass-spectrometry
LPA	Lipophosphatidic acid
EGF	Epidermal growth factor
GFP	Green fluorescent protein
ROMK	Renal outer-medullary potassium channel
SNARE	Soluble NSF Attachment Protein Receptor
CFTR	Cystic Fibrosis Transmembrane Conductance Regulator
NMR	Nuclear Magnetic Resonance spectroscopy
PCR	Polymerase Chain Reaction
LB	Luria Broth

IPTG	Isopropyl β -D-1-thiogalactopyranoside
TEV	Tobacco Etch Virus
Tris	Tris(hydroxymethyl)aminomethane
EDTA	Ethylene diamine tetra-acetic acid
RF	Radio frequency
HSQC	Heteronuclear Single Quantum Coherence
INEPT	Insensitive Nuclei enhanced by Polarization Transfer
TOCSY	Total Correlation Spectroscopy
NOESY	Nuclear Overhauser Effect Spectroscopy
MALLS	Multi-angle laser light scattering
PEG	Polyethylene glycol
MR	Molecular replacement
TLS	Translation, libration and screw
T_m	Midpoint unfolding temperature
IC₅₀	Half maximal inhibitory concentration
HPLC	High performance liquid chromatography
ESI/MS	Electrospray ionization mass spectrometry
DSF	Differential scanning fluorimetry
TAO2	Thousand And One kinase isoform 2
BSA	Bovine Serum Albumin
cAMP	Cyclic adenosine monophosphate
MWCO	Molecular weight cutoff
WSP	WNK-specific PF2 domain
WASP/WAVE	Wiskott-Aldrich Syndrome Associated Proteins

Chapter 1

Introduction

Protein kinases are signal transduction machines that transmit information using chemical modification of the amino acids serine, threonine, and tyrosine by phosphate stemming from adenosine-triphosphate (ATP). In eukaryotes, depending on the type of initial signal encountered, the propagated signal can induce a wide and varied array of cell responses, from apoptosis to cell division and proliferation. The known human kinome spans more than 500 members and is divided into eight distinct groups depending on their function, sequence similarity, and associated regulatory mechanisms (e.g. AGC group kinases have cyclic-nucleotide-dependent binding sites which partly control their activation) (Hanks and Hunter, 1995; Manning et al, 2002).

Although these distinct groups within the kinase family exist, there are some atypical kinases that do not meet the distinct criteria for this classification. One of these kinases is the with no lysine (k) kinase (WNK) which is distinguished by its unique placement of the catalytic lysine. Of the four known isoforms of the kinase, WNK1 is the best characterized. The WNK1 protein had become a focal point of research due to its involvement in a hereditary form of hypertension known as pseudohypoaldosteronism type II (PHAII). Interest in the kinase further grew when the initial structure was solved by Min *et al*

revealed a unique placement of the catalytic lysine along with an altered arrangement of residues in the nucleotide-binding site compared to that of other kinases (Min et al, 2004). Recent cellular assays involving WNK have revealed its involvement in electroneutral cotransporter regulation driven by the CCCs. These assays have also shown that CCCs present in kidney tissue are activated by hypotonic stress and by phosphorylation (Richardson and Alessi, 2008; Lytle and Forbush, 1996; Hoffmann et al, 1983). WNK has also been implicated in endocytic, and mitotic mechanisms and much detail concerning the biophysical underpinnings of the protein's function is still unknown.

This dissertation focuses on the regulation of the WNK1 kinase by an autoinhibitory domain and direct interaction of chloride ions with the kinase domain. A detailed structural and biochemical analysis of the regulatory domain will be discussed as well as the salt sensitivity of the kinase domain. Taken together, these studies suggest that the kinase domain itself is an anion sensor (specifically for chloride) and may be the initial mechanism that engages to control cell volume.

1.1 The WNK1 Protein Kinase

Data prior to the present thesis have partially characterized the domain boundaries, phosphorylation state and biochemical response of the WNK1 kinase domain to various stimuli in living cells. Further, there has been one crystallographic study of the inactive kinase domain which confirmed the unique

lysine placement relative to other protein kinases. The protein kinase WNK1 is a serine/threonine kinase that utilizes ATP to catalyze the phospho-transfer reaction of the γ -phosphate of ATP to a hydroxyl moiety on a serine or threonine amino acid located on a substrate protein. WNK1 was originally discovered through the efforts of Xu *et al* in an attempt to identify new members of the Ste20 family (which tend to be activators of MAP kinase modules) (Xu *et al*, 2000). The authors were successful in cloning and sequencing a 2126 amino acid, \sim 250kDa protein that localized in the particulate fractions of HEK293 cells. Sequence analysis of the kinase relative to other known protein kinases indicated it may be deficient of the catalytic lysine necessary for all known kinases to be enzymatically competent. Thus, the kinase was originally named due to its assumed lack of this lysine, which normally contributes to the transition-state stabilization by coordinating the α and β phosphates in ATP during nucleophilic attack by the substrate serine/threonine hydroxyl group. However, in the primary literature that stated the discovery of this unique protein kinase, Xu *et al* noted that mutation of K233 to methionine abolished kinase activity. It was predicted by sequence alignment that the lysine would be shifted from its canonical position in β 3 to a unique position in strand β 2 (Figure 1.1a).

Further biochemical analysis of this new protein kinase showed that the unique placement of the catalytic lysine could be incorporated into a similar arrangement by genetically modifying the MAPK extracellular signal-regulated kinase 2 (ERK2). Xu *et al* found that in WNK1, the typical placement

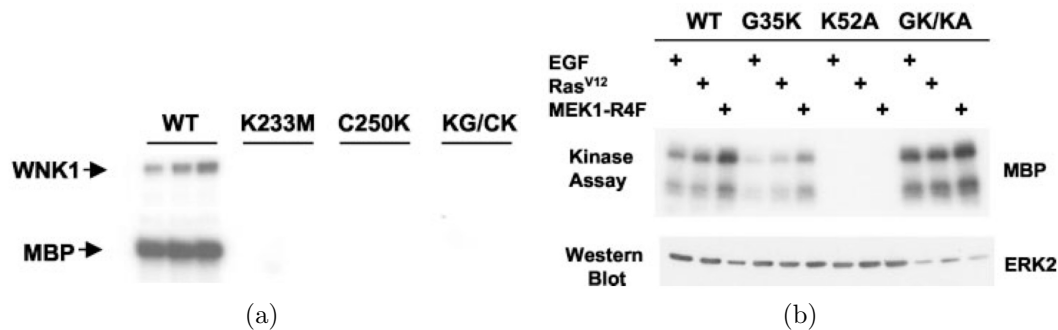


Figure 1.1: a) Mutation of the catalytic lysine of WNK1 abolishes activity toward MBP. An attempt to shift the lysine to the canonical position occupied by a cysteine. b) Placement of the catalytic lysine in ERK to an equivalent position to that in WNK1 does not abolish kinase activity of ERK toward MBP. This research was originally published in the Journal of Biological Chemistry. Xu, B.; Min, X.; Stippec, S.; Lee, B.; Goldsmith, E.J.; Cobb, M. H. Regulation of WNK1 by an Autoinhibitory Domain and Autophosphorylation. *J. Biol. Chem.* 2002; 277:48456-48462 © The American Society for Biochemistry and Molecular Biology

of the catalytic lysine is occupied by a cysteine and that trying to exchange these two amino acids (K233M, C250K) resulted in an enzymatically dead kinase toward the general kinase substrate myelin basic protein (MBP) (Xu et al, 2002). However, the authors found that moving the catalytic lysine from its wild-type position in ERK2 to one equivalent to the lysine position in WNK1, (G35K,K53A) allowed ERK2 to retain catalytic activity toward MBP when activated by EGF stimulation of HEK293 cells. Similar results were shown when the selective overexpression of Ras or MEK1-R4F was induced (Figure 1.1b).

Xu *et al* also described a new domain discovered at a location C-terminal to the kinase domain which comprises amino acids 485-555. The authors call this sequence the autoinhibitory domain. Xu *et al* expressed

three sequentially extended fragments of WNK1 using recombinant methods of expression in *E. coli*. The authors used a GST-coexpression vector which incorporated the protein glutathione S-transferase (GST) into the N-terminus of the WNK1 protein constructs with a 16-residue linker adjoined with a thrombin cleavage site (Xu et al, 2002). With the inclusion of this linked GST protein, the authors were able to isolate their expressed WNK1 constructs using reduced glutathione immobilized on crosslinked sepharose beads to elute the tagged protein using solublized reduced glutathione.

The first fragment, 1-491, displayed competent catalytic activity, as monitored by ^{32}P incorporation detected by autoradiography of an SDS-PAGE gel, toward the generic kinase substrate MBP as well as an interesting activity of autophosphorylation. However, when the amino-acid sequence was extended to include residues 1-555, there was a complete loss of catalytic activity for both autophosphorylation and substrate incorporation. Extension of the C-terminus to the 639th amino acid resulted in partial recovery of both autophosphorylation and activity toward MBP. The authors then tried to recapitulate these results using an *in trans* assay method that combined GST-tagged versions of both the kinase domain (1-491) and autoinhibitory domain (485-555, 485-539). Xu *et al* did, however, notice a core conservation in the autoinhibitory domain fragments among the WNK isoforms and potentially among many species (specifically rat, human and *c. elegans*) in the form of and Phe-X-Phe motif. The authors found that mutation of this motif to alanine (F524A,F526A) caused the loss of regulatory activity and WNK1 was

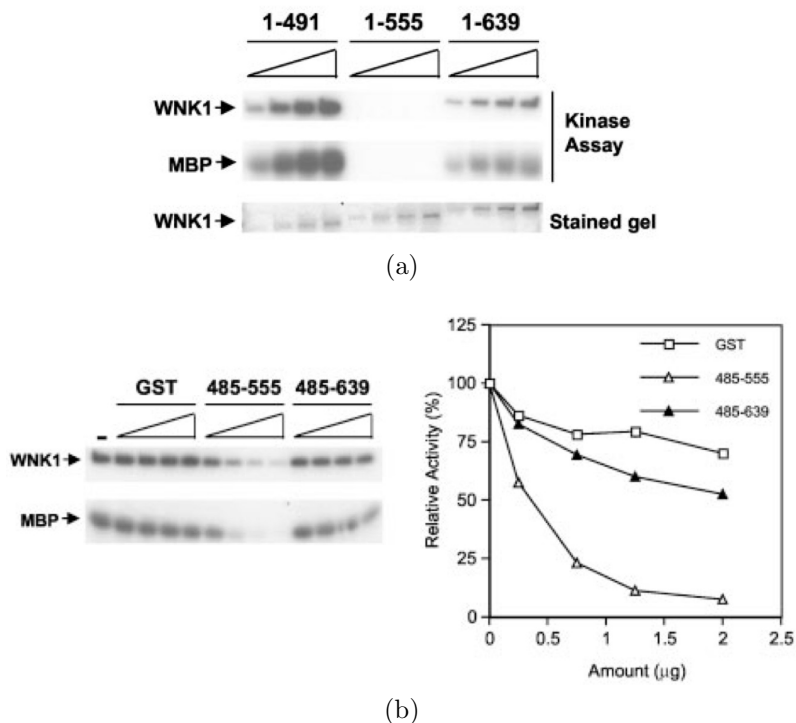


Figure 1.2: a) Expression of constructs of WNK1 with differing lengths show autoinhibition *in cis* when fragments of WNK1 are extended past the WNK1 kinase domain. b) Titration of GST-1-491 with GST-485-555 shows μM inhibition of WNK1 kinase activity toward MBP. This research was originally published in the Journal of Biological Chemistry. Xu, B.; Min, X.; Stippec, S.; Lee, B.; Goldsmith, E.J.; Cobb, M. H. Regulation of WNK1 by an Autoinhibitory Domain and Autophosphorylation. *J. Biol. Chem.* 2002; 277:48456-48462 © The American Society for Biochemistry and Molecular Biology

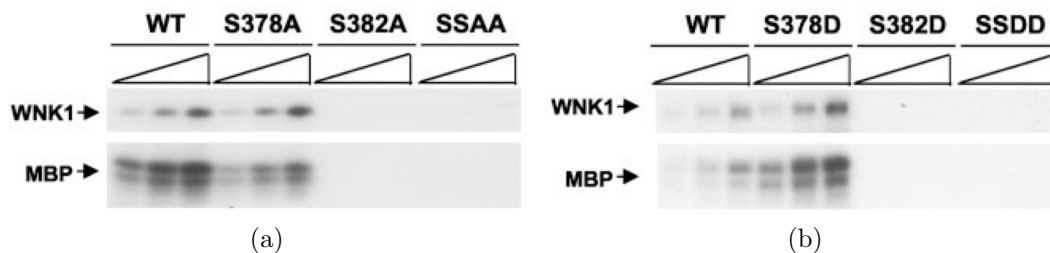
able to fully autophosphorylate and target MBP. ¹

In describing the initial findings of the newly discovered autoinhibitory domain, Xu *et al* also tested the activity of WNK1 through mutagenesis studies involving two serines in the activation loop that we now understand are

¹Author's note: it was the coincidence of noticing the FXX motif that allowed me to initially link sequence similarity of the autoinhibitory domain to the OSR-PF2 domain as described in later chapters.

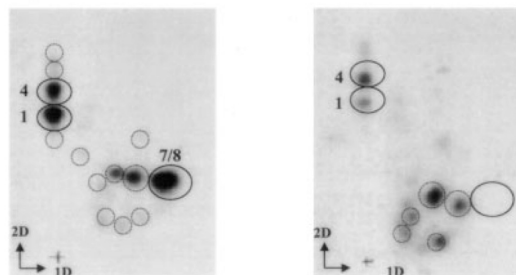
critical to WNK1 activity, Ser378 and S382. As seen in Figure 1.3a, while mutation of S378 to alanine reduces the activity of WNK1 to the generic kinase substrate MBP, WNK1 maintains its ability to autophosphorylate. However, when S382 is knocked out by alanine mutation, there is no observable incorporation of radiolabeled phosphate on WNK1 (autophosphorylation) or myelin basic protein. A more interesting result occurred when the common phosphomimetic mutation to aspartic acid was used for the two activation loop serines. When the S382D mutation was made, an effect similar to mutation to alanine was observed: the kinase was catalytically dead. However, when S378 was mutated to aspartate, the kinase was much more active toward both MBP and autophosphorylation than wild-type WNK1 (Xu et al, 2002). It was not discovered until later by Lenertz et al (2005) that wild-type, activated, WNK1 kinase was phosphorylated at both S378 and S382. It was thought that only S382 was phosphorylated because of mass spectrometry data detecting only phospho-S382 by Xu *et al.* However, in 2005, separation of phosphorylated peptides by 2D gel electrophoresis from WNK1 kinase domain expressed in *E. coli* and digested by incubation with trypsin protease showed that two phosphorylation sites in the activation loop were present. Mutation of S378A followed by identical treatment of the mutant protein showed the loss of a peak in the 2D gel electropherogram corresponding the peptide incorporated with phosphorylated S378 (Lenertz et al, 2005).

The structure of the WNK1 kinase domain in its mutant, inactive form:



WNK1: ³⁶⁶IGDLGLATLKRAS*FAKS*VIGTPEFMAPEMYEEK³⁹⁸

Peptide 1 RAS FAKS*VIGTPEFMAPEMYEEK
 Peptide 2 RAS*FAKS*VIGTPEFMAPEMYEEK
 Peptide 3 RAS*FAKS*VIGTPEFMAPEMYEEK
 Peptide 4 AS FAKS*VIGTPEFMAPEMYEEK
 Peptide 5 AS*FAKS VIGTPEFMAPEMYEEK
 Peptide 6 AS*FAKS*VIGTPEFMAPEMYEEK
 Peptide 7 RAS*FAK
 Peptide 8 AS*FAK
 Peptide 9 S*VIGTPEFMAPEMYEEK



WNK1 wild-type

WNK1 S378A

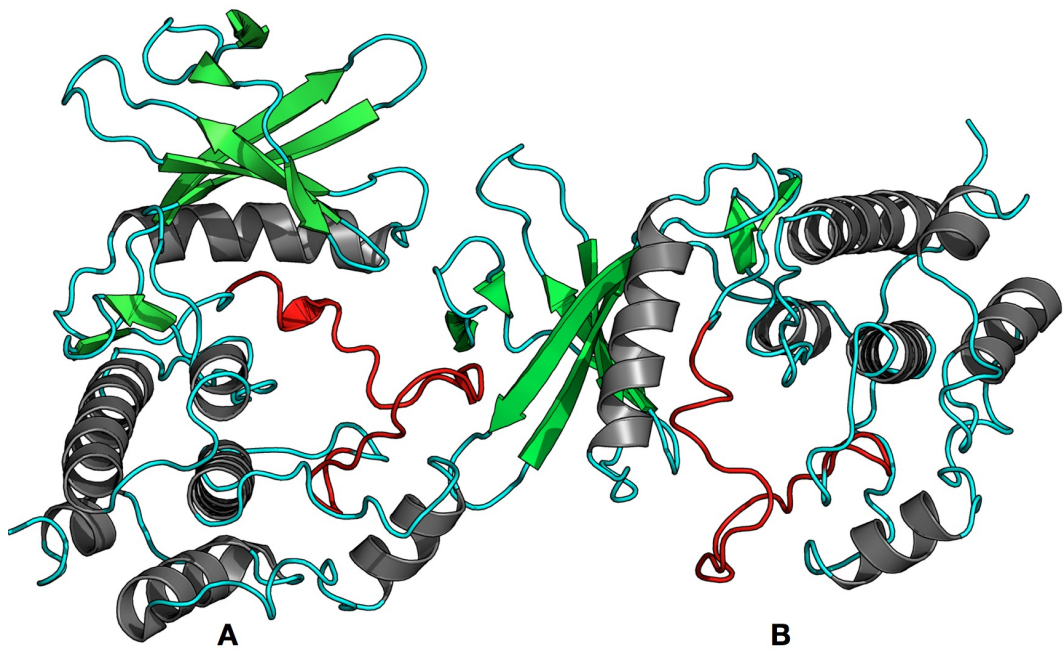
(c)

Figure 1.3: a) The WNK1 kinase domain is active toward MBP for both wild-type and the S378A mutant which abolishes one phosphorylation site in the activation loop. Mutation of S382 or both phosphorylation sites abolishes both autophosphorylation activity and activity toward MBP. b) Similar results are shown compared to a. Mutation of S378 to a phospho-mimetic is sufficient to resemble an activated WNK1 kinase domain. This research was originally published in the *Journal of Biological Chemistry*. Xu, B.; Min, X.; Stippec, S.; Lee, B.; Goldsmith, E.J.; Cobb, M. H. Regulation of WNK1 by an Autoinhibitory Domain and Autophosphorylation. *J. Biol. Chem.* 2002; 277:48456-48462 © The American Society for Biochemistry and Molecular Biology c) Isoelectric focusing of ³²P-incorporated activation loop peptides shows that WNK1 is phosphorylated at S382 and S378 in the wild-type protein. Mutation of S378 to alanine displays radiolabeled phosphate incorporation into S382. This research was originally published in the *Journal of Biological Chemistry*. Lenertz, L.; Lee, B.; Min, X.; Xu, B.; Wedin, K.; Earnest, S.; Goldsmith, E. J.; Cobb, M. H. Properties of WNK1 and Implications for Other Family Members. *J. Biol. Chem.* 2005; 280:26653-26658 © The American Society for Biochemistry and Molecular Biology

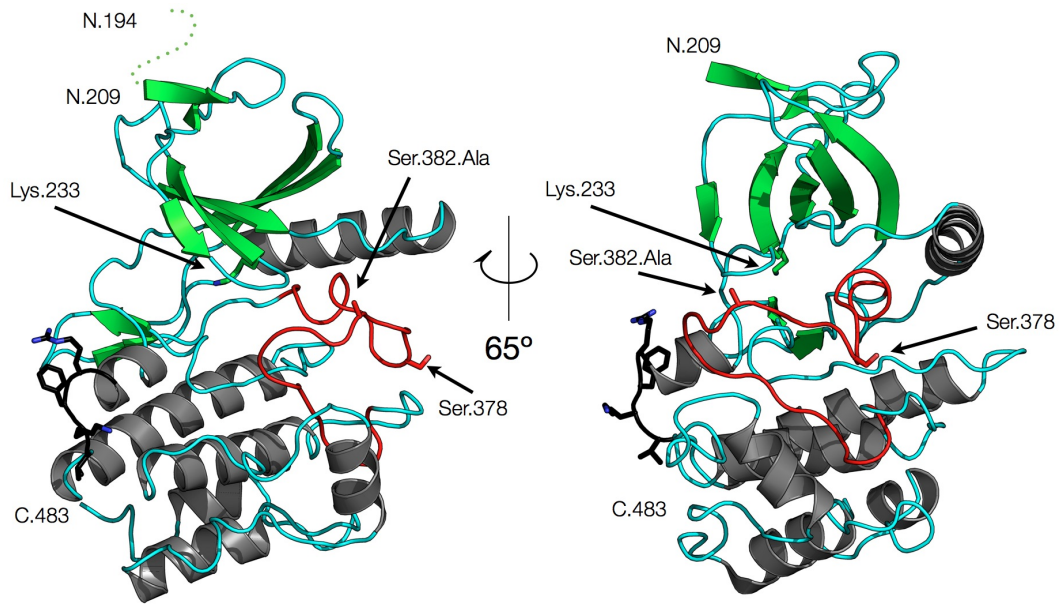
The structure of the kinase domain of the WNK1 protein kinase was solved by (Min et al, 2004) in its inactive form, with the mutation of S382 to alanine rendering the kinase unable to autophosphorylate during protein expression. The protein crystallized in the presence of 300 mM NaCl, 20-24% PEG 2000 (monomethylether), 100 mM HEPES pH=7.0 and diffracted to 1.8 Å. In general, the kinase displays a similar fold relative to that of other kinases: a bilobal architecture with the N-terminal lobe comprised primarily of beta strands and the C-terminal domain all containing alpha helices. Spanning the two lobes, the activation loop is clearly visible.

The kinase domain (194-483) was crystallized as an asymmetric "head-to-side" dimer in the space group P1 as seen in Figure 1.4. Although the construct used included residues 194-483, the first fifteen residues were unstructured and only electron density from 209-483 was visible. As predicted by Xu *et al* in the original description of the kinase sequence, the canonical position of the lysine was occupied by a cysteine (C250) in $\beta 3$ and the catalytic lysine (K233) was shifted to occupy a position in $\beta 2$ adjacent to the glycine-rich loop, which is a characteristic feature of protein kinases between $\beta 1$ and $\beta 2$ (Bossemeyer et al, 1993; Grant et al, 1998).

When the two monomers present in the asymmetric unit are compared, a striking difference between the two proteins are found in the N-terminal region of the kinase. Although the majority of the C-terminal α -helical region is unperturbed and has an RMSD for comparable C α atoms of 0.16 Å (compared



(a)



(b)

Figure 1.4: Crystal structure of the mutant, inactive WNK1 kinase domain. Adapted from Min et al (2004)

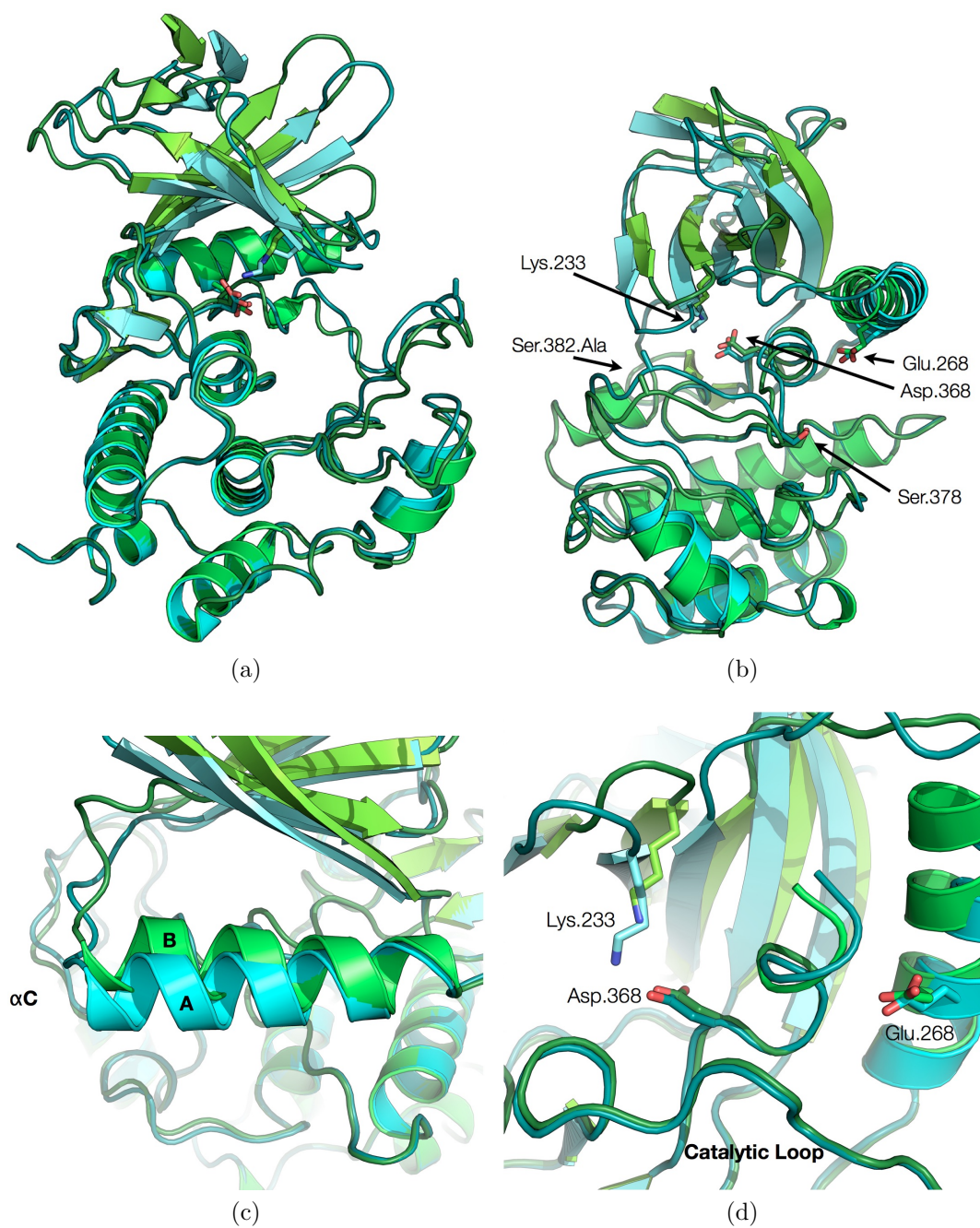


Figure 1.5: Structural comparison of monomers in the ASU of the mutant, inactive WNK1 kinase domain Adapted from Min et al (2004)

to an overall RMSD of 0.85 Å), there is a significant shift of the β strands in the N-terminal by 3 Å toward α C. Coordinated with this shift, the catalytic lysine C_α is shifted, but the N_ζ is still oriented toward the placement of the other monomer's lysine. In addition to the β shift, there is an associated displacement of α C inward toward the β barrel of 3.5 Å. The displacement of the α C helix is typically associated with conformational changes in kinases linked to the activation state of the kinase (Jeffrey et al, 1995).

In describing the nucleotide binding site, it was noted by Min *et al* that the equivalent glutamate (E268) in WNK1/ α C that is involved in coordination of the catalytic lysine from PKA (E91) is more than 13 Å away and interacting with R345 from the catalytic loop and R263 from α C (Min et al, 2004; Zheng et al, 1993). Min *et al* noted that the attempted expression of the kinase domain with the mutation of this glutamate to glutamine was unsuccessful. It is also of interest that R345 and the equivalent arginine in PKA (R165) is traditionally thought to be involved in stabilizing a phosphorylated amino acid in the activation loop but it is sequestered through its interaction with E268 from α C.

1.2 WNK1 Biochemical Pathway Involvement

1.2.1 NKCC Regulation

The WNK1 protein kinase was originally identified in a rare, genetic form of hypertension called PHAII wherein a deletion in the first intron of the gene causes overexpression of the kinase (Disse-Nicodème et al, 2000). In the distal convoluted tubule (DCT) of the kidney, where reabsorption of salt from the urinary lumen occurs, WNK1 is thought to interact with and activate OSR1/SPAK. These kinases, in turn, activate the NKCC electro-neutral symporters on the apical (lumen) side of the DCT, which pump Na^+ , K^+ and Cl^- ions across the cell membrane (Richardson and Alessi, 2008). It is currently speculated that the activation of these symporters occurs through a mechanism of hypertonicity which induces cell volume changes. However, it is unknown how the cell senses the change in intercellular salt in response to the active symporters. The mechanism for turning the system off is known to be mediated through the phosphatase PP1, which inactivates the NKCCs through removal of a phosphate group (Strange et al, 2006). On the basolateral side of the DCT, Na^+ ions are removed through the Na^+, K^+ -ATPase, and K^+ through the ROMK channel, while chloride is removed via the chloride channel (ClC-kb) which functions via a voltage-gated mechanism or through CFTR whose activity is controlled by WNK1 kinase activity (He et al, 2007; Kramer et al, 2008; Yang et al, 2007). The discovery of the WNK1 kinase and its interactions with substrates to effect signal transduction in this particular system was not arrived at in a sequential process as neatly as it is outlined

above. The following paragraphs place the timeline of those discoveries into perspective of how the signaling pathway was elucidated.

Oxidative and Stress Responsive kinase (OSR) was first characterized through an investigation of the c-Jun N-terminal kinase (JNK) in *Drosophila* S2 cells (Chen et al, 2004). This screen isolated the *Fray* gene as the regulator of JNK activity. In an attempt to study the protein further, the mammalian homologue, OSR, was isolated using reverse transcription-PCR from HeLa RNA. Following sequencing, Chen *et al* identified the OSR kinase domain by comparison with the published sequence of its homologue SPAK (Johnston et al, 2000). However, the authors also identified and classified two domains that are conserved among all GCK-IV members. The domains were named PF1 and PF2 due to their homology to the *Drosophila* genes *PASK* and *FRAY*, from which the domains were identified.

The first published experiments indicating that the SPAK and OSR kinases interacted with the cation-chloride cotransporters (Na,K,2Cl Cotransporters (NKCCs) and K,Cl Cotransporters (KCCs)) detailed yeast-two-hybrid experiments where the N-terminus of KCC3 was used as the bait and seven separate constructs of SPAK utilizing only the PF1 and PF2 domains and one containing only the PF2 of OSR were used as prey (Piechotta et al, 2002). The authors found that the C-terminal regions of both SPAK and OSR (where the PF2 domain was located) gave positive results in the two-hybrid screen. The experiment was then narrowed to include the PF2 domain of SPAK as the bait and several N-terminal fragments of KCC3 as prey. Using this strategy, the au-

thors were able to focus on a single motif with the sequence Arg-Phe-Xxx-Val (RFXV), which is conserved among all NKCCs and KCC3 but not KCC1/4. These results were confirmed by the same lab five years later through their monitoring of *in vitro* incorporation of $^{32}\text{PO}_4$ from γ - ^{32}P -labeled ATP into NKCC1 using SPAK as the activating kinase (Gagnon et al, 2007). The authors demonstrated that mutation of the RFXV phenylalanine or truncation of the N-terminus to exclude both RFXV motifs present in NKCC1 reduced incorporation of $^{32}\text{PO}_4$ at T217.

This localization signal from OSR/SPAK to its substrate NKCC/KCC was also found to be important for the binding of the activator of OSR/SPAK, WNK1. Anselmo *et al* showed, using a yeast-two-hybrid assay, that the C-terminal region of OSR interacted with three distinct segments of the WNK1 C-terminal region where four RFXV motifs were located (Anselmo et al, 2006). The molecular mechanism for both of these associations of OSR/SPAK with its activators and substrates was detailed through the crystal structure of the OSR-PF2 domain solved both in its *apo* and *holo* (bound with GRFQVT peptide) forms (Villa et al, 2007). The structure of the PF2 domain is characterized by four antiparallel β strands stacked against two α helices (Figure 1.6a). The strand connectivity is broken between $\beta 2/\beta 3$ by the α helices A and B and between $\beta 3/\beta 4$ by αC . The authors describe the presence of two binding pockets present in the structure: a 'primary' pocket between $\beta 2$ and αA , as well as a 'secondary' pocket near $\alpha 3$ adjacent to the loops bridging the β strands.

The *holo* structure shows the RFXV motif forming three distinct contacts in the structure. The first is an electrostatic interaction between the guanidinium group on the RFXV arginine and two acidic amino acids of the domain, D459/E467 (Figure 1.6b). These two residues are conserved throughout all PF2 domains as acidic residues. The second of these amino acids, E467, is universally conserved in PF2 domains as a glutamate and is located 1.5 turns from the beginning of αA . This conservation is likely a consequence of the location of the arginine-binding site near the loop spanning $\beta 2/\alpha A$. If this residue were mutated to an aspartic acid, it is unlikely that the sidechain would be long enough to reach from αA to the arginine binding site. The second important interaction is a π -stacking interaction formed between the RFXV phenylalanine and F452, which helps form the hydrophobic core of the PF2 domain (Figure 1.6c). The last interaction is a β backbone contact between the peptide valine and threonine to $\beta 2$ located in the protein (Figure 1.6d). The authors used surface plasmon resonance to examine the binding affinity between the OSR-PF2 domain and an octadecameric peptide derived from the C-terminus of WNK4 and also look at the effect of alanine scanning on the conserved 'primary' pocket. They found that the mutation of residues I450, L468, E467 and D459 in the OSR-PF2 domain were able to effectively abolish the ~ 50 nM binding affinity.

Although Villa *et al* mentioned the potential importance of the 'secondary' binding pocket in their discussion of the structure of the PF2 domain and showed that its residues are conserved among family members across

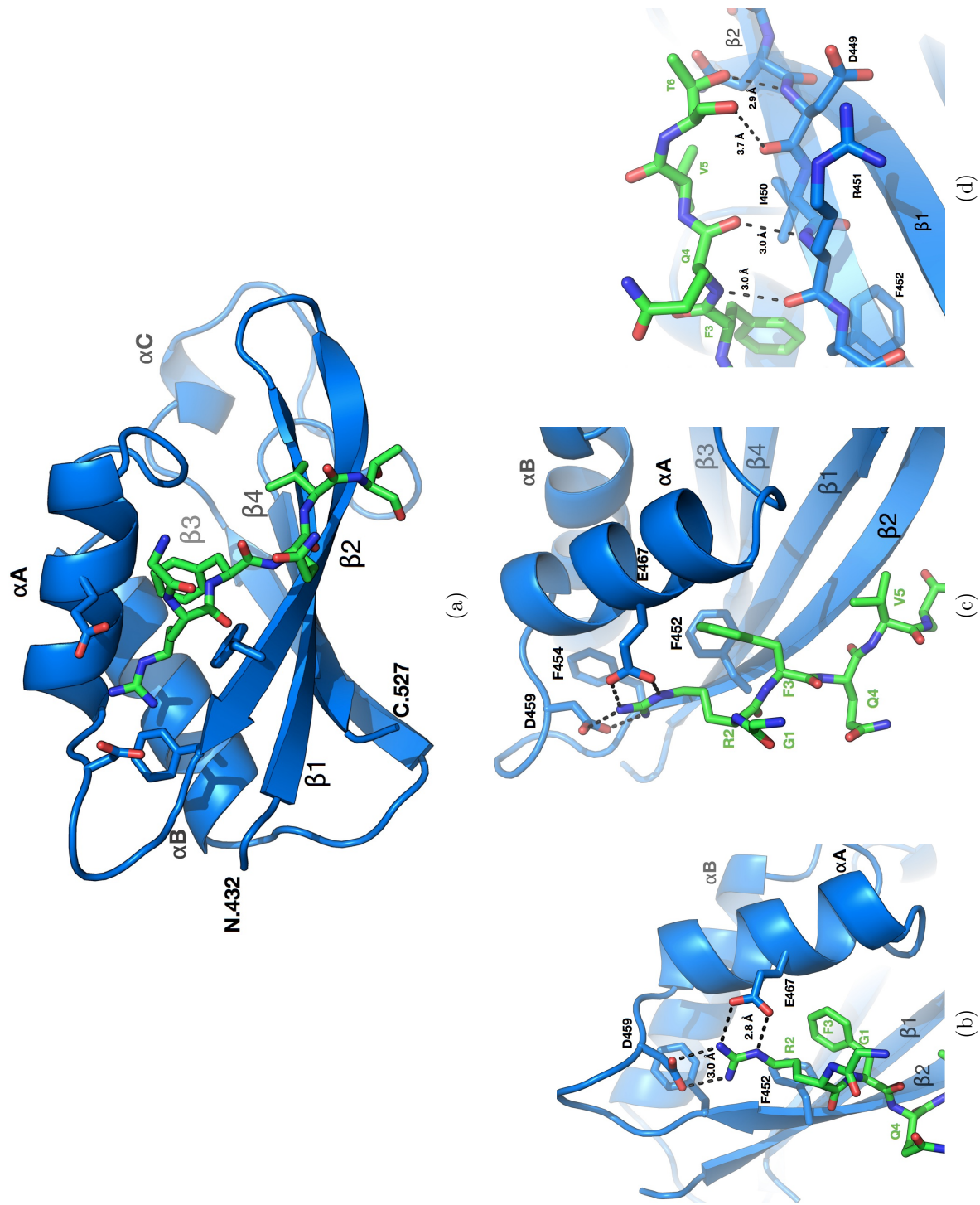


Figure 1.6: a) Structure of the OSR-PF2 domain bound to a GRFKVT peptide. The domain makes three distinct interactions with the RFXV peptide. b) An electrostatic interaction between the guanidinium group of the arginine from the peptide is made to a glutamate in αA and an aspartic acid in the loop between $\beta 2$ and αA . c) A π -stacking interaction between two phenylalanines from the peptide and the domain. d) A pseudo- β interaction is formed between the O_γ of the peptide's threonine and $\beta 2$ in the PF2 domain. Adapted from Villa et al (2007)

species, the authors stated that their alanine mutagenesis studies of three residues in the 'secondary' pocket (L440, S443, V507) showed no appreciable change in affinity of the selected peptide. The authors concluded from this observation that the residues were "not essential of the binding of OSR1 activators and substrates (Villa et al, 2007)."

The location of the PF2 domain on the OSR and SPAK kinases allows it to localize to both its activator and substrates through the presence of RFXV motifs on both types of proteins. Further, phosphorylated serine and threonine residues adjacent to the RFXV arginines by Zagorska *et al* were detected by MALDI/TOF mass spectrometry (Zagorska et al, 2006). The possibility of regulation by phosphorylation was tested by Villa *et al* through the use of synthetic peptides from WNK4 that were phosphorylated during the synthesis process. The authors showed that there was a marked decrease in binding affinity by SPR, suggesting a mechanism counterintuitive to that of SH2 (Src Homology 2) domains that preferentially bind phosphotyrosine moieties (Pawson et al, 2001).

1.2.2 Responses to Changes in Osmolarity

Cellular assays of the response of the WNK kinases to osmotic stressors (NaCl and Sorbitol) have been measured by *in vivo* and *in vitro* assays. The results show a response of WNK1 to both hyper- and hypo-osmotic conditions. However, these observations presented in the literature regarding the amount of WNK1 activation in response to changing osmotic conditions are

inconsistent. The results of the experiments as they were presented in the journal articles will be discussed in the current section, while the interpretation of results and implications of those results in light of these studies will be discussed, at length, in Chapter 9. During the initial investigations of the WNK1 protein kinase, Xu *et al* treated HEK293 cells overexpressing WNK1 with a series of extracellular kinase activators including EGF, nocodazole, anisomycin, lipophosphatidic acid (LPA), and NaCl. WNK1 was immunoprecipitated from cells and assayed for autophosphorylation, and it was found that the cells stimulated with NaCl had the greatest increase in ^{32}P incorporation (Xu et al, 2000). The authors noted that phosphorylation of MBP was not monitored due to "background phosphorylation [being]...too high to be a reliable measure of activity." A more extensive investigation of WNK1 autophosphorylation was undertaken by Lenertz et al (2005), wherein a wider array of osmolites were included. Using mouse distal convoluted tubule (DCT) cells, cell cultures were treated with glucose, sucrose, mannitol, sorbitol, NaCl, and KCl at various concentrations for up to 1.5 hours with the predominant intervals being 15 minute incubations. Although changes in autophosphorylation were detected among all osmolites, the greatest changes were effected by sodium chloride and potassium chloride. These effects were replicated in five separate cell lines (DCT, MCF7, MDA-MB-231, SW480 and HT-29) to varying degrees, with the greatest change between control and treated cells being in DCT cells with a 9.5 fold increase in autophosphorylation activity.

Zagorska *et al* also reported the response of overexpressed WNK in

HEK 293 and HeLa cell lines when immunoprecipitated and assayed against kinase dead OSR (D164A) (Zagorska et al, 2006). In the first experiments, HEK 293 cells expressing endogenous WNK1 were exposed to sorbitol (0.5 M) for half an hour. WNK1 was immunoprecipitated and assayed against kinase dead OSR. The authors reported that following sorbitol exposure, WNK1 was more active toward OSR than control preparations and that phosphorylation of WNK1 increased near at least one RFXV site in the C-terminus as well as in two regions of polyproline repeats (An N-terminal poly proline repeat region (94-117), is necessary for binding to intersectins (He et al, 2007)).

Further experiments showed that incubation of HEK 293 cells for up to 80 minutes with sorbitol still showed increases in ^{32}P incorporation into OSR substrate. When the authors repeated these experiments using increasing amounts of NaCl, they reported similar findings when increasing NaCl concentrations up to 1 molar. However, the most striking result from this paper is the response recorded in live cells expressing GFP-tagged WNK1. Briefly, HEK 293 cells were treated with either 0.2 M sorbitol or NaCl and the GFP channel recorded localization of WNK1 in the cell. After 30 seconds of treatment in either case, there is a dramatic ($\sim 20\text{-}30\%$) reduction in cell size followed by localization of WNK1 to clathrin-coated vesicles within 2-3 minutes following stimulation. The authors were able to identify these vesicles as clathrin-containing due to immuno-staining of cells for clathrin and a number of effector proteins associated with clathrin vesicles. The authors also note that this process is reversible following a wash step in the absence of sorbitol

or salt-containing buffers.

The most recent report of WNK effects driven by the presence of salt were reported by Moriguchi et al (2005) while investigating the interaction of WNK1 with OSR/SPAK through RFXV motifs and the downstream effect on NKCCs. In the final experiment reported, the authors exposed HEK 293 cells to isotonic or hypotonic chloride buffers. WNK1 was then immunoprecipitated from the cells and assayed for activity against the SPAK PF1 domain. The authors found that WNK1 has reduced activity toward substrate in the presence of chloride ion and an increase in kinase activity toward SPAK when chloride ion was removed. These results were confirmed using an *in vitro* ^{32}P -labeling assay in which HEK293 cells were preincubated with radiolabel for 6 hours before being exposed to isotonic or hypotonic buffer. Immunoprecipitation of T7-NCC followed by autoradiography showed reduced incorporation of ^{32}P into NCC in high-chloride-content buffer compared to low-chloride-containing buffer.

1.2.3 Incompletely Characterized Functions

In addition to the involvement of WNK1 in a putative salt-sensing role for the cell, the WNK protein kinases may influence a wider variety of cellular pathways including exocytosis, chloride-channel cycling and maintenance of spindle polarity during mitosis.

Endocytosis/Exocytosis

The endocytic process in the cell is a necessary mechanism for the

internalization of extracellular material for use by the cell and helps in the turnover and regulation of membrane-bound proteins including ion channels (Mukherjee et al, 1997). As discussed in the previous section, WNK1 localizes to endocytic clathrin-coated vesicles identified through colocalization experiments from microscope images of immunostained HEK293 cells (Zagorska et al, 2006). Other evidence has shown that this effect may include the act of internalization of ROMK1 (renal outer medullar potassium channel 1) through WNK1's interaction with intersectin (He et al, 2007). He *et al* showed that the WNK1 interaction with intersectin follows as a kinase-independent mechanism wherein a set of three poly-proline motifs housed between amino acids 94-117 bind to the third of five consecutive SH3 domains located in intersectin's C-terminus. The authors qualitatively linked the internalization of ROMK1 to the interaction of WNK1 and intersectin by measuring amounts of surface ROMK1 and its associated current density. Overexpression of WNK1-FL and derivative constructs only containing the necessary polyproline motifs required for intersectin interaction decreased current density, while negative controls exempting this region showed no deviation from normal current density in the absence of WNK1.

WNK1 has also been shown to be important, in a kinase-dependent manner, for the regulation of synaptotagmin 2 (Syt2). Synaptotagmins are integral proteins to exocytic mechanisms through their interaction with the SNARE complex (Chapman, 2002). Synaptotagmin comprises an N-terminal transmembrane helix and two tandem C2 domains that bind Ca^{2+} (C2A and

C2B), which are required for membrane binding and fusion of vesicles with the plasma membrane. In a report published by Lee et al (2004), it was found that WNK1 interacts with synaptotagmins 1-3 and 9 (but not 4,7 and 8) through a conserved valine - located at the C-terminus of the RFXV motif (V318) - that is not present in WNK4. It was hypothesized that, because WNK4 does not interact with Syt2, mutation of the valine to a charged residue would disrupt the WNK1 kinase domain's interaction with Syt2, which the authors confirmed through yeast two-hybrid assay. Lee *et al* also demonstrated that WNK1 phosphorylation of Syt2 T202 in the C2A domain and T366 in the C2B domain plays an integral role in the regulation of Ca²⁺ binding and the resultant localization of Syt2 to the plasma membrane during the vesicle fusion process.

Chloride channel conductance regulation

Cystic fibrosis is a genetic disease that is most commonly induced by the deletion of phenylalanine 508 in both chromosomal copies of the cystic fibrosis transmembrane conductance regulator (CFTR). The CFTR protein pumps chloride ions across the plasma membrane to the extracellular space and is particularly important in the maintenance of mucosal thickness near the epithelial cells of the lung for clearance of airborne bacteria such as *Pseudomonas aeruginosa* (Guggino and Stanton, 2006). WNK1 and WNK4 have been shown to independently inhibit CFTR chloride conductance in a kinase-dependent and kinase-independent fashion, respectively. Both kinases inhibit CFTR activity by approximately 40% and, for WNK4, in a dose-dependent

fashion (Yang et al, 2007).

Mitotic processes

Finally, the most recent finding of WNK1 involvement in cellular processes not directly linked to maintenance of salt levels in the cell is reported by Tu et al (2011). Knockdown of WNK1 and OSR using siRNA, followed by immunostaining was used to track cells in varying stages of mitosis. The authors showed that WNK1 and OSR are localized in punctate patterns throughout HeLa cells. However, during mitosis, WNK1 colocalizes with α -tubulin to the mitotic spindle, whereas OSR1 is excluded. When WNK1 is knocked down in these same cells, a loss of spindle polarity is observed concomitant with a 65% reduction in cell survival compared to only a 25% reduction when OSR1 was knocked out (Tu et al, 2011). Also observed was an extension of the bridge between the dividing daughter cells. The authors report an extension of the abscission process by a total of 15 hours when WNK1 was knocked down compared to wild-type cells.

1.3 Description of Dissertation Research

Chapter 2 describes the expression and purification of the WNK1 autoinhibitory domain in preparation for NMR analysis and structure determination.

Chapter 3 presents a theoretical description of 1D and 2D NMR and describes the experiments conducted for the results presented in Chapter 4.

Chapter 4 discusses the structural determination of the WNK1 autoinhibitory

domain and analysis of the structure in comparison to the OSR-PF2 domain. The chapter also describes the incubation of the autoinhibitory domain with three constructs of RFXV peptides and the resulting change in the $^1\text{H},^{15}\text{N}$ -HSQC of WNK1 (480-572).

Chapter 5 describes the expression, purification, and crystallization of the activated (doubly phosphorylated) WNK1 kinase domain (209-483) in preparation for X-ray data collection.

Chapter 6 describes the theoretical framework of X-ray crystallography and the solution to the phase problem by molecular replacement. The chapter continues with the description of the data collection for the activated WNK1 (209-483 S378*,S382*) and the subsequent description of the structure and its comparison to the inactive WNK1 kinase domain (194-483 S382A).

Chapter 7 discusses biochemical and biophysical experimentation on the WNK1 kinase domain (194-483) and its associated mutants. The chapter also discusses experimentation done regarding the tethered kinase and autoinhibitory domains (194-573) and associated mutants.

Chapter 8 describes the expression, purification and crystallization of WNK1 (194-483 S382A) in the presence of sodium bromide. The chapter discusses the presence of bromide ion signal from the anomalous difference fourier map and the location and re-refinement of the chloride-bound structure of WNK1 (194-483 S382A) determined by Min *et al.*

Chapter 9 attempts to place the data collected in a physiological context and provides perspective on future investigations of the WNK1 kinase.

Chapter 2

Expression and Purification of the WNK1 Autoinhibitory Domain

2.1 Introduction

There are four members of the WNK kinase family which vary in length and overall sequence identity and all contain an autoinhibitory domain which was originally defined by the span of residues 485-555 in WNK1 and is flanked on the N-terminus by a 7 residue linker to the end of the kinase domain and immediately to the C-terminus by what was thought to be a coiled coil domain. As previously discussed, the location of this domain was encountered by (Xu et al, 2002) in one of the original papers describing the protein kinase by expressing varying lengths of the protein and testing for ^{32}P incorporation into MBP and WNK1 (autophosphorylation).

This chapter describes the bioinformatic analysis of the WNK1 autoinhibitory fragment which ultimately expanded the domain boundaries for the regulatory domain to include residues 480-572 and predicted by both sequence similarity and secondary and tertiary domain topology analysis that the WNK1 autoinhibitory fragment has the same fold as the OSR-PF2 domain and retains the necessary residues to both form an RFXV binding pocket and bind the arginine guanidinium group in a similar manner to that of the

OSR-PF2 domain. This chapter also includes the methodology necessary for expression of the WNK1 autoinhibitory domain in standard or M9 minimal media preparations (using either unlabeled or uniformly ^{15}N and ^{13}C labeling) for accommodating investigation by NMR methodologies presented in Chapter 3.

2.2 Bioinformatic analysis of the WNK1 autoinhibitory domains

2.2.1 Sequence alignment

PSI-BLAST (Altschul et al, 1997) against the filtered NR database (May 10, 2009, 8483808 sequences) using the PF2 domain structure sequence (gi—151568135, residues 1 to 96) as a query with default parameters (E-value cutoff 0.01, iterated to convergence at round 7) identified a number of WNK sequences as hits, including rat WNK1 (gi—41688742, E-value in final iteration $2\text{e-}18$). Secondary structure prediction of the WNK1 sequence (gi—41688742) using the JPRED server (Cole et al, 2008) identified a reliably-predicted β -strand N-terminal to the previously defined autoinhibitory domain (residues 485 to 489, along with a confidently predicted C-terminal helix (residues 550 to 570). WNK1-related sequences were gathered using PSI-BLAST (identical parameters as above) using the query (gi—41688742, residues 480 to 570).

2.2.2 Secondary and tertiary structure prediction

Multiple-sequence alignments of identified sequences were generated using PROMALS3D (Pei et al, 2008). WNK1 sequence corresponding to the extended domain boundaries was submitted to ROSETTA (Rohl et al, 2004) ab-initio structure prediction (41688742, residues 480 to 570). ROSETTA generated and clustered 1200 decoys, with a top cluster size of 24 decoys. Inspection of structure representatives of the top 10 clusters identified a fold of similar topology in 6 out of 10 clusters (totaling 84 decoys).

2.2.3 Discussion

Using an NCBI-BLAST search of the expressed sequence (WNK1-485-555), the initial sequence-similarity search revealed that the autoinhibitory domain is a paralog of the OSR1-PF2 domain with 28% similarity as identified by a BLOSUM62 score analysis and is conserved among all autoinhibitory domains for WNK family members.

The outlined region in Figure 2.1 is the RFXV-binding site for the OSR-PF2 domain and is the locus of the highest sequence conservation between the OSR-PF2 and the WNK1-AI domains which include four peptide-binding residues, identified previously in the crystal structure of the PF2 domain, two phenylalanines and two acidic residues. Overall, there is a greater degree of conservation of aspartic acid at the first acidic site, although it is a glutamate in all of the WNK2 autoinhibitory domains that we investigated using our bioinformatics query, and the second acidic site is wholly conserved

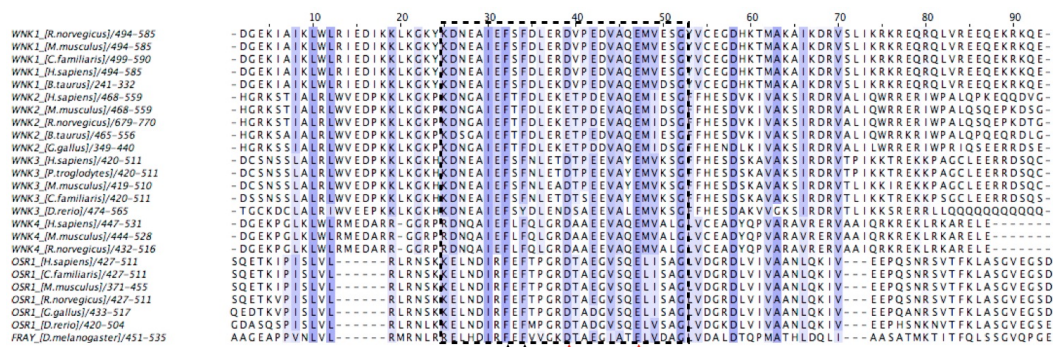


Figure 2.1: Sequence Alignment of WNK Autoinhibitory Domains with OSR-PF2 Domains. The boxed residues show the conserved RFXV binding site found by BLAST sequence analysis. The black arrows show the placement of two conserved phenylalanine residues while the red arrows show the two conserved acidic residues necessary for binding the RFXV arginine in the PF2 domain from OSR.

as a glutamate - likely due to its placement 2.5 turns down αA (See chapter 4).

In investigating this domain, the BLAST results indicated that the homology of the PF2 domain in the WNK1 sequence extended beyond the previously published boundaries to include residues 480-572. Upon further analysis, we found that the architecture of the protein was likely modified through the removal of the penultimate C-terminal β -strand found in the PF2 domain and the prediction of a non-homologous strand in the N-terminus of the autoinhibitory domain encompassing residues 482-489. Because of this bioinformatic examination of the domain, we were able to redefine the domain boundaries of the WNK1 kinase. We have extended the C-terminus of the domain to include what was once postulated to be a coiled-coil domain and moved the N-terminus to abut the C-terminal tail of the kinase domain. In querying this

consensus binding site to the remainder of the protein, we discovered another putative autoinhibitory/PF2-like domain which encompasses residues 864-948 of WNK1.

2.3 Construct design

The construct for expressing the WNK1 autoinhibitory domain (480-572) was cloned into the pHis-parallel expression vector, which was commonly used for WNK1 expression (Min et al, 2004; Sheffield et al, 1999). Primers were designed for the PCR amplification of the desired WNK1 autoinhibitory fragment to utilize the 5'-BamHI and 3'-XhoI endonuclease sites present in the pHis-parallel vector. Four separate trials using WNK1 cDNA (generously provided by the lab of Melanie Cobb, Ph.D.) were run to generate the desired PCR product using the following protocol:

Table 2.1: PCR Protocol for WNK1 (480-572)

Cycles	Time (s)	Temp. (°C)					
29x	30	98	H ₂ O	36.5	36.0	35.0	32.0
	10	98	5 μ M <i>f. primer</i> [†]	5.0	5.0	5.0	5.0
	30	67	5 μ M <i>r. primer</i> [‡]	5.0	5.0	5.0	5.0
	22 [§]	72	4 mM DNTP Mix	2.5	2.5	2.5	2.5
	300	72	10X <i>Pfu turbo</i> buffer	5.0	5.0	5.0	5.0
	∞	4	1X <i>Pfu turbo</i> enzyme	0.5	0.5	0.5	0.5
			cDNA template	0.5	1.0	2.0	5.0
Total (μ L)				50	50	50	50

[†] 5'-GCCATGGATCCGCAGGAGGAAACAGGGGTACGGGTAGAA-3' (sense)

[‡] 5'-GTGCTCGAGTTATCACCGCTGCTCTCGTTTTCTCTTAATTAATGA-3' (antisense)

[§] 15 s/kb for extension

Following the PCR reaction, the resultant amplified fragment was separated by size on a 0.8% (w/v) agarose gel and purified using a gel purification kit (Qiagen). The purified fragment was then subjected to digestion by *Bam*HI and *Xho*I endonucleases along with a purified empty pHis-parallel vector as shown in Table 2.2. To complete the cloning process, the digested fragments were once again separated using an agarose gel and purified using isopropanol precipitation from the gel purification kit. The post-digest PCR fragments were then combined with the digested empty pHis-parallel vector in a 7:1 ratio and allowed to incubate according to Table 2.3 for one hour at room temperature before being transformed into *E. coli* DH5 α cells and selected for ligation products by incubating them on LB/ampicillin agar plates at 37°C. A total of eight colonies were picked, and the plasmids were purified using a MiniPrep kit (Qiagen) before being sequenced at the UT Southwestern Sequencing Facility. Sequencing analysis showed that the PCR product was inserted in frame with the N-terminal histidine tag.

2.4 Expression

2.4.1 Expression Trials

Following subcloning into pHis-parallel, WNK1 480-572 was expressed as previously described by Min (2004). Briefly, 1 μ L of WNK1 (480-572) plasmid was transformed into Rosetta (Novagen) *E. coli*, which was used for the expression because the WNK gene includes the rare tRNA codons AGG, AGA,

Table 2.2: Digest of WNK (480-572) and pHis-Parallel (empty)

	PCR: WNK1 (480-572)/Template	14 μL ea.
	10X BSA	2 μL
	NEB4 Buffer	2 μL
	<i>Bam</i> HI	1 μL
	<i>Xho</i> I	1 μL
Total	20 μL	

[†] 2hr incubation at 37°C followed by gel purification. Yellow arrows delineate cut fragments of either empty pHis-parallel vector (lanes 2,4) or cut PCR product (lanes 3,5)

Table 2.3: Ligation of WNK (480-572) and pHis-Parallel (empty)

	Digested WNK (480-572) fragment	7 μL
	Disgested pHis-parallel (empty)	1 μL
	10X <i>T</i> ₄ ligase buffer	1 μL
	<i>T</i> ₄ DNA ligase	1 μL
	Total	10 μL

[†] 1hr incubation at 22°C followed by transformation into DH5 α . Lanes 1-8 delineate samples of plasmid DNA (yellow arrow) purified by MiniPrep (Qiagen) by growing 5mL cultures in LB+AMP post ligation and transformation.

AUA, CUA, CCC, and GGA. The transformants were plated on agar plates containing LB, ampicillin and chloramphenicol. A single colony was selected and grown in 60 mL of LB, ampicillin and chloramphenicol overnight at 37°C (200rpm). After 16 hours, the cell culture was refreshed by inoculating 5 mL

of this starter culture into 60 mL of LB, ampicillin and chloramphenicol for 1 hour at 37°C (200rpm).

The first cultures were grown following a similar protocol for making the WNK1 kinase domain (194-483), which included inoculating 6 L of LB (6 x 1L Fernbach flasks) and growing at 37°C (200rpm) until the optical density (OD_{595nm}) reached 0.8. The culture medium was induced using a final concentration of 1 mM isopropyl β -D-1-thiogalactopyranoside (IPTG) and incubated at 18°C (200 rpm) for 16-20 hours. Following expression, cells were centrifuged at 4000 rpm for 35 min at 4°C and the pellets resuspended in 5 mL of Ni Buffer A (Table 5.1), flash frozen in $N_2(l)$, and stored at -80°C.

To optimize expression for the expression of uniformly $^{13}C,^{15}N$ -labeled protein in M9 minimal media, two expression cultures containing 1 L of M9 minimal media were inoculated with 10 mL of *E. coli* culture transformed with pHis-WNK (480-572) grown in LB, ampicillin and chloramphenicol (Gardner and Kay, 1998). Both cultures were grown at 37°C to an OD_{595nm} of 0.7 and induced using a final concentration of 1 mM IPTG. At this point, one culture was sequestered and incubated at 20°C (230rpm) for 15 hours while the other continued to be incubated at 37°C for 3 hours. Samples taken from the cultures were taken to assess the level of protein expression by SDS-PAGE gel at discrete time points for each temperature.

2.4.2 Uniform ^{13}C , ^{15}N labeling in M9 minimal media

To label WNK1 (480-572) uniformly with ^{13}C , ^{15}N , the general protocol for expression as discussed above was followed except for the preparation of M9 minimal media. As Gardner and Kay (1998) discuss, inclusion of ^{15}N -ammonium chloride and uniform ^{13}C -labeled D-glucose will take advantage of the *E. coli* amino-acid synthesis by allowing for full incorporation of ^{13}C and ^{15}N into the amide backbone in addition to the sidechain carbon and nitrogen atoms. To prepare those media, 100 mL of M9 salts (67.8 g Na_2HPO_4 (anhydrous), 30 g KH_2PO_4 , 5 g NaCl in 1 L of distilled H_2O) along with 2 L of water were autoclaved along with a 2.4 L Fernbach flask and a 1 L glass volumetric cylinder. In the presence of a lit Bunsen burner, 100 mL of 10X M9 salts were combined with 1 mL each of CaCl_2 , MgSO_4 and 10 mg/mL thiamine (sterile filtered) and biotin (not filtered). To this 1 g of $^{15}\text{NH}_4\text{Cl}$ dissolved in 10 mL of water and 3 g of $\text{U-}^{13}\text{C}$ -D-glucose were added. This was followed by the addition of enough sterile water to make a 1 L solution. The solution was prewarmed to 37°C , and the working concentration of ampicillin and chloramphenicol were added immediately prior to inoculation. The media was inoculated with 10 mL of Rosetta (Novagen) *E. coli* culture grown in LB, ampicillin and chloramphenicol. The best expression was obtained by incubating the culture until the $\text{OD}_{595\text{nm}}$ reached 0.8 and inducing using 1mM IPTG (final concentration). The culture was grown for 2 hrs after induction and pelleted using centrifugation (4000 rpm for 35 min). The pellet was re-suspended in 5 mL/L of cell culture in Ni Buffer A (Table 5.1), flash frozen in

$N_{2(l)}$, and stored at -80°C .

2.5 Purification

To purify the expressed protein, cells were thawed and lysed in the presence of protease inhibitors (Sigma) using an Emulsiflex C5 (Avestin) homogenizer by passing the cell paste 4x through the system. Homogenized cell lysate was then centrifuged at 40,000 rpm for 1 hr at 4°C to separate soluble from insoluble fractions. The resultant supernatant was passed through a $0.45\ \mu\text{M}$ filter before being loaded onto a precharged Ni^{2+} -sepharose column (GE). The column was washed with 10 column volumes of Ni Buffer A (Table 5.1) and attached to an AKTA (Pharmacia) system. A linear gradient ranging from 0-250 mM imidazole in Ni Buffer A was used to elute the protein-containing fractions (Figure 2.2).

The WNK1 (480-572)-containing fractions were consolidated and dialyzed overnight against Mono Q buffer A (Table 5.1) in the presence of 1 mg of TEV protease at 4°C . Following 12-16 hours of dialysis, the contents of the dialysis were applied to a 2 mL Ni^{2+} -agarose column (GE) to remove the TEV protease, the cut His₆ tag, and any protein containing the tag that was not cleaved by TEV. The eluent was concentrated and loaded onto a MonoQ 5/5 (GE) for anion-exchange chromatography. WNK1 (480-572) was eluted using a linear gradient of 20-500mM NaCl in MonoQ buffers A and B, respectively (Figure 2.3). The protein of interest eluted in the first fractions, which were pooled and dialyzed overnight against 10 mM Tris pH=6.5, 10 mM NaCl, 1

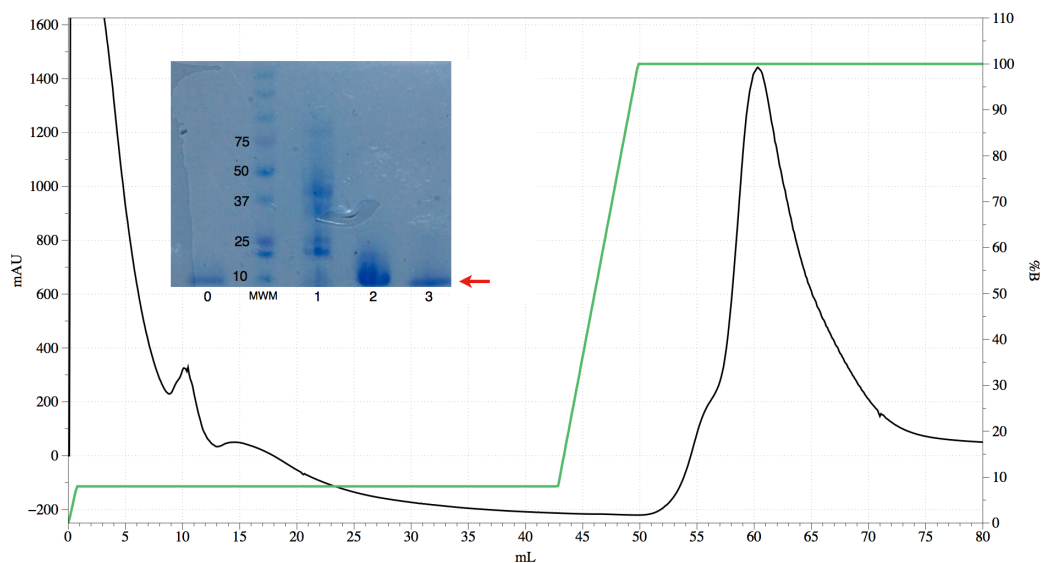


Figure 2.2: Ni^{2+} -sepharose of $\text{U-}^{13}\text{C},^{15}\text{N}$ -WNK1 (480-572). Fractions represented in the PAGE gel are as indicated 0) WNK1 (480-572) standard 1) flow through fraction post loading of column, 2) Pre-TEV digestion 3) Post-TEV digestion

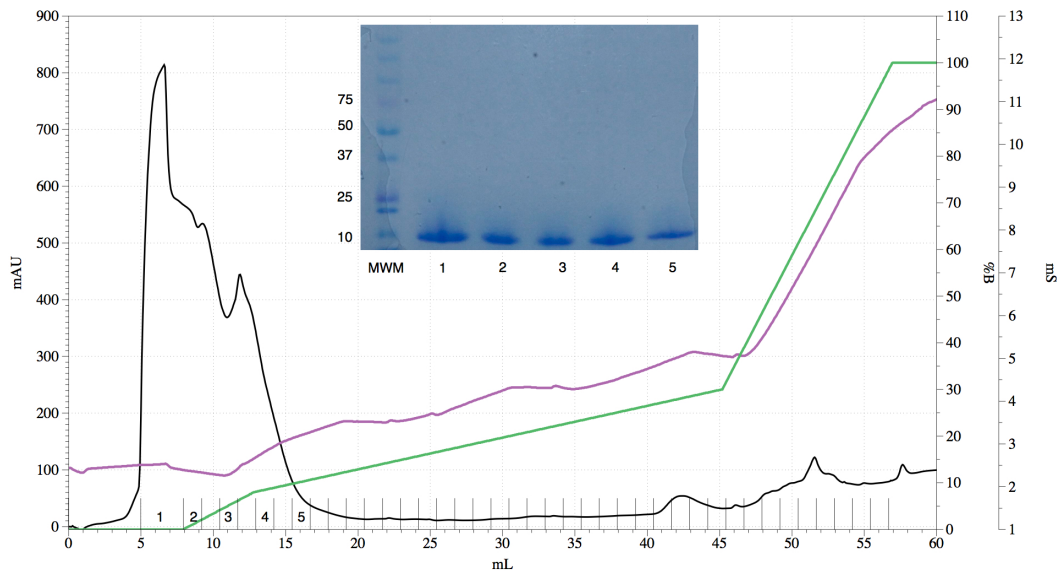


Figure 2.3: MonoQ of $\text{U-}^{13}\text{C},^{15}\text{N}$ -WNK1 (480-572). Fractions 1-5 are represented as the respective fractions from the first peak in the chromatogram.

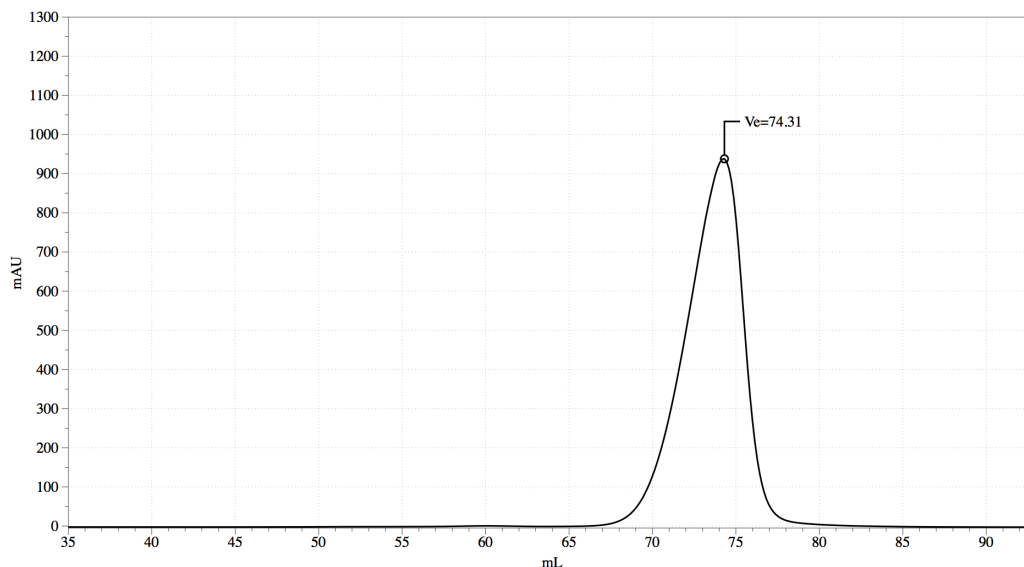


Figure 2.4: Superdex 75 (16/60) of U- ^{13}C , ^{15}N -WNK1 (480-572)

mM DTT. WNK1 (480-572) was concentrated and loaded onto a Superdex 75 (16/60) column (GE), and the protein was eluted isocratically with an V_e of 75 mL (Figure 2.4). Protein was concentrated to an apparent concentration of 10 mg/mL as assessed by Bradford assay. However, to glean a more accurate measure of concentration, what was estimated to be 2 mg of total protein was buffer exchanged into deionized water, lyophilized, and measured to 1 mg and resuspended in 1 mL of water. A dilution series was measured and a mass absorptivity of $0.298 \text{ (mg/ml}\cdot\text{cm)}^{-1}$ was calculated. The protein sample was measured to a concentration of 1.35 mM and aliquotted into 1 mL fractions (8 in total), flash frozen in $\text{N}_2(l)$, and stored at -80°C .

Multi-angle laser light scattering

A solution containing 500 μL of 5 mg/mL U- ^{13}C , ^{15}N -WNK1-(480-572) in 10 mM Tris pH=6.5, 10 mM NaCl, 1 mM DTT was passed through a 0.22 μM filter by centrifugation and loaded onto a Superdex 200 (10/300) column (GE) connected to a three-angle (47° , 90° , 131°) miniDAWN TREOS in tandem with a Optilab rEX (Wyatt) for measurement of scattering and refractive index. Average molecular weight was calculated using the ASTRA software suite (Wyatt) and plotted using DataGraph (Visual Data Tools).

2.6 Materials

Listed below are the buffers used in the purification of WNK1 (480-572). The Ni and MonoQ buffers are identical to those used in the purification of the WNK1 kinase domain. The gel-filtration buffer differs due to the necessary pH and salt considerations needed for NMR data collection; however, the autoinhibitory domain is stable over long periods of time and the buffer can be modified as necessary for biochemical/biophysical studies.

Table 2.4: Buffers for Purification of WNK1 (480-572)

Ni ²⁺ Buffer A	50 mM Tris pH=8.0 300 mM NaCl 20 mM Imidazole
Ni ²⁺ Buffer B	50 mM Tris pH=8.0 300 mM NaCl 250 mM Imidazole
MonoQ Buffer A	50 mM Tris pH=8.0 50 mM NaCl 1 mM EDTA 1 mM DTT
MonoQ Buffer B	50 mM Tris pH=8.0 500 mM NaCl 1 mM EDTA 1 mM DTT
Gel Filtration Buffer	10 mM Tris pH=6.5 10 mM NaCl 1 mM DTT

Chapter 3

NMR Data Collection and Structure Calculation of the WNK1 Autoinhibitory Domain

3.1 Introduction

3.2 Theory

3.2.1 Spin

Atoms and their constituent components can be accurately described by quantum mechanical postulates that predict, among other properties, the energy of electronic states, the probability densities of orbitals, and how the interaction of light with matter affect the physical states of the particles. Generally, chemical physics focuses on the electronic structure of atoms and the results of the interactions of the electron cloud with light (see Chapter 6 regarding X-ray crystallography). However, nucleonic energy states and the effects from their interactions with electromagnetic radiation can also be accurately described by quantum theory. Like macroscopic objects which have angular momentum given by directional rotation about an axis, subatomic particles have a quantized quantity called "spin angular momentum" that arises from the subatomic composition of nucleons. Since neutrons and protons both have spin $1/2$ quantities, any given atom with unpaired protons or neutrons has a magnetic moment along the spin axis. Classically, this magnetic moment can

be described by the following:

$$\vec{\mu}_n = \gamma_n \hbar \vec{I} \quad (3.1)$$

where μ_n is the magnetic moment for some nucleus n , γ_n is the gyromagnetic ratio of that nucleus and $\hbar \vec{I}$ is the spin angular momentum. As a result, the energy states of these atomic nuclei can be probed by exposure of these nucleons to a magnetic field which, for a spin 1/2 particle, will split the energy levels into +1/2 and -1/2 states. This phenomenon is known as the Zeeman effect. Assuming this magnetic field is oriented along the Z-axis, the Hamiltonian for the energy of the system can be written:

$$\begin{aligned} E_{system} = \mathcal{H} &= \int (\vec{\mu} \times \vec{B}_o) d\theta \\ &= -|\mu||B_o|\cos\theta \\ &= -\vec{\mu}\vec{B}_o \end{aligned} \quad (3.2)$$

where B_o is the strength of the external magnetic field. By substituting equation 3.1 and knowing that the energy levels are separated as $\pm 1/2$ energy states, we have

$$\begin{aligned} \mathcal{H} &= -\gamma_o S_z \\ E_\alpha &= -\frac{\gamma \hbar B_o}{2}, E_\beta = \frac{\gamma \hbar B_o}{2} \\ \Delta E &= E_\beta - E_\alpha = \gamma \hbar B_o \end{aligned} \quad (3.3)$$

$$\hbar\omega = \gamma \hbar B_o$$

$$\omega = \gamma B_o$$

where γ is the gyromagnetic ratio of the nucleus and S_z is the z-component of the spin-angular momentum. This equation describes the Larmor frequency as

the frequency of radiation (ω) that is absorbed by the nucleus under a specific magnetic field (B_o). Quantum states of subatomic particles and their associated energies can be described by the Schrödinger equation which equates the energy of the system to the Hamiltonian operator via an eigenfunction. This relation can either be represented in a time independent (Eqn 3.4) or time-dependent fashion (Eqn 3.5):

$$E\Psi = \mathcal{H}\Psi \quad (3.4)$$

$$i\hbar\frac{d}{dt}\Psi = -\frac{\hbar}{2m}\frac{d^2}{dx^2}\Psi + V_o\Psi \quad (3.5)$$

$$i\hbar\frac{d}{dt}\Psi = \mathcal{H}\Psi$$

To calculate the expectation values of energy for the system of eigenfuncations and eigenvalues, the integral of the eigenfunction is combined with its complex conjugate and the Hamiltonian operator.

$$\begin{aligned} \langle E \rangle &= \int \Psi^* \hat{\mathcal{H}} \Psi d\chi \\ &= \langle \Psi^* | \hat{\mathcal{H}} | \Psi \rangle \end{aligned} \quad (3.6)$$

However, even single-particle systems contain more than one energy term, and subsequently more than one wavefunction contributing to the system. Therefore, the arbitrary wavefunctions are composed as a linear combination of multiple functions and their coefficients. These wavefunctions can be represented as a matrix along with their associated operators (Hamiltonians). For a spin 1/2 particle, the wavefunctions, in Dirac notation, for the energy levels of the α and β states are:

$$\mu_\alpha = \begin{bmatrix} 1 \\ 0 \end{bmatrix}, \mu_\beta = \begin{bmatrix} 0 \\ 1 \end{bmatrix} \quad (3.7)$$

Since the value of the Z-component of the spin angular momentum, S_z , can take two values, $\pm \frac{\hbar}{2}$, combining these values with the associated wavefunctions for the α/β states produce

$$S_z = \begin{bmatrix} \langle \mu_\alpha | S_z | \mu_\alpha \rangle & \langle \mu_\alpha | S_z | \mu_\beta \rangle \\ \langle \mu_\beta | S_z | \mu_\alpha \rangle & \langle \mu_\beta | S_z | \mu_\beta \rangle \end{bmatrix} \quad (3.8)$$

Since μ_α and μ_β are orthonormal, this matrix reduces to

$$\begin{aligned} S_z &= \begin{bmatrix} (\frac{\hbar}{2})1 & (\frac{\hbar}{2})0 \\ (\frac{\hbar}{2})0 & (\frac{\hbar}{2})-1 \end{bmatrix} \\ &= \frac{\hbar}{2} \begin{bmatrix} 1 & 0 \\ 0 & -1 \end{bmatrix} \end{aligned} \quad (3.9)$$

This matrix will be used to represent the total spin angular momentum of the single particle along the Z-component. The remaining matrix operators for the X and Y components of the spin angular momentum are

$$S_x = \frac{\hbar}{2} \begin{bmatrix} 0 & 1 \\ 1 & 0 \end{bmatrix}, S_y = \frac{\hbar}{2} \begin{bmatrix} 0 & -i \\ i & 0 \end{bmatrix} \quad (3.10)$$

3.2.2 A single pulse experiment

Any one dimensional NMR experiment can be thought of a series of three steps 1) Preparation: the spin angular momentum of a spin 1/2 nucleon is oriented on the Z-axis along the moment of the applied magnetic field. 2) Excitation: radiofrequency electromagnetic radiation perturbs the energy state of the system and pushes the vector of the spin angular momentum into

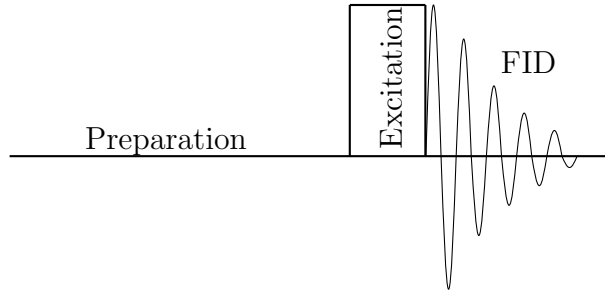


Figure 3.1: A one pulse NMR experiment

the transverse plane. 3) Free induction decay: the energy state of the nucleon undergoes free-precession about the transverse plane and undergoes a relaxation process to the preparation state. During this, the nucleon moves from a higher energy level to a lower energy and emits radiation in the radiofrequency range which can be detected by the instrument (Figure 3.1).

In the preparation stage, the integrated time-dependent Schrödinger equation has the general form

$$\Psi(t) = \Psi(0)e^{\frac{-iEt}{\hbar}} \quad (3.11)$$

and this can be applied, more specifically to the wavefunctions describing the energy states of the spin angular momentum of the 1/2 particle such that

$$\begin{aligned} \mu_\alpha(t) &= \mu_\alpha(0)e^{\frac{i\omega_s t}{2}} \\ \mu_\beta(t) &= \mu_\beta(0)e^{\frac{-i\omega_s t}{2}} \end{aligned} \quad (3.12)$$

The time dependency of the eigenfunction is described using the eigenvector

$$|+\rangle = \cos(\theta/2)e^{-i\phi/2}|\mu_\alpha\rangle + \sin(\theta/2)e^{i\phi/2}|\mu_\beta\rangle$$

for the total spin angular momentum \mathbf{S} . Applying the time-dependent equations from 3.10, the $|+\rangle$ vector wavefunction becomes:

$$\begin{aligned} |+\rangle &= \cos(\theta/2)e^{-i\phi/2}e^{i\omega_s t/2}|\mu_\alpha\rangle + \sin(\theta/2)e^{i\phi/2}e^{-i\omega_s t/2} \\ &= \cos(\theta/2)e^{-i(\phi-\omega_s)/2}|\mu_\alpha\rangle + \sin(\theta/2)e^{i(\phi-\omega_s)/2} \end{aligned} \quad (3.13)$$

From this, we find that the spin angular momentum proceeds around the vector of the induced \mathbf{B} field with an angular velocity of the Larmor frequency (ω_s) as was described in the classical picture. When the expectation value is calculated,

$$\begin{aligned} \langle S_z \rangle &= \langle + (t) | S_z | + (t) \rangle \\ &= [\cos(\theta/2)e^{i\phi t/2} \quad \sin(\theta/2)e^{-i\phi t/2}] \frac{\hbar}{2} \begin{bmatrix} 1 & 0 \\ 0 & -1 \end{bmatrix} \begin{bmatrix} \cos(\theta/2)e^{i\phi t/2} \\ \sin(\theta/2)e^{-i\phi t/2} \end{bmatrix} \\ &= \frac{\hbar}{2} [\cos^2(\theta/2) - \sin^2(\theta/2)] \\ &= \frac{\hbar}{2} \cos\theta \end{aligned} \quad (3.14)$$

we find that the Z-component of the spin angular momentum is time *independent*. However, the X-component of \mathbf{S} precesses about the XY plane at the Larmor frequency according to

$$\langle S_x \rangle = \frac{\hbar}{2} \sin(\theta) \cos(\phi - \omega_s t) \quad (3.15)$$

However, this component of the spin is averaged out due to decoherence arising as a product of a Boltzmann distribution of spin populations.

During the second phase of the one-pulse experiment, the spin system is excited by a radiofrequency pulse. The effect of this RF pulse is a rotation about the Z-axis in a time-dependent fashion at a rate of $\omega_r t$. Because the

collection of spins can now be thought of as a Boltzmann population, the expectation value of the population density (ρ_{S_z}) undergoing rotation (R) induced by the RF pulse can be expressed as

$$\rho'_S = R\rho_{S_z}R^* \quad (3.16)$$

where

$$R = \begin{bmatrix} \cos(\theta/2) & -i\sin(\theta/2)e^{-i\phi} \\ -i\sin(\theta/2)e^{i\phi} & \cos(\theta/2) \end{bmatrix} \quad (3.17)$$

When the rotation angle (θ) is oriented at 90° and the direction of the pulse is along the X direction ($\phi=0^\circ$)

$$\begin{aligned} R &= \begin{bmatrix} \cos(\pi/4) & -i\sin(\pi/4)e^{-i\phi} \\ -i\sin(\pi/4)e^{i\phi} & \cos(\pi/4) \end{bmatrix} \\ &= \frac{1}{\sqrt{2}} \begin{bmatrix} 1 & -i \\ -i & 1 \end{bmatrix} \end{aligned} \quad (3.18)$$

When the expectation value of the density matrix for the resulting effect of the rotation wavefunction on the Z-component of the spin angular momentum is calculated,

$$\begin{aligned} \rho'_{S_z} &= R_x S_z R_x^* \\ &= \frac{1}{\sqrt{2}} \begin{bmatrix} 1 & -i \\ -i & 1 \end{bmatrix} \frac{1}{2} \begin{bmatrix} 1 & 0 \\ 0 & -1 \end{bmatrix} \frac{1}{\sqrt{2}} \begin{bmatrix} 1 & i \\ i & 1 \end{bmatrix} \\ &= \frac{1}{2} \begin{bmatrix} 0 & i \\ -i & 0 \end{bmatrix} = S_y \end{aligned} \quad (3.19)$$

The resulting density matrix is equivalent to the S_y component of the spin angular momentum from equation 3.8. The free induction decay following excitation proceeds under the Hamiltonian ($-\omega_s S_z$) describing the influence of the \mathbf{B}_o field on the spin angular momentum

$$\Psi(t) = e^{-i\mathcal{H}t/\hbar}\Psi(0) \quad (3.20)$$

The time evolution described by the Schrödinger equation following the 90° pulse is

$$\begin{aligned}
\rho_f(t) &= e^{i\omega_s t S_z} \rho_{S_z} e^{-i\omega_s t S_z} \\
&= \frac{1}{2} \begin{bmatrix} e^{i\omega_s t/2} & 0 \\ 0 & e^{-i\omega_s t/2} \end{bmatrix} \begin{bmatrix} 0 & i \\ -i & 0 \end{bmatrix} \begin{bmatrix} e^{-i\omega_s t/2} & 0 \\ 0 & e^{i\omega_s t/2} \end{bmatrix} \\
&= \begin{bmatrix} 0 & e^{i\omega_s t/2} \\ e^{-i\omega_s t/2} & 0 \end{bmatrix} \\
&= \begin{bmatrix} 0 & i(\cos(\omega_s t) + i\sin(\omega_s t)) \\ -i(\cos(\omega_s t) - i\sin(\omega_s t)) & 0 \end{bmatrix} \\
&= \vdots \\
&= \frac{1}{2} [-S_y \cos(\omega_s t) - S_x \sin(\omega_s t)]
\end{aligned} \tag{3.21}$$

This shows that the spin angular momentum following the excitation precesses about the XY plane at an angular velocity of ω_s . The FID is detected in quadrature as defined by

$$I^+ = I_x + iI_y = \frac{1}{2} \begin{bmatrix} 0 & 1 \\ 1 & 0 \end{bmatrix} + \frac{1}{2} \begin{bmatrix} 0 & -i \\ i & 0 \end{bmatrix} = \frac{1}{2} \begin{bmatrix} 0 & 1 \\ 0 & 0 \end{bmatrix} \tag{3.22}$$

The expectation value of the quadrature-detected signal is given by the trace of the product of the final density matrix ρ_f with I^+

$$\begin{aligned}
\langle I^+ \rangle &= \text{Trace} \left(\begin{bmatrix} 0 & 1 \\ 0 & 0 \end{bmatrix} \begin{bmatrix} 0 & ie^{i\omega_s t} \\ -ie^{-i\omega_s t} & 0 \end{bmatrix} \right) \\
\langle I^+ \rangle &= -ie^{-i\omega_s t}
\end{aligned} \tag{3.23}$$

The fourier transform of this equation from the time dimension to frequency gives a uniform peak at ω_s .

3.2.3 The chemical shift

In an NMR experiment, when a spectrum is collected there is not a single uniform peak but, many peaks spread across the spectral width. The place-

ment of these peaks are attributed to the chemical shift. This phenomenon arises from the *electronic* environment surrounding the nuclei being investigated. The electronic environment is induced by the \mathbf{B}_o field to produce a smaller, localized magnetic field which can act as a shield for the nearby nuclei from the general \mathbf{B}_o field represented as:

$$B = (1 - \sigma)B_o \quad (3.24)$$

where σ is the shielding factor. This can be applied to the classical model affecting the precession frequency ω such that

$$\omega = -\gamma(1 - \sigma)B_o \quad (3.25)$$

The chemical shift for specific compounds are often used as reference signals, such as tetramethyl silane (TMS) and 4,4-dimethyl-4-silapentane-1-sulfonate (DSS). Using these reference markers, individual spectra collected on multiple instruments of varying strength can be compared accurately due to the reference signal by the chemical shift expressed in $\delta(ppm)$

$$\delta(ppm) = (\sigma_{ref} - \sigma) \times 10^6 = \frac{\Omega - \Omega_{ref}}{\omega_s} \times 10^6 \quad (3.26)$$

3.2.4 Many spin systems

In multidimensional heteronuclear NMR spectroscopy, two spin systems connected by a chemical bond (in the case of a $^1\text{H}, ^{15}\text{N}$ -HSQC, the H-N amine bond of the backbone amide or sidechain Arg, Lys, Asn, Gln) have a combined initial density matrix described by

$$\rho = \gamma_H I_z + \gamma_N S_z \quad (3.27)$$

where I_z is the Z-component of the spin angular momentum for the proton and S_z is that of the nitrogen nuclei and γ_H/γ_N are the gyromagnetic ratios of the respective nuclei. Since the protons and nitrogens in proteins are covalently linked, the electronic nature of the bond influences the local \mathbf{B}_o field effect on the protein under investigation. Qualitatively, the induction of these small fields give rise to the splitting effect in the spectra of two coupled spins and is proportional to the type of bonded nuclei and the number of bonds linking them. This scalar (J) coupled splitting is measured by looking at the frequency difference between the two spins

$$\Delta\omega \propto \pm\gamma_H\gamma_N \quad (3.28)$$

In a quantum description, one find that the α/β states of the coupled spins combine into four new basis vectors representing the four spin states that the nuclei can reside in. (Figure 3.2) The interaction of these spin states in the atoms being assessed is essential for transferring the magnetization from the proton to the other nuclei and detecting its chemical shift. To illustrate this, a $^1\text{H}, ^{15}\text{N}$ -HSQC will be used as an example. The pulse sequence for the HSQC spectrum is presented graphically as Figures 3.3 and 3.4.

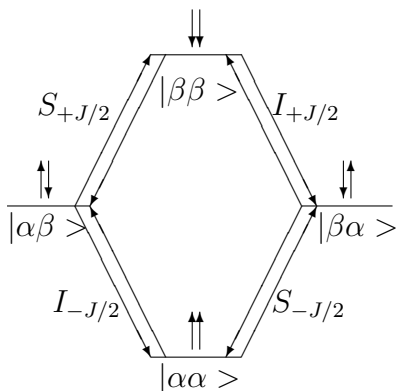


Figure 3.2: Spin energy levels in a 2-spin coupled system

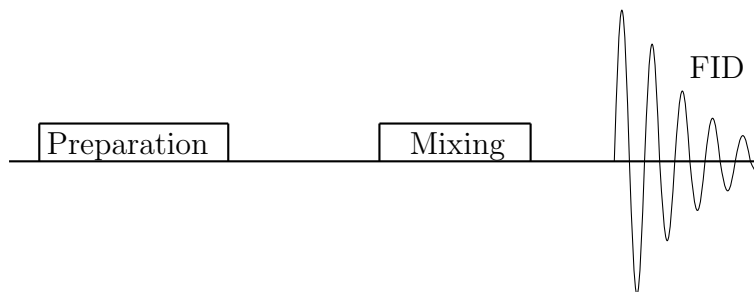


Figure 3.3: A general outline of a multidimensional experiment

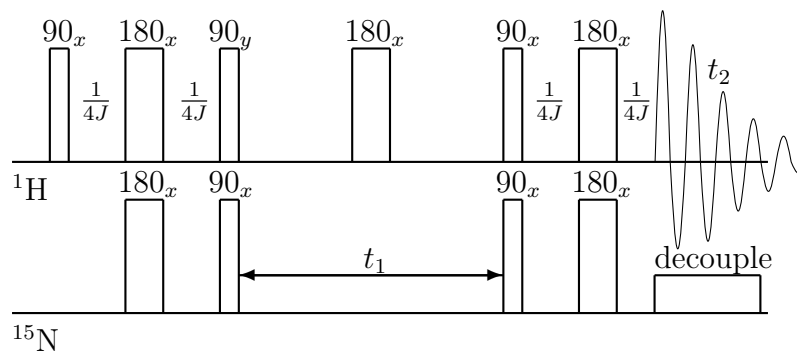


Figure 3.4: Outline of a $^1\text{H}, ^{15}\text{N}$ -HSQC experiment

For a single quantum coherence spectrum, an initial 90° pulse along the x dimension converts the Z-component of the spin angular momentum of the proton into the transverse plane along $-I_y$ (in a similar fashion to what was described in a single-spin, single-pulse experiment). During this process, the pulse is refocused by a 180° pulse and the density matrix evolves under scalar coupling (J) such that

$$\begin{aligned}
-I_y &\xrightarrow{180^\circ_{I_x}} -[I_y \cos(\phi) - 2I_x S_z \sin(\phi)] \\
&\xrightarrow{180^\circ_{S_x}} -[-I_y \cos(\phi) - 2I_x S_z \sin(\phi)] \\
&\xrightarrow{J} \cos(\phi)[I_y \cos(\phi) - 2I_x S_z \sin(\phi)] - \sin(\phi)[2I_x S_z \cos(\phi) + I_y \sin(\phi)] \\
&= I_y \cos(2\phi) - 2I_x S_z \sin(2\phi)
\end{aligned} \tag{3.29}$$

If the delay (ϕ) is set at $1/4$ of the N-H scalar coupling value, the density matrix will evolve to:

$$\rho = -2I_x S_z \tag{3.30}$$

The second 90° proton pulse along y flips the density matrix to

$$\rho = -2I_z S_y \tag{3.31}$$

The combination of these $90^\circ \rightarrow 180^\circ \rightarrow 90^\circ$ pulses are known as an INEPT (insensitive nuclei enhanced by polarization transfer) sequence. Once the magnetization is transferred to the nitrogen nuclei, the chemical shift of the proton does not evolve since the spin angular momentum of I is transverse and, therefore, not time dependent. The evolution due to J coupling only occurs as a shift in sign due to the $180^\circ_{I_x}$ refocusing pulse. What does evolve during t_1 is

the chemical shift associated with the nitrogen according to

$$2I_zS_y \xrightarrow{\omega_s t_1} 2I_z[S_y \cos(\omega_s t_1) - S_x \sin(\omega_s t_1)] \quad (3.32)$$

To return the magnetization to the proton for detection, a reverse INEPT transfer sequence converts the first component of equation 3.32 since the second term results in a double quantum transition that is not detectable.

$$2I_zS_y \cos(\omega_s t_1) \rightarrow 2I_yS_z \cos(\omega_s t_1) \quad (3.33)$$

The detected signal, therefore, with quadrature is

$$S(t_1, t_2) = \cos(\omega_s t_1) e^{i\omega_I t_2} \quad (3.34)$$

3.2.5 3D experiments for backbone and sidechain assignments

In a similar fashion to that of a two-spin, through-bond experiment, 3D NMR experiments for assigning backbone and sidechain chemical shifts for individual atoms utilize through-bond coupling. These experiments link the magnetically active nuclei ^1H , ^{15}N and ^{13}C utilizing the types of bonds along the protein backbone and in the sidechains of each amino acid. The 3D experiment can be thought of in a similar diagram to that of a 2D experiment presented in Figure 3.3. However, in a three dimensional experiment, there are two mixing events following the preparation stage. For the assignment of backbone amide chemical shifts, two experiments were utilized: the HNCACB and the CBCA(CO)NH (Figures 3.5 and 3.6).

The HNCACB spectrum is a type of 3D experiment known as an "out-

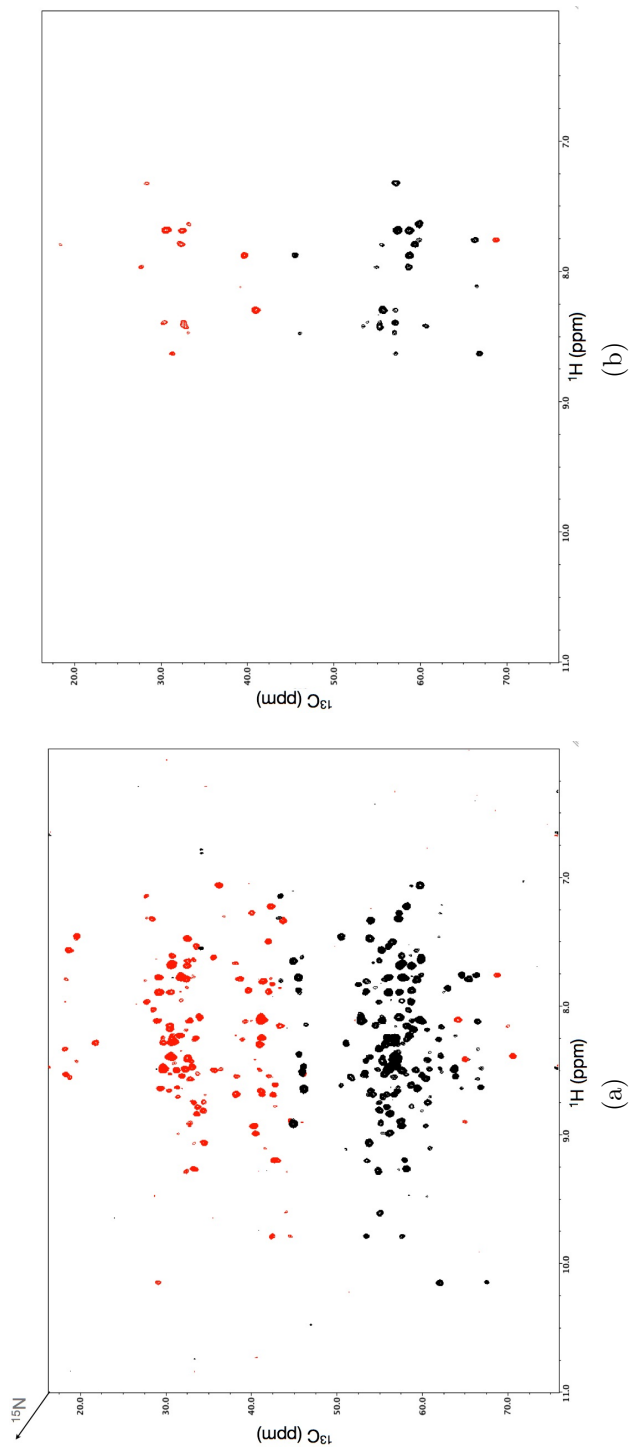


Figure 3.5: HNCACB of U- ^{15}N , ^{13}C -WNK1 (480-572). a) Projection along the Z-axis of the ^{15}N chemical shift. b) A sample spectrum along a single value of the ^{15}N chemical shift. Peaks shown in red are aliased and correspond to the C_β of the backbone sidechain.

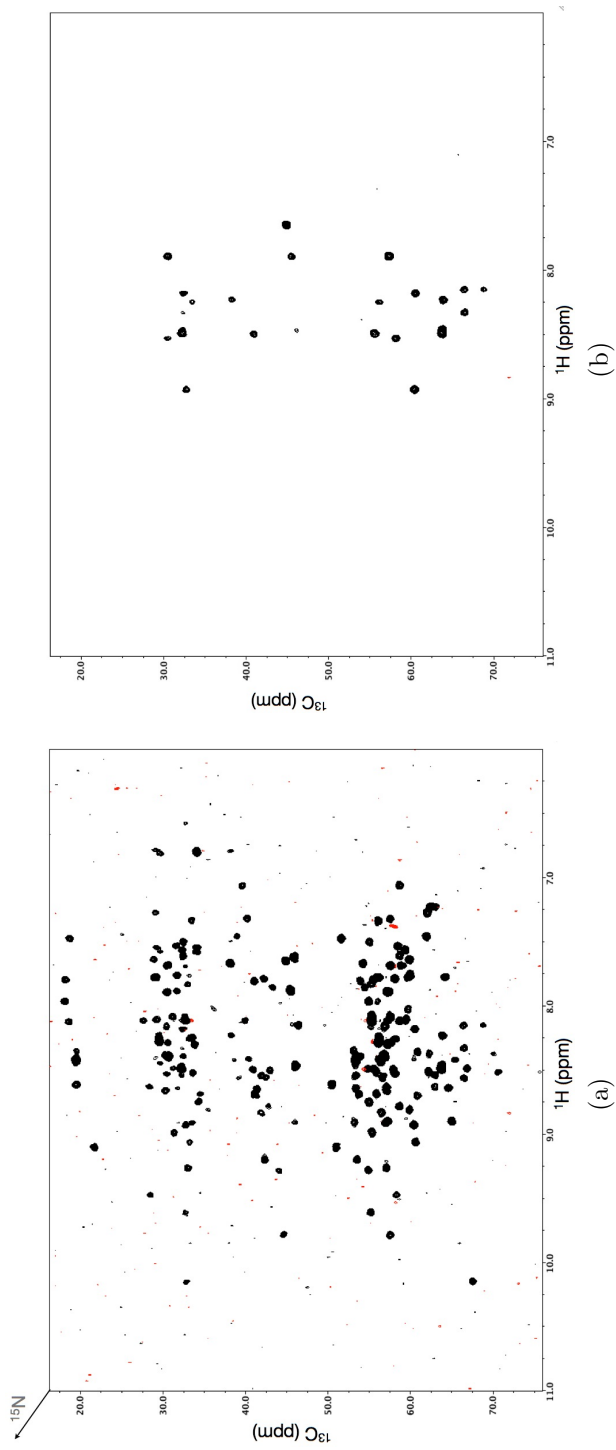


Figure 3.6: CBCA(CO)NH of U- ^{15}N , ^{13}C -WINK1 (480-572). a) Projection along the Z-axis of the ^{15}N chemical shift. b) A sample spectrum along a single value of the ^{15}N chemical shift.

and-back.” The magnetization begins on the amide proton in the backbone of the polypeptide chain and is transferred to the nitrogen using an INEPT-type sequence. The magnetization is then transferred to the C_α carbon of both the i and $i-1$ residues. This process can occur because the double and single bond J coupling constants between the amide and adjacent C_α are approximately equivalent, although the peaks corresponding to the $i-1$ sidechain C_α and C_β will have weaker intensity. The magnetization is then mixed with the C_β and transferred back to the proton (via the nitrogen) for detection (Wittekind and Mueller, 1993; Kay et al, 1990). The spectrum as seen in Figure 3.5, has both directly detected and aliased peaks corresponding to C_α and C_β , respectively.

The second 3D experiment used to assign backbone chemical shifts is the CBCA(CO)NH (Grzesiek and Bax, 1992). This experiment can be thought of as a ”straight through” experiment because the magnetization begins associated with the sidechain protons and is transferred to the side chain carbons of the $i-1$ residue and, finally, on to the amide nitrogen and proton of the i residue via the carbonyl carbon (which is not detected due to constant-time-separated pulses). Because there is information for the $i-1$ residue only, this spectrum can be compared to the HNCACB, and the i residue can be linked to the preceding $i-1$ residue through the known sequence by looking for specific amino acids throughout the sequence such as glycine and serine/threonine (which have unique chemical shifts for C_α and C_β), an accurate assignment can be made. An example of the linkage process using these two spectra can be seen in Figure 3.7. Each strip shown corresponds to the ^1H in the X-dimension,

^{13}C in the Y-dimension and a specified ^{15}N chemical shift along the Z.

Once the backbone amides have been assigned, the remainder of the sidechain carbons and their associated protons can be assigned utilizing three experiments involving TOtal Correlation SpectroscopY (TOCSY). The first of these is the (H)C(CO)NH-TOCSY which, as a "straight-through" method, correlates all of the backbone carbons and their associated chemical shifts from the $i - 1$ residue with the i proton-amide chemical shift (Grzesiek et al, 1993). The number of peaks associated with sidechain carbons and their chemical shifts can be used to assess whether the assignment of the backbone is accurate. To find the proton chemical shifts for the associated hydrogens attached to the side chain carbons, the H(CCO)NH-TOCSY is used. This experiment is similar to the (H)C(CO)NH-TOCSY in that it is a "straight-through" method and looks at the protons attached to sidechain carbons from the $i - 1$, residue and the magnetization is detected through the amide proton of the i residue (Grzesiek et al, 1993; Montelione et al, 1992). To check the corresponding assignments from these two experiments, the HCCH-TOCSY experiment is used (Bax et al, 1990). This correlates the proton associated with sidechain carbons by mixing of the magnetization along the entire carbon sidechain and then transferring back to the sidechain protons for detection (Figure 3.10).

Finally, to measure interproton distances, an F2-(^{13}C , ^{15}N)-edited NOESY (also called the Mother-NOESY) was collected (Xia et al, 2003). This experiment begins by transferring the magnetization from protons in the polypeptide being investigated through space to adjacent protons via dipolar

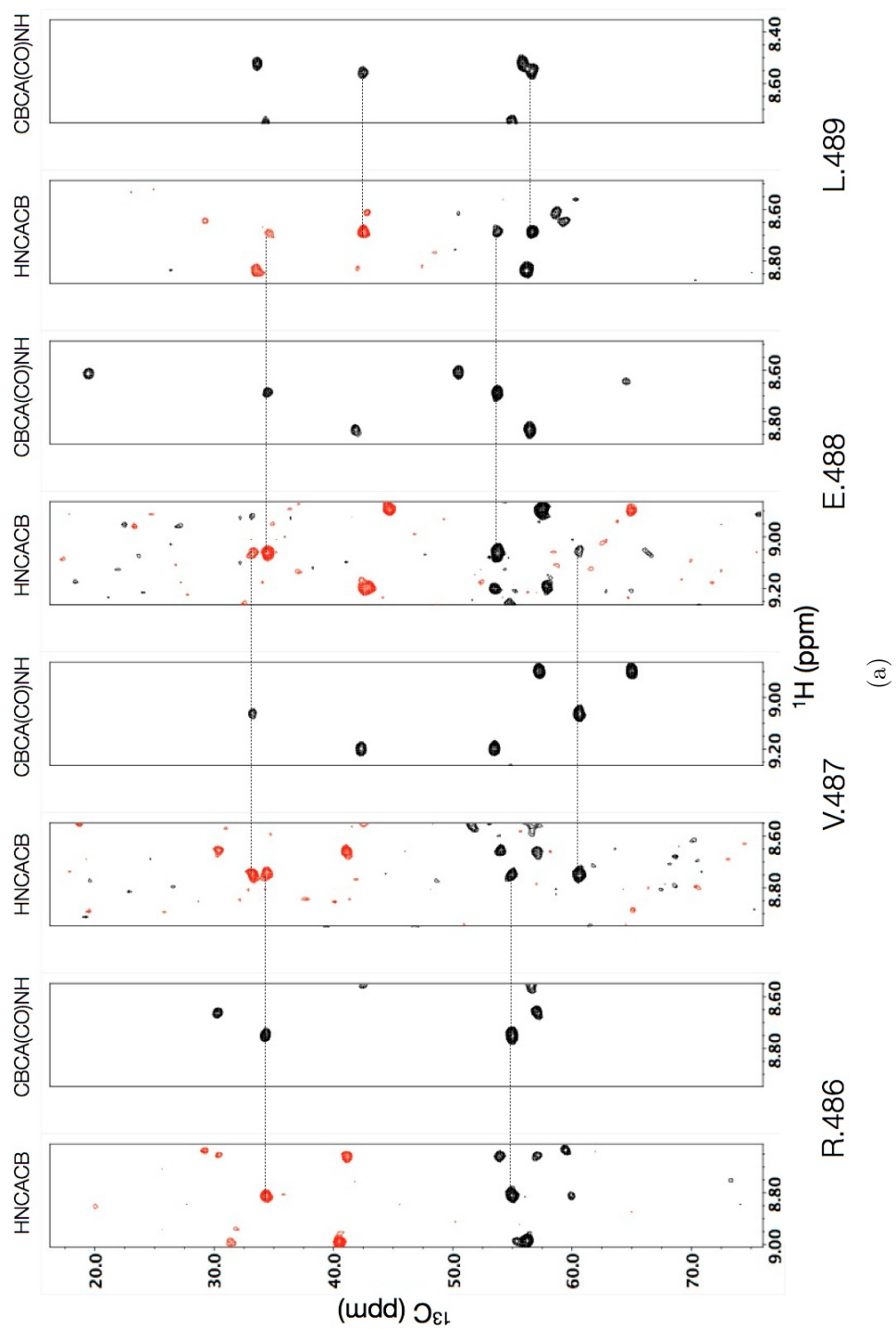


Figure 3.7: Sample connectivity for backbone assignment of U- ^{15}N , ^{13}C -WINK1 (480-572)

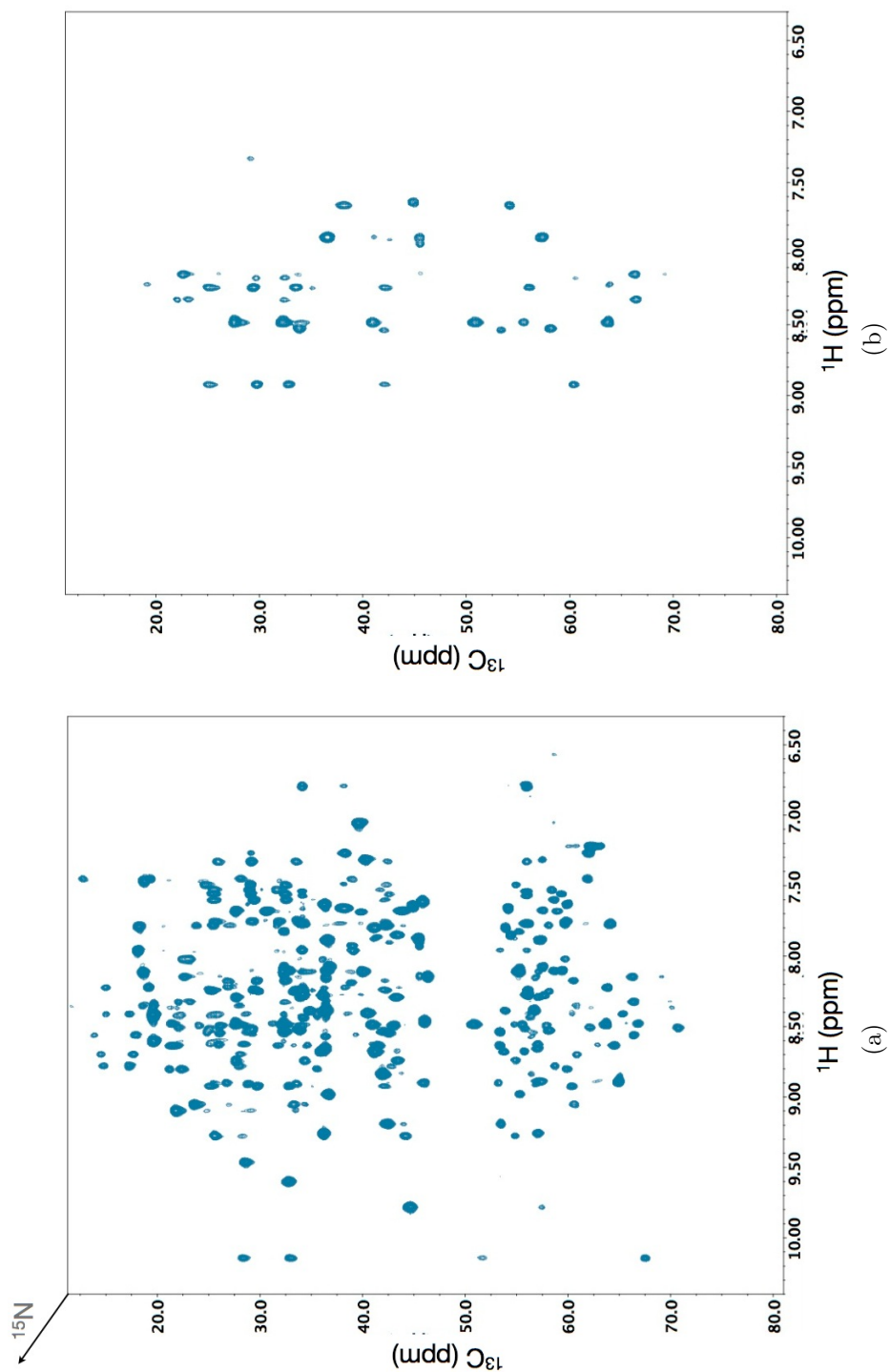


Figure 3.8: $(\text{H})\text{C}(\text{CO})\text{NH-TOCSY}$ of $\text{U-}^{15}\text{N}$, ^{13}C -WINK1 (480-572). a) Projection along the Z-axis of the ^{15}N chemical shift. b) A sample spectrum along a single value of the ^{15}N chemical shift.

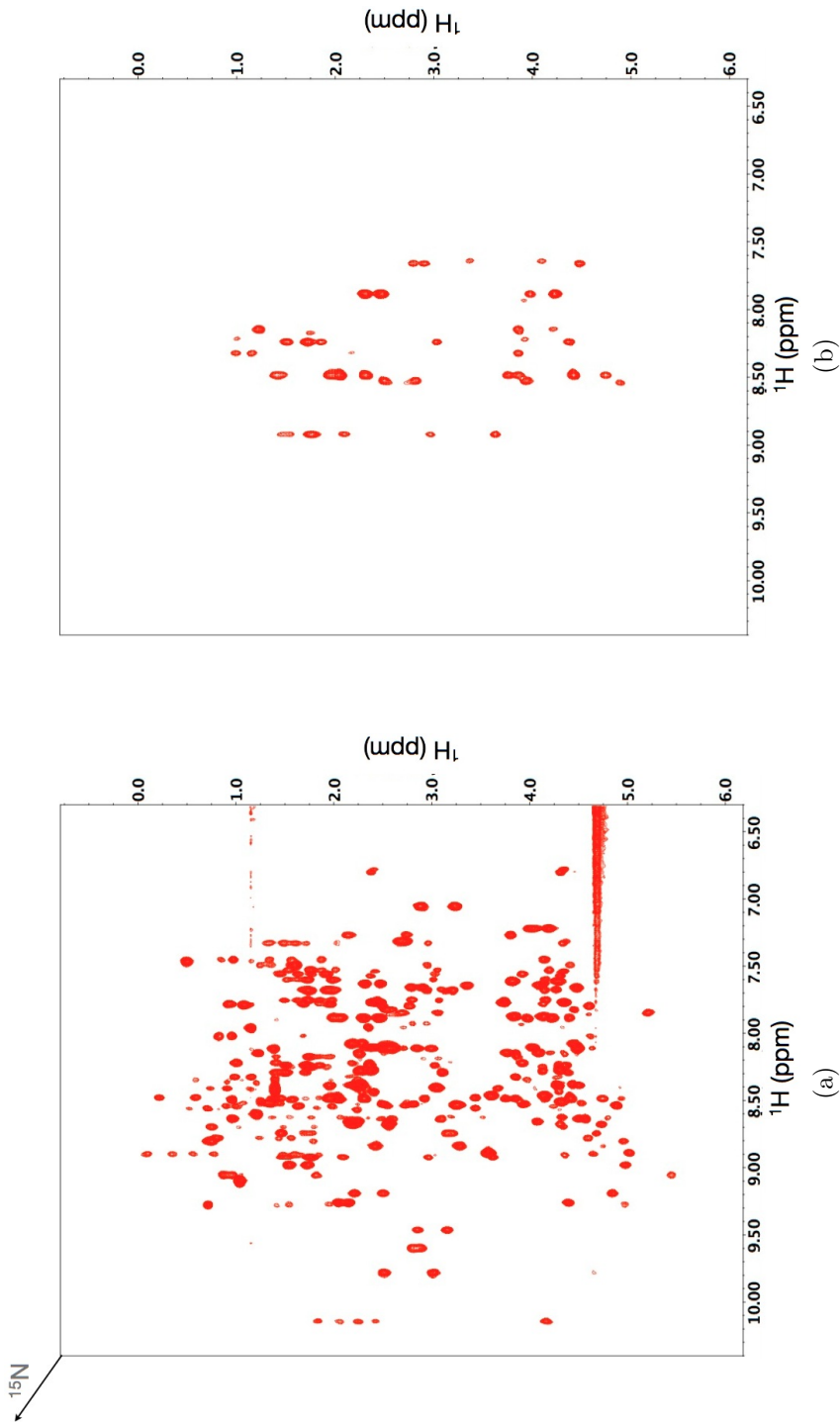


Figure 3.9: H(CCO)NH-TOCSY of U- ^{15}N , ^{13}C -WINK1 (480-572). a) Projection along the Z-axis of the ^{15}N chemical shift. b) A sample spectrum along a single value of the ^{15}N chemical shift.

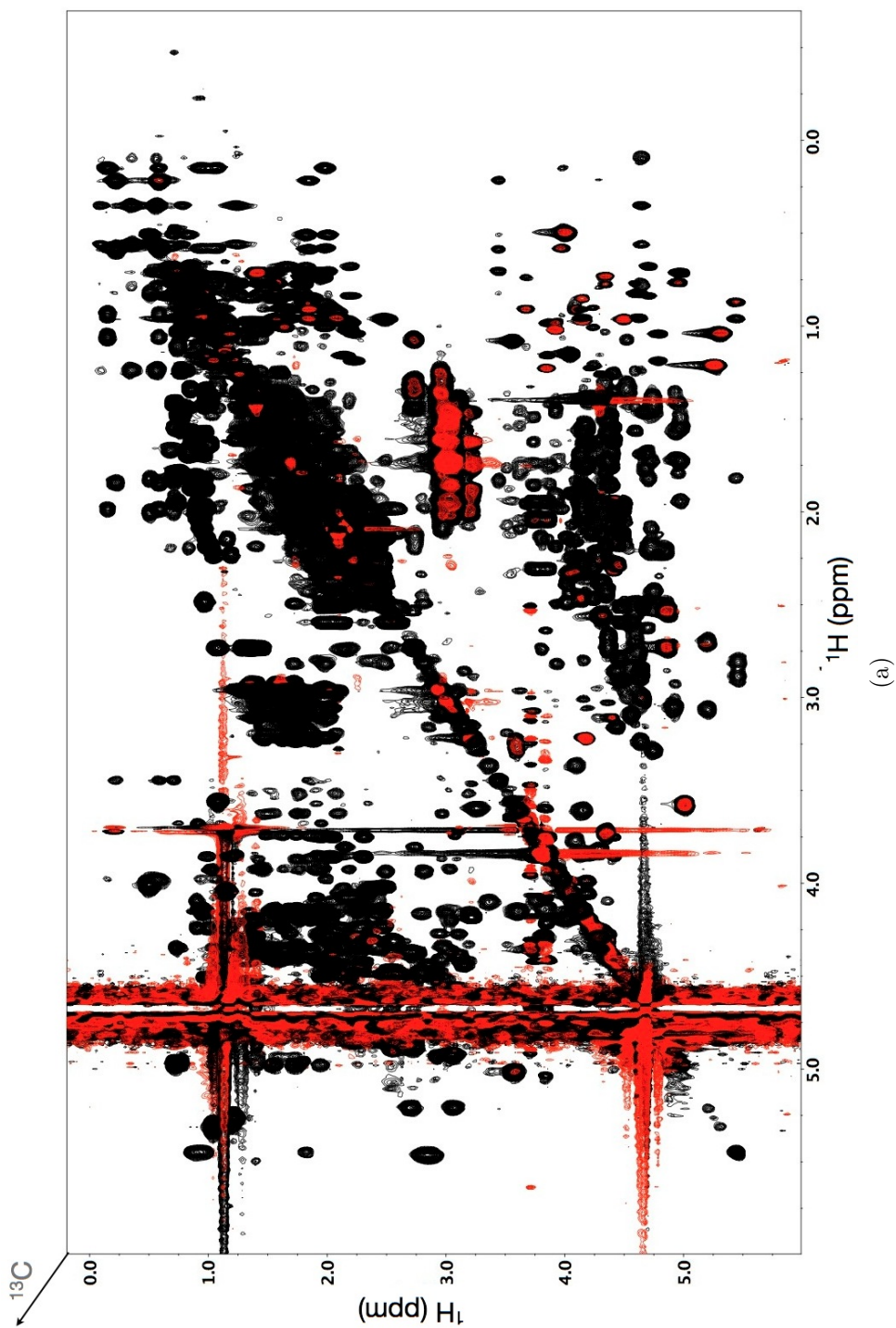


Figure 3.10: HCCH-TOCSY of U- ^{15}N , ^{13}C -WNK1 (480-572). The spectrum shown is a projection along the Z-axis of the ^{13}C chemical shift. Peaks shown in red are aliased.

coupling. The rate of this transition is a function of the gyromagnetic ratio of the atomic nuclei being transferred and the inter-nuclei distance as shown by

$$W_k \propto \frac{\gamma^4 \hbar^2}{r^6} \quad (3.35)$$

where W_k is the rate of magnetization transfer. Once the mixing step is completed the magnetization is transferred to nearby ^{15}N and ^{13}C via J coupling. The chemical shift for both the ^{15}N and ^{13}C evolve under time-simultaneous conditions and are transferred back to the attached protons for detection. The deconvolution of the spectra is achieved by detecting in quadrature with the TPPI-states method (Marion et al, 1989). A Hadamard matrix (Kupce et al, 2003) is used during processing to generate nuclei-specific spectra as seen in Figures 3.11 and 3.12.

3.3 Materials and Methods

3.3.1 Data collection and manipulation

Experiments for assignment and structural analysis were conducted at 35°C using an 800 MHz Varian INOVA spectrometer equipped with a cryogenically cooled probe for ^1H , ^{15}N , ^{13}C detection with Z-axis pulsed field gradient. Samples containing 650 μM U- ^{13}C , ^{15}N - WNK1-(480-572) were used to collect 3D HNC0, HNCACB, CBCA(CO)NH and HCCH-TOCSY experiments for chemical shift assignments (Cavanagh et al, 2007). Restraints from interproton distances were obtained from F2-(^{13}C , ^{15}N)-edited NOESY spectra (120ms).

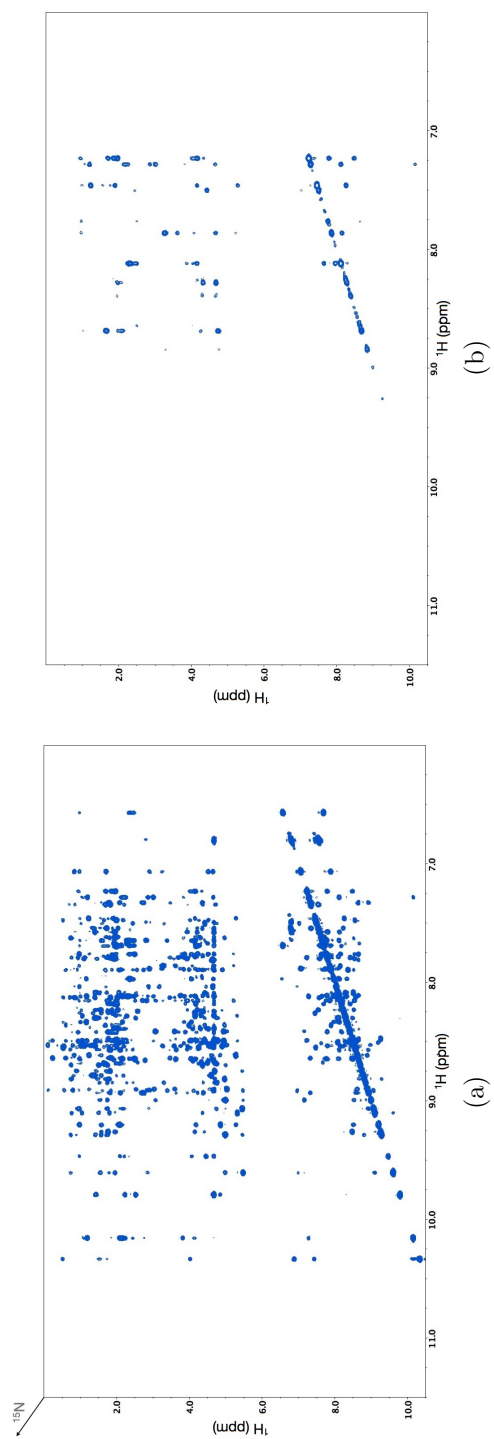


Figure 3.11: ^{15}N -NOESY of U- ^{15}N , ^{13}C -WINK1 (480-572). a) Projection along the Z-axis of the ^{15}N chemical shift. b) A sample spectrum along a single value of the ^{15}N chemical shift.

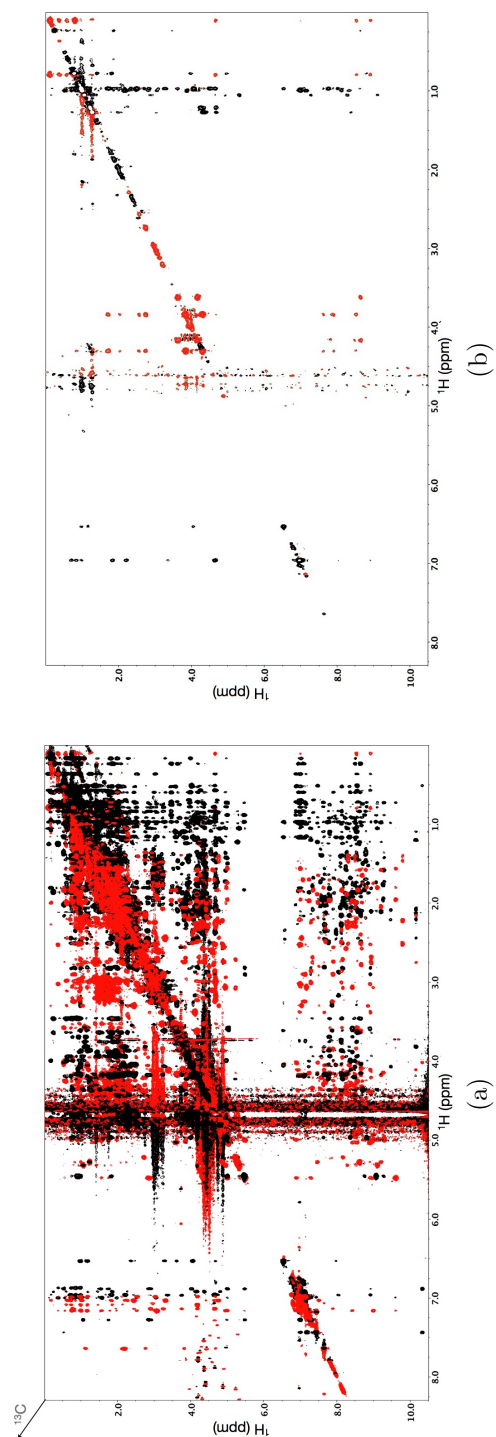


Figure 3.12: ^{13}C -NOESY of U- ^{15}N , ^{13}C -WNK1 (480-572). a) Projection along the Z-axis of the ^{13}C chemical shift. Red peaks shown are aliased. b) A sample spectrum along a single value of the ^{15}N chemical shift.

Experiments for titration analysis were implemented using a 600 MHz Varian INOVA spectrometer at 35°C with a similar cryoprobe as stated above. Spectra were serially collected following introduction of titrant to the sample. Penta and dodecameric peptides NH₂-GRFKV-NH₂, NH₂-GAFKV-NH₂ and NH₂-GTLKTYLKRFKVMKIKVLRN-NH₂ were synthesized on site in the UT Southwestern Protein Chemistry Technology Center. Shift in chemical shift was measured employing the equation $\Delta\delta = ((\Delta\delta_{HN})^2 + (\frac{1}{5}\Delta\delta_N)^2)^{1/2}$ (Grzesiek et al, 1996). All data were processed in NMRPipe (Delaglio et al, 1995) and analyzed by NMRviewJ (One Moon Scientific).

3.3.2 Structure calculation

Structure calculations for WNK1-(480-572) were performed using ARIA v2.3 (Nilges et al, 1997) using dihedral angle restraints calculated from ¹³C α , ¹³C β , ¹⁵N, and ¹H chemical shifts using TALOS (Shen et al, 2009) with the dihedral angle restraints set at twice the standard deviation provided by TALOS. A two-step structure calculation was performed where, in the first step, ARIA began with an unfolded polypeptide and found a stable fold of the domain. The lowest energy structure from the initial step was used as a starting scaffold to complete the structure using unambiguous and ambiguous restraints. From iteration 0 \rightarrow iteration 7, 20 structures were calculated per iteration and a final 500 structures were generated in iteration 8. During refinement in vacuo and in the presence of water, 20 structures were generated. Analysis was completed by Procheck-NMR (Laskowski et al, 1996) and the chemical shifts used

for the calculation were deposited in the Biological Magnetic Resonance Data Bank (www.bmrb.wisc.edu).

Chapter 4

Solution Structure and Biochemical Characterization of the WNK1 Autoinhibitory Domain

4.1 Introduction

The involvement of WNK1 in the regulation of salt balance hinges on its interaction with its substrates OSR1/SPAK and their subsequent activation of NKCCs through a kinase-dependent mechanism. This process is highlighted in the distal convoluted tubule of the kidney where the reuptake of salt from the urinary lumen is important in maintaining levels of potassium and chloride ions in the blood. This signal transduction pathway hinges on the interaction of the OSR/SPAK kinases with WNK1 and the NKCCs via the presence of a small peptide binding domain located on OSR1/SPAK. It was initially shown that a small peptide motif (RFXV) located on the N-terminus of NKCC1 was necessary for localizing SPAK to the N-terminus of NKCC1 and phosphorylation of T217 Piechotta et al (2002). The crystal structure of the domain necessary for this binding event, called the PASK/FRAY homology 2 (PF2) domain, was solved in complex with a 6-mer GRFQVT peptide derived from the C-terminus of WNK4. The presence of two acidic residues (1 Asp, 1 Glu) and their interactions with the guanidinium group from the arginine in the

peptide was shown to characterize the primary mode of binding for the domain to the peptide motif Villa et al (2007).

An autoinhibitory domain was found in initial biochemical studies of the WNK1 kinase. Recombinant expression of the kinase *in cis* with the autoinhibitory domain was found to have no autophosphorylation activity or activity toward the general kinase substrate myelin basic protein (MBP) Xu et al (2002). This regulatory domain was also found to inhibit the kinase domain *in trans* in a dose-dependent fashion. Here, we present the solution structure of the WNK1 autoinhibitory domain and characterize its interactions with 5 and 20-residue RFXV-containing peptides derived from the WNK1 kinase domain in an effort to understand the structural relationship to the OSR1-PF2 domain and gain insights into the mechanism of autoinhibition.

4.2 Results

4.2.1 Bioinformatic approach

As initially described by Xu *et al.*, the *R. norvegicus* WNK1 autoinhibitory domain was characterized for residues 485-555. In attempt to isolate the domain, a GST-tagged version was expressed in *E. coli* and purified. Following thrombin cleavage of GST, precipitation was observed (data not shown). In hopes of optimizing the construct by refining the length of the domain, an NCBI-BLAST search of the expressed sequence (WNK1-485-555) revealed that the autoinhibitory domain is a paralog of the OSR1-PF2 domain with 28% similarity as identified by a BLOSUM62 score analysis (Figure 4.1a)

and is conserved among all autoinhibitory domains for WNK family members.

The outlined region in Figure 1 is the RFXV binding site for the OSR-PF2 domain is identified by this alignment. The locus of the highest sequence conservation between the OSR-PF2 and the WNK1-AI domains contains the OSR-PF2 binding site for an RFXV peptide. Four key peptide binding residues which form the binding cleft (two phenylalanines and two acidic residues) were identified previously in the crystal structure of the PF2 domain. The two phenylalanines first highlighted by Xu, *et al* and then later showed to be important for forming the hydrophobic core of the OSR1-PF2 domain by Villa *et al* are both wholly conserved in all autoinhibitory domains of the WNKs, except for one case in WNK3 from *D. rerio* where, in the second position, it is replaced by a tyrosine. The two acidic residues responsible for binding the guanidinium group from the arginine in the RFXV motif as characterized in the OSR1-PF2 domain structure are conserved as well. The identity of the second acidic residue is entirely conserved as a glutamate, likely due to its relative position along the first alpha helix. There is a preponderance of conservation of aspartic acid at the first acidic site, although it is substituted as a glutamate in all of the WNK2 autoinhibitory domains that we investigated using our bioinformatics query.

In investigating this domain, the BLAST and initial Rosetta *ab initio* results indicated that the homology of the PF2 domain in the WNK1 sequence extended beyond the previously published boundaries to include residues 480-572. Upon further analysis, we found that the architecture of the protein was

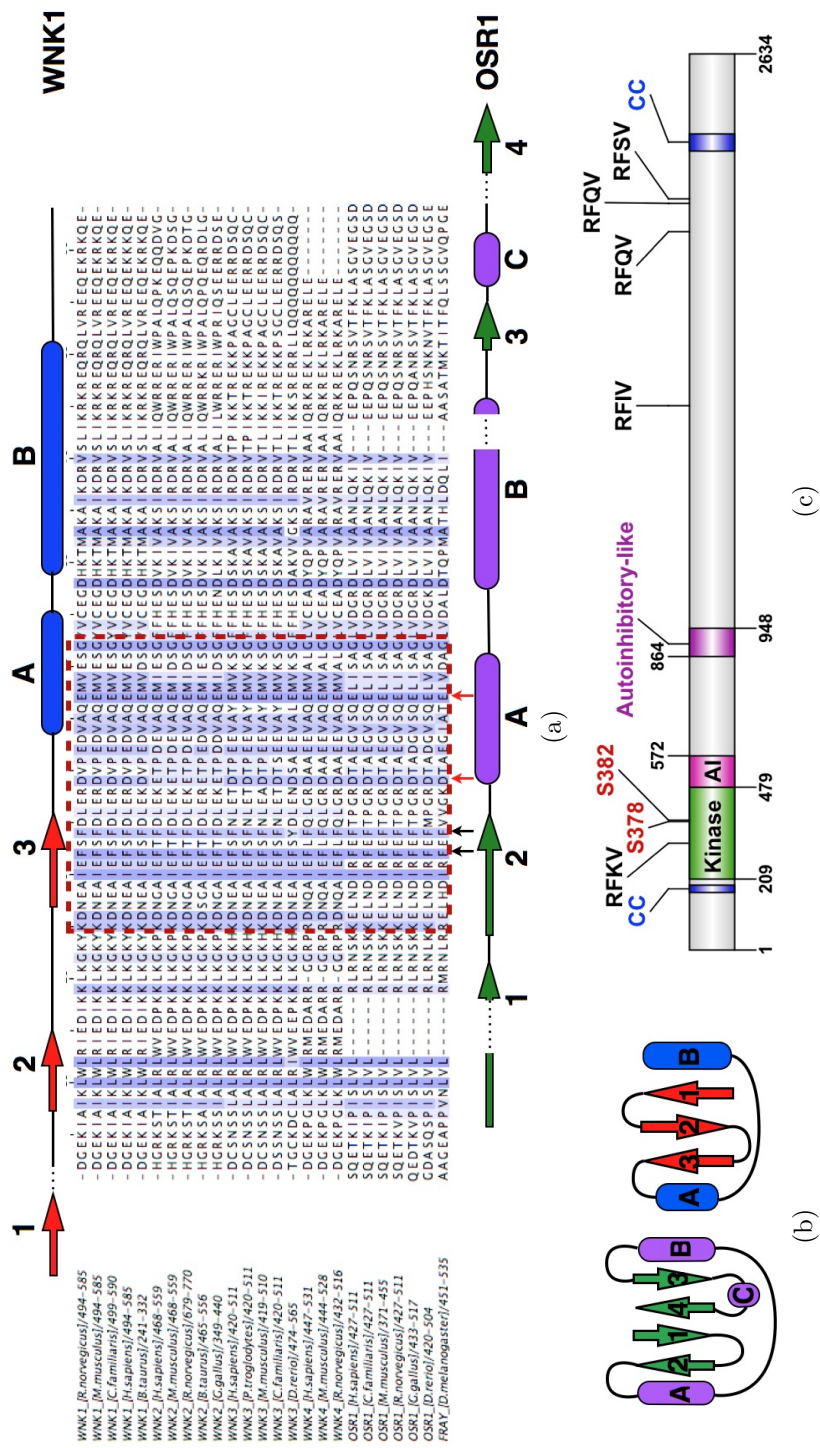


Figure 4.1: a) Multiple Sequence alignment of autoinhibitory domains of the four known WNK isoforms from several vertebrate species compared to the PF2 domains from OSR1. There is a 28% sequence identity between the two domains with a higher level of conservation occurring at the RFXV binding site denoted by arrows at the bottom of the alignment. The two aromatic residues that are necessary for forming the hydrophobic core of the domain are universally conserved (black arrows) and the acidic residues shown to be important for binding the RFXV arginine are also wholly conserved across isoforms and species (red arrows). b) Domain architecture of the OSR-PF2 domain (green/purple) compared to that of the WNK1 autoinhibitory domain (red/blue) with β strands depicted as arrows and α helices depicted as oblate spheroids. c) Linear domain diagram showing the newly defined domain boundaries for the WNK1 autoinhibitory domain as well as a previously unidentified autoinhibitory-like (AIL) domain located between residues 864-948

likely modified. Instead of terminating in a β -strand as found in the PF2 domain, the autoinhibitory domain was predicted to terminate with the two conserved α helices. It was predicted that this would be effected through the removal of the penultimate C-terminal strand found in the PF2 domain and the prediction of a non-homologous strand in the N-terminus of the autoinhibitory domain encompassing residues 482-489. This relationship is shown graphically in Figure 1b as the reordering of $\beta 4$ in the PF2 domain to $\beta 1$ of the autoinhibitory domain with the concomitant loss of $\beta 3$ and αC from the PF2 domain. The sequence of the binding site remains unchanged between $\beta 2$ and αA in the PF2 domain and $\beta 3$ and αA in the autoinhibitory domain.

Because of this bioinformatic examination of the domain, we have been able to redefine the domain boundaries of the WNK1 kinase as shown in Figure 1c. We have extended the C-terminus of the domain to include what was once postulated to be a coiled-coil domain and moved the N-terminus to abut the C-terminal tail of the kinase domain. In querying this consensus binding site to the remainder of the protein, we discovered another putative autoinhibitory/PF2-like domain which we predict to include residues 864-948.

Using this information, we decided to employ the tertiary structure prediction software, Rosetta *ab initio* to determine whether our domain boundaries were correct and if the domain would have a predicted structure similar to that of the PF2 domain. Using the sequence corresponding to our newly extended boundaries, Rosetta identified a similar $\alpha+\beta$ fold topology in six out of the ten largest clusters of low-energy fragment assemblies. The conserved

peptide-binding site of the WNK1 autoinhibitory domain aligned well with that of the PF2 domain structure. The predicted structure consists of an $\alpha+\beta$ sandwich similar to that of the PF2 domain with 3 antiparallel β strands followed by two adjacent alpha helices. Rosetta predicts a short helical region between strands 2 and 3.

4.2.2 NMR data collection and the solution structure of the WNK1 autoinhibitory domain

The $^1\text{H},^{15}\text{N}$ -HSQC of the WNK1 autoinhibitory domain good dispersion across ^1H and ^{15}N frequencies (Figure 4.2). All asparagine H δ s and arginine/glutamine H ϵ s are stably protonated at pH=6.5, but the domain shows approximately 30% reduction in signal intensity over the course of three weeks at a temperature of 308K. Despite the presence of some signal loss due to precipitation, the domain is amenable to collection of standard triple resonance data for use in the assignment of backbone and sidechain resonances as well as inter-proton distance measurements (see methods).

Following data collection and analysis, 95% coverage of backbone amides present in the $^1\text{H},^{15}\text{N}$ -HSQC spectra was achieved (with the exception of 2 prolines present in the expressed construct not visible in the HSQC). Peaks with overlapping $^1\text{H}/^{15}\text{N}$ -amide resonances were easily resolved through relation to the 3D-HNCO spectra. In total, 93% of all possible backbone $^1\text{H},^{15}\text{N}$ resonances were assigned along with 99% of all possible sidechain assignments.

The structure of the WNK1 autoinhibitory domain is a compact stable monomer with a flexible N-terminal tail associated with linker residues from

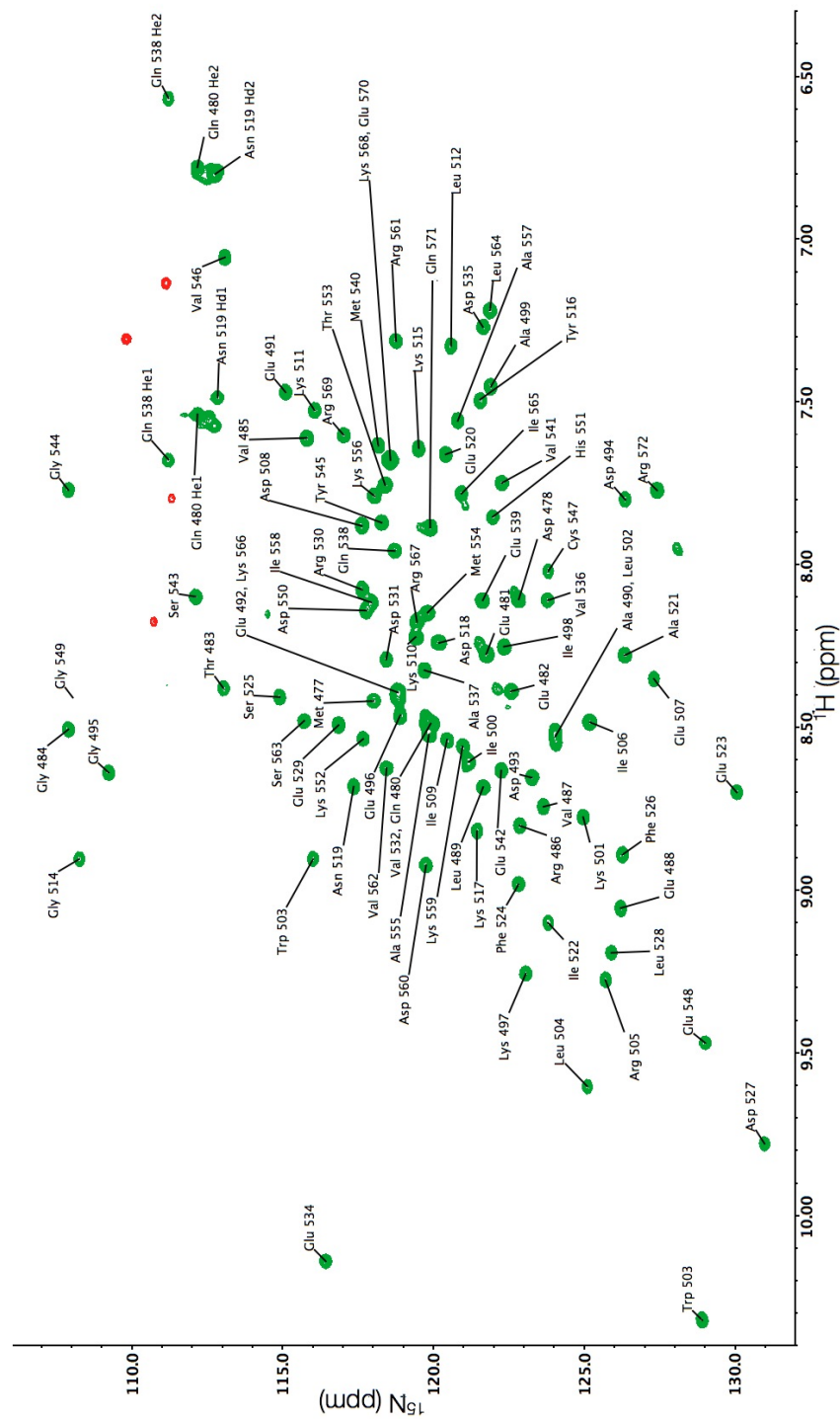


Figure 4.2: ^1H , ^{15}N -HSQC of WNK1 480-572

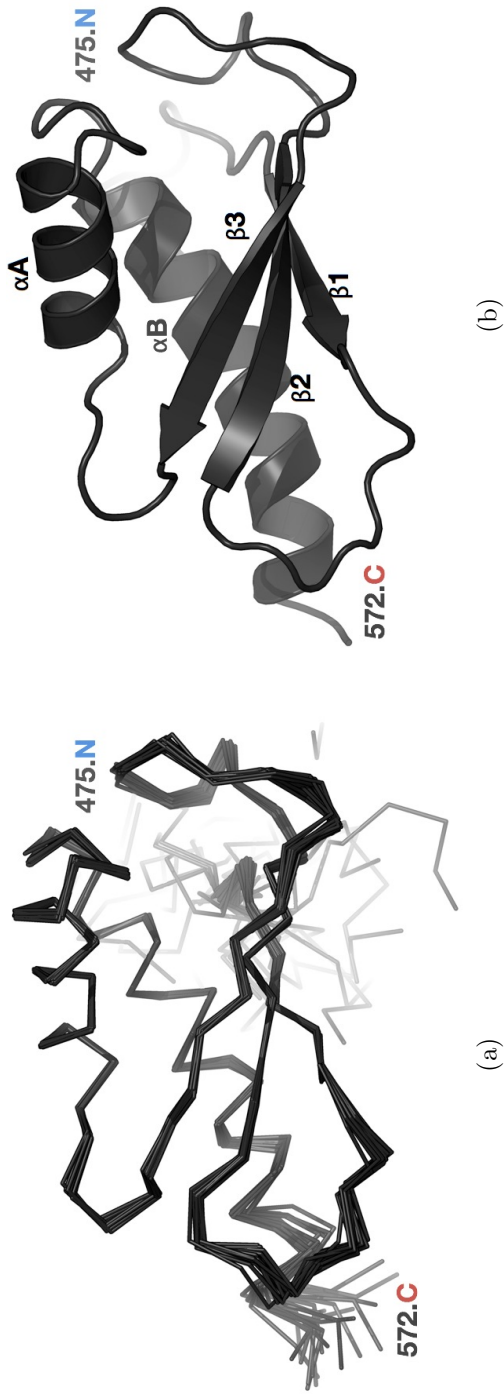


Figure 4.3: a) The solution structure of the WNK1 autoinhibitory domain displayed as an ensemble of the 20 lowest energy structures refined in the presence of water. The fold consists of the same order of secondary structural elements predicted by the JPRED server (Cole et al., 2008) (three beta strands preceding two alpha helices), and the tertiary structure matches very well with the prediction by Rosetta ab initio (Figure 4.9) (Rohl et al., 2004). b) Ribbon diagram of the lowest RMSD structure.

the expression tag. The domain consists of three β strands that form a curved base, packed tightly against two alpha helices. The core of the protein is constructed of entirely hydrophobic residues that are well-packed and capped on both ends of the protein by hydrophilic loops (Table B.1, Figure 4.3).

The structure follows very closely to that predicted by analysis of the primary sequence; and, the binding pocket is well conserved with respect to the OSR-PF2 domain. The first conserved phenylalanine (F524) and the two conserved acidic residues D531/E539 are oriented toward the putative RFXV binding groove between the β 3- α A interface which suggest that the autoinhibitory domain binds the arginine guanidinium group in a similar manner to the OSR-PF2 domain(Figure 4a). The flexible N-terminus containing remnants of the expression tag (475-479) may explain why we observe an elution volume consistent with a globular protein with twice the molecular weight of the autoinhibitory domain when run on a SEC column. However, when we analyzed the uniformly ^{13}C , ^{15}N WNK1-(480-572) using multi-angle laser light scattering (MALLS), we observed an average molecular weight of $11,800 \pm 100$ g/mol compared to a calculated mass of 11,964g/mol (Figure B.1).

In comparison of the WNK1 autoinhibitory domain to that of the OSR1-PF2 domain, the bioinformatic approach to determine the domain boundaries of the autoinhibitory domain were accurate. The approach was able to identify the permutation of the PF2 domain's C-terminal strand to the N-terminus in the autoinhibitory domain and the associated deletion of the penultimate strand and helix. To quantify the structural similarity of the

OSR-PF2 domain and autoinhibitory domains, we structurally aligned the x-ray structure of the PF2 domain with the lowest energy structure from the solution ensemble for the autoinhibitory domain. When all C_α atoms are compared, the RMSD is calculated to be 1.2Å. However, when we align the binding sites from both proteins (AI: 521-543; PF2:449-471) the RMSD for C_α drops to 0.7Å (Figure 4.4). The value of the RMSD in the binding site arises from the positioning of the strand composing the binding site housing F524, and the orientation of the proximal loop. There is little observed deviation in the structure of αA or its trailing loop.

4.2.3 The autoinhibitory domain interaction with RFXV motifs

Given the similarity of the autoinhibitory domain to the PF2 domain, we synthesized a small pentameric peptide with the sequence $\text{NH}_2\text{-GRFKV-NH}_2$. The N-terminal glycine was included to emulate the type of peptide found in the crystal structure of the OSR-PF2 domain. Titration of this peptide into a sample containing $\text{U-}^{13}\text{C},^{15}\text{N}$ -labeled WNK1-(480-572) showed a dramatic displacement in many of the chemical shifts associated with the $^1\text{H},^{15}\text{N}$ -HSQC of the autoinhibitory domain (Figure 4.5). Fast exchange behavior was observed with no obvious peak broadening or intensity loss over the titration range. The observed K_d for binding of the pentamer peptide to the autoinhibitory domain was calculated to be $130 \pm 5\mu\text{M}$. When the change in chemical shifts were plotted according to residue number, the greatest number of affected residues with the largest effects ($\Delta\delta\text{ppm} \geq 0.2$) were observed in

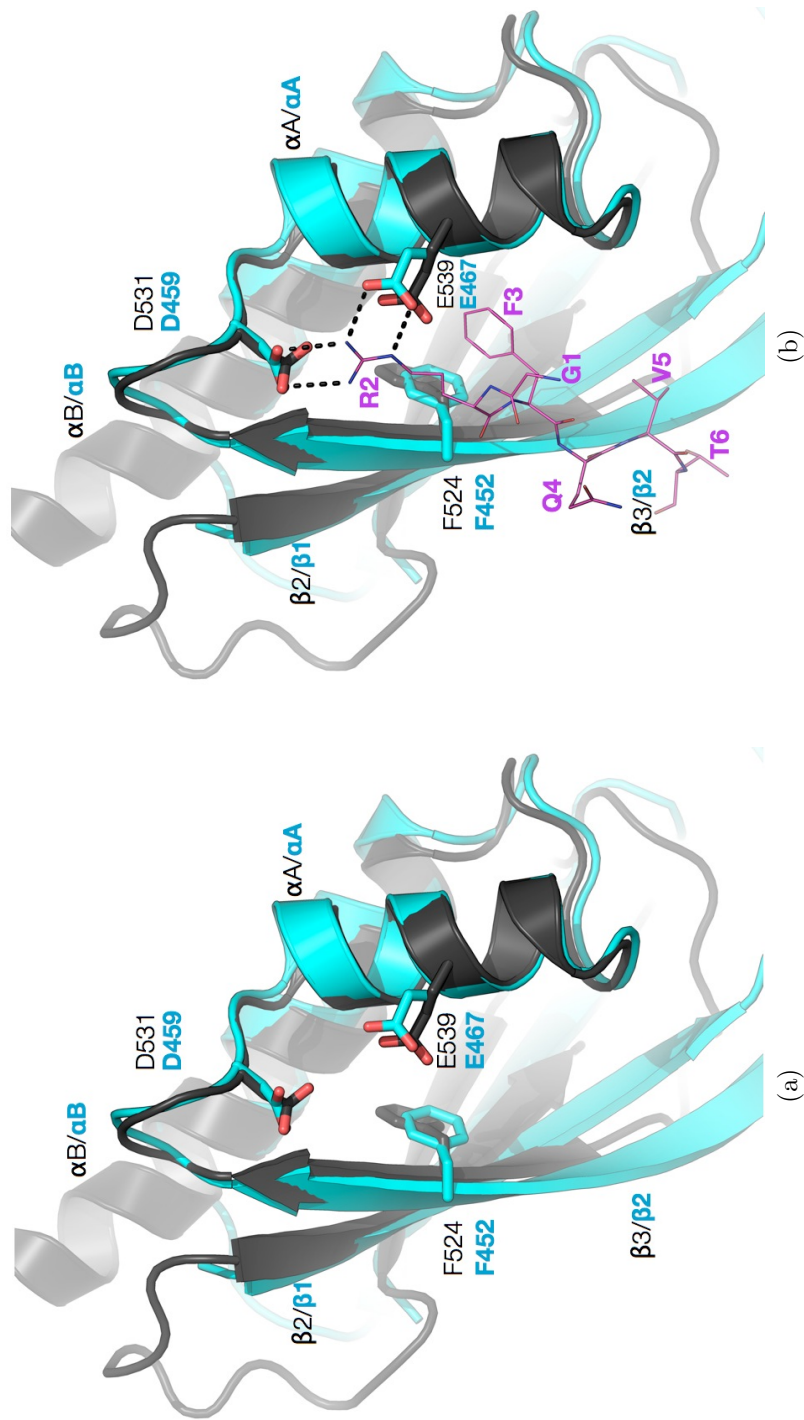


Figure 4.4: a) the conserved RFXV-binding site from the solution structure of the WNK1 autoinhibitory domain (black) aligns well with the site from the OSR-PF2 domain (cyan) solved by Villa et al with an RMSD=0.71 for Ca in the binding site. b) The solution structure of the autoinhibitory domain aligned with the crystal structure of the PF2 domain docked with the GRFQVT peptide (thin lines) derived from the WNK4 kinase (Villa et al, 2007)

the predicted binding site; specifically at strand $\beta 3$ in residues 522-525 as well as a tyrosine in αA (Figure 4.6). Mid-range shifts in chemical shift ($\Delta\delta_{\text{ppm}} \geq 0.1$) were detected in the remainder of αA , the conserved guanidinium-binding D531 as well as $\beta 1/\beta 2$.

To determine whether the association of this RFXV motif has a similar binding mechanism to that of the PF2 domain, we engineered two controls. The first control was used to test binding specificity of the peptide. A pentameric peptide lacking the N-terminal arginine ($\text{NH}_2\text{-GAFKV-NH}_2$) was synthesized and titrated into U- ^{13}C , ^{15}N -labeled WNK1-(480-572) to equimolar equivalence. Collection of the ^1H , ^{15}N -HSQC showed no changes in chemical shifts associated with the autoinhibitory domain (Figure B.2a). Further, an experiment involving the elimination of the arginine recognition glutamate (E539A) was performed. This construct (WNK1-(480-572 E539A) was expressed with U- ^{15}N -labeling and titrated with GRFKV peptide to equimolar equivalency. In a similar result to that discussed above, we observed no change in the chemical shift in the ^1H , ^{15}N -HSQC spectrum (Figure B.2b).

To further probe specificity toward the WNK1 kinase domain, we synthesized a larger peptide corresponding to a 20-residue fragment of the WNK1 kinase domain which spans residues 307-326. This corresponds to fragments of $\alpha D/E$ and the RFXV-containing loop region between them ($\text{NH}_2\text{-GTLKTYLK (RFKV)MKIKVLRN-NH}_2$). When this larger peptide was titrated into U- ^{13}C , ^{15}N -labeled WNK1-(480-572), we observed a switch to slow exchange behavior and a reduction in the K_d by an order of magnitude to $14 \pm 1 \mu\text{M}$ (Figure

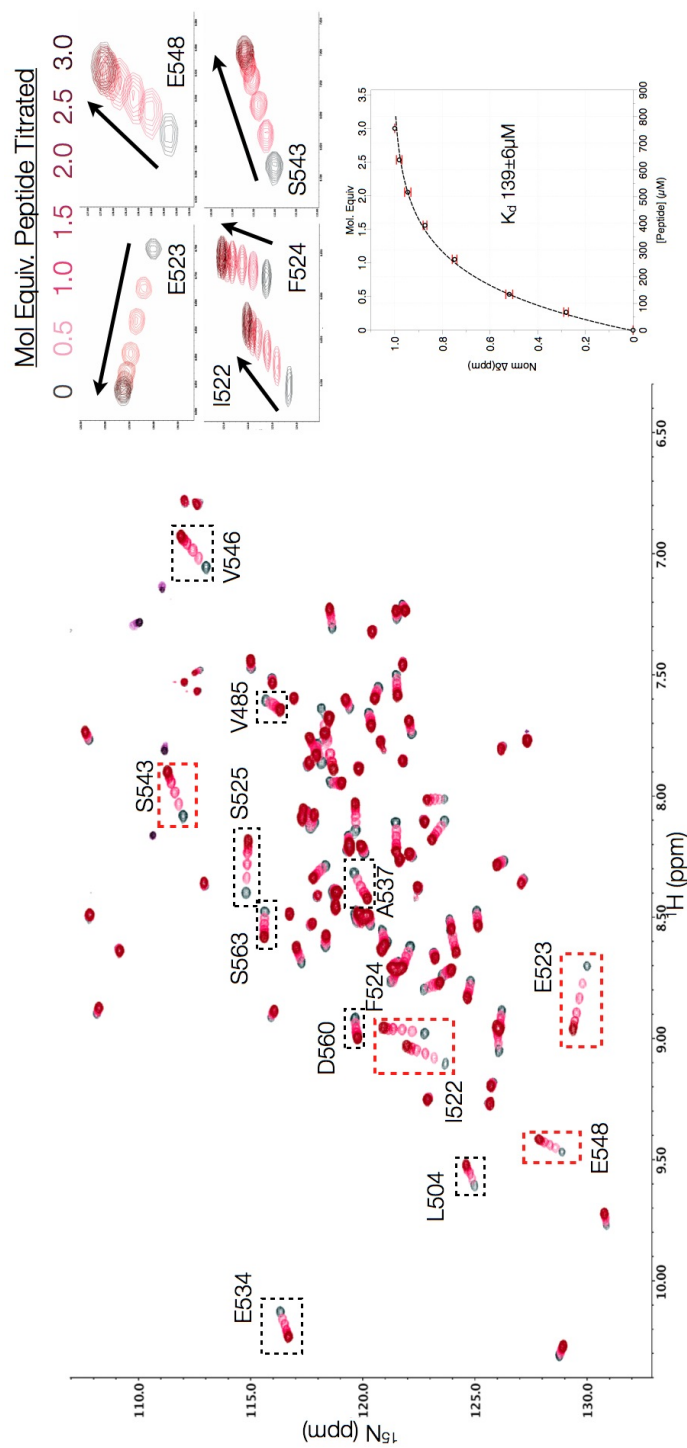
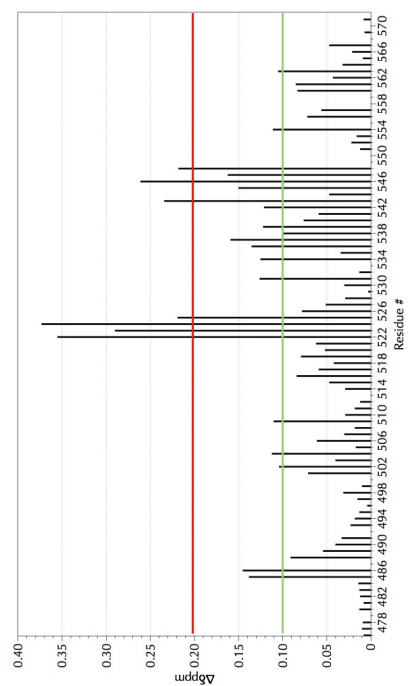
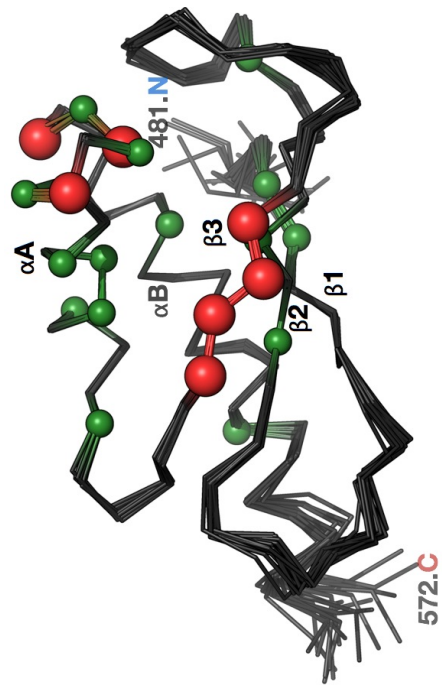


Figure 4.5: ^1H , ^{15}N -HSQC of 270 μM WNK1 480-572 titrated with 10 mM GRFKV peptide in 10 mM NaCl. Fast binding kinetics are observed, and the greatest amount of peak movement is associated with that of the binding pocket of the WNK1 autoinhibitory domain. A set of thirteen amino acids (boxed) and their associated $\Delta\delta$ (ppm) were normalized and averaged to generate a binding isotherm over the associated titration range. An equation for one-site binding was used to fit the data and extract a $K_D = 139 \pm 6 \mu\text{M}$. A sample set of the HSQC peaks used in the titration analysis are shown in the right hand panel with their associated locations on the HSQC shown in red boxes.



(a)



(b)

Figure 4.6: a) Shift in chemical shift as a function of amino acid number is plotted for the spectra of ^1H , ^{15}N -HSQC of WNK1 (480-572) titrated with GRFKV peptide in 10mM NaCl at 35°C. b) the majority of movement is associated with that of the binding pocket of the WNK1 autoinhibitory domain (red $\geq 0.2\text{ppm}$, 0.2ppm \geq green $\geq 0.1\text{ppm}$)

4.7). The titrant binding was tracked by monitoring the rapid loss in signal intensity of the peaks in the binding site. Associated with this significant loss in signal intensity, we observed precipitation of the autoinhibitory domain in the NMR sample tube.

The WNK1 protein kinase possesses an RFXV motif located between alpha helices D and E in the kinase domain and is one of five throughout the kinase, albeit the only one located in the N-terminus, and the only one associated with known secondary structural elements flanking the motif Min et al (2004). To test the possibility of whether the autoinhibitory domain could bind these unstructured RFXV motifs, we synthesized a nonadecameric peptide derived from the RFIV motif in the C-terminus of the kinase (Figure 1c) NH₂-VVHSAGR(RFIV)SPVPESRL-NH₂. The peptide was titrated into U-¹³C,¹⁵N-labeled WNK1-(480-572) and ¹H,¹⁵N-HSQC spectra were collected at each titrant point (Figure 4.8). Upon titration to one molar equivalency, we observed mixed binding kinetics distinguished by some shift in chemical shift associated with signal intensity loss at the midpoint of the titration. We also observed a loss of signal not associated with graded change in chemical shift with the binding site residues F524, E523, I522, situated along β 3. In tracking the change in chemical shift, we were able to fit the data to a one-site binding isotherm with a K_d of $60 \pm 5 \mu\text{M}$.

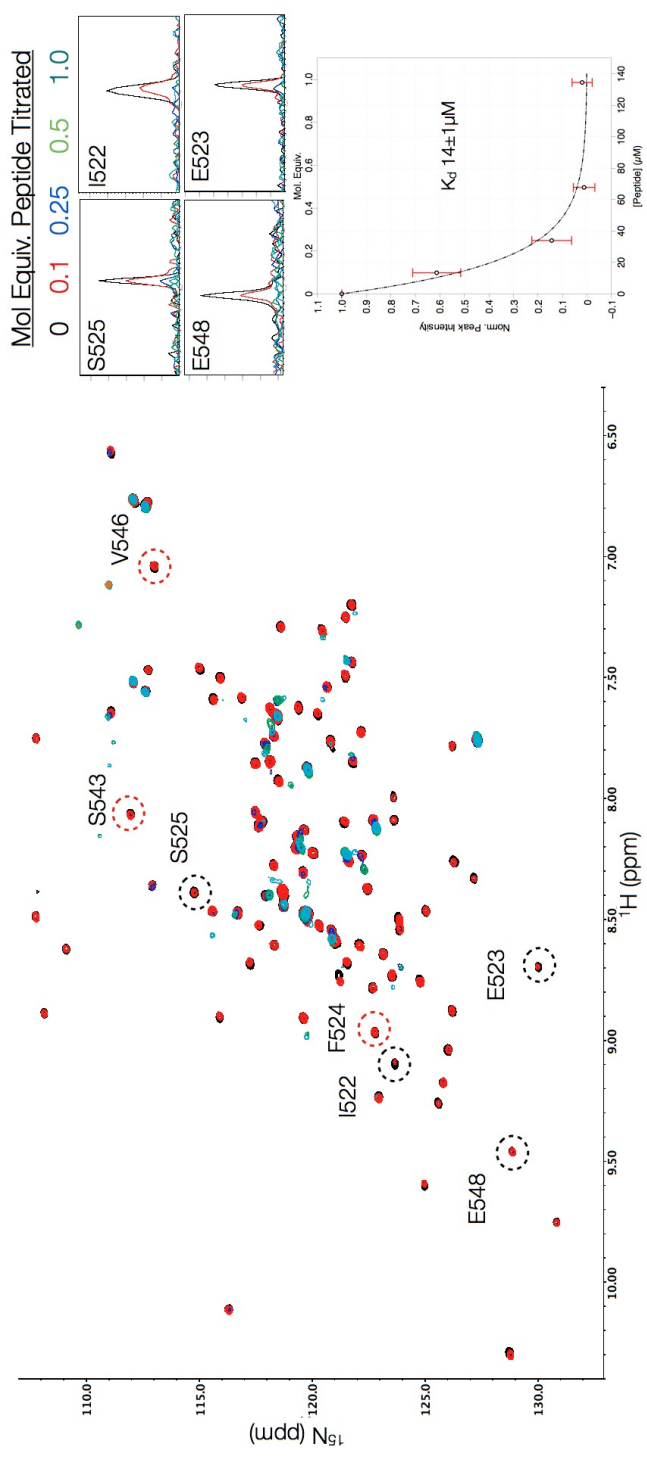


Figure 4.7: ^1H , ^{15}N -HSQC of $135 \mu\text{M}$ WNK1 480-572 titrated with 1mM dodecamer-GRFKV peptide in 10mM NaCl. Slow binding kinetics are observed and are associated with precipitation of the domain as saturation is reached. A set of seven amino acids (circled) and their associated intensities were normalized and averaged to generate a binding isotherm over the associated titration range. An equation for uniform exponential decay was used to fit the data and extract a $K_d = 14 \pm 1 \mu\text{M}$. A sample set of the HSQC peaks used in the titration analysis are shown in the right hand panel with their associated locations on the HSQC shown in red circles.

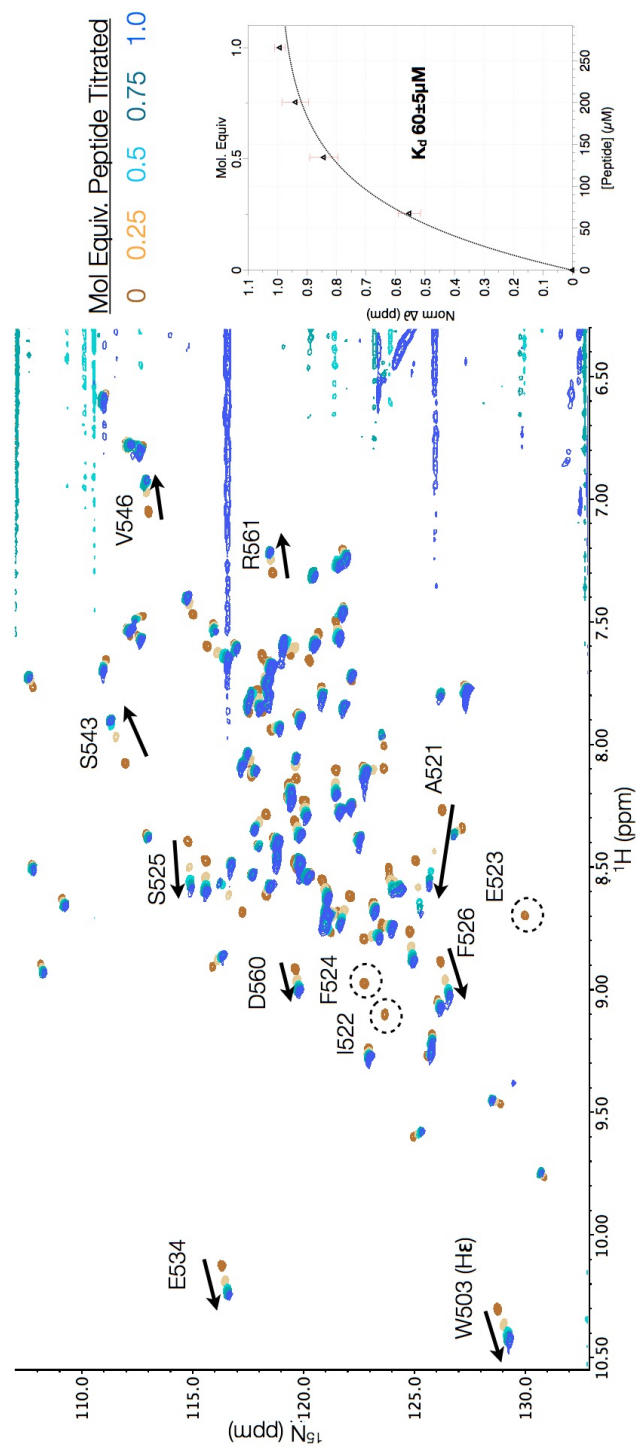


Figure 4.8: ^1H , ^{15}N -HSQC of 272M WNK1 (480-572) titrated with 10 mM nonadecamer-GRFIV peptide in 10 mM NaCl. Intermediate kinetics are observed with a K_d of $60 \pm 5 \mu\text{M}$.

4.3 Discussion

The structure of the WNK1 autoinhibitory domain displays a similar fold to that of the OSR1-PF2 domain. Moreover, the scaffold of the RFXV binding site is completely conserved in tertiary structure and the placement of residues in the binding site. This is reflected in the C α RMSD calculated for this binding cleft. While this measurement is above 1 Å, this can easily be explained by the slight shift in β 3 and the orientation of loop 3 which differs significantly from the PF2 domain to the autoinhibitory domain.

In this examination of the WNK1 regulatory sequence, we have extended the domain boundaries of the segment to abut the C-terminus of the kinase domain and include an α -helix previously predicted as a coiled-coil domain. The extension of the previous domain boundaries from 485-555 to 480-572 to include the aforementioned helix and the primary strand of the domain was essential to generate a stably-folded protein. Based on results the initial bioinformatic search and subsequent sequence analysis, we ran the tertiary structure prediction software Rosetta *ab initio* to determine whether our domain boundaries were correct and if the domain would have a similar predicted structure as that of the PF2 domain. Using the sequence corresponding to our newly extended boundaries, Rosetta identified a similar alpha+beta fold topology in six out of the ten largest clusters of low energy fragment assemblies. The RMSD between the predicted and solution structures is 1.6 Å when the RFXV binding sites are compared. The predicted structure consists of an alpha+beta stack in good agreement with the solution structure, specifically

constructed of 3 antiparallel β strands followed by two adjacent alpha helices. Rosetta predicts a short helical region between strands 2 and 3 which was ultimately deemed inaccurate by our solution structure.

In the sequence and structural comparisons of the autoinhibitory domain with the OSR-PF2 domain, we found a nonhomologous strand permuted to the N-terminus of the WNK1 autoinhibitory domain. In Figure 4.10, the interaction between $\beta 3$ and αB from the PF2 domain is shown. This is compared to that of the $\beta 1/\alpha B$ interaction from the autoinhibitory domain shown in Figure 4.11. In the PF2 domain, there is not a specific interaction between the alpha and beta secondary structure excepting hydrophobic interactions which form the core of the protein (F501,V499/482,I481). This is inconsistent with what is observed in the autoinhibitory domain. In the interface between αB and $\beta 1$, there are two electrostatic interactions which stabilize the contact between the two secondary structural elements. The first hydrogen bond is between $\alpha B/R561$ to $\beta 1/E488$ and the second is between $\beta 1/R486$ to $\alpha B/D560$.

Our negative controls for alanine mutations in both the RFXV peptide and the regulatory domain suggest a similar binding mechanism of the guanidinium group of arginine being electrostatically trapped by the conserved acidic groups in the binding site. Further, chemical shift analysis showing the greatest change in chemical shift along $\beta 3$ may indicate interaction of the FXV amino acids in a manner similar to that observed in the crystal structure of the *holo* form of the PF2 domain Villa et al (2007).

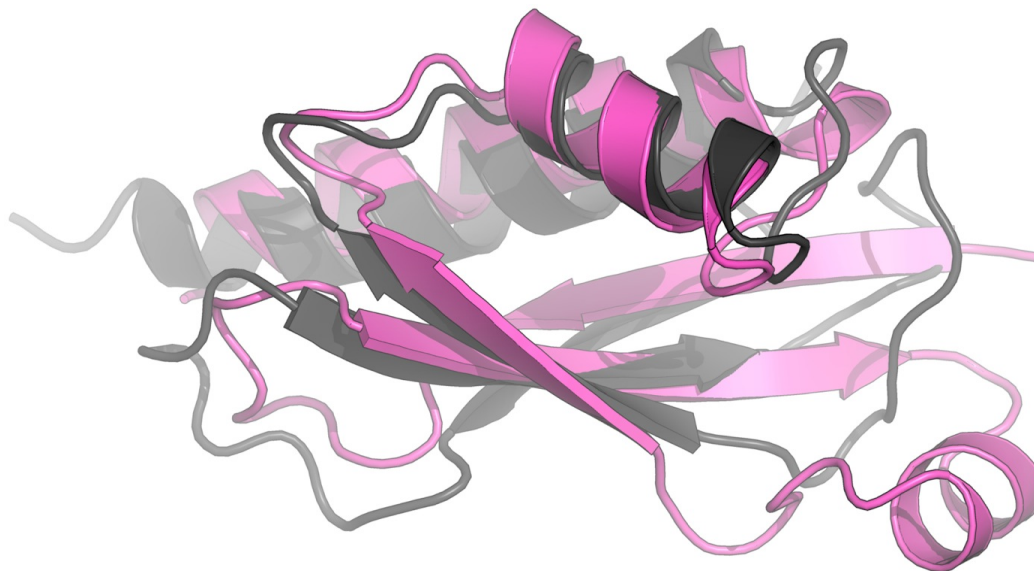


Figure 4.9: The predicted Rosetta structure of the WNK1 autoinhibitory domain (magenta) compared to that of the solution structure of WNK1-480-572 (black).

The interaction of peptide motifs with small regulatory domains are well-characterized in biological systems (Bhattacharyya et al, 2006b). These interacting species have been shown to be essential in the signal transduction machinery where they act in binding the signaling molecule of interest to scaffolding proteins where downstream modules are localized (Tatebayashi et al, 2003; Bhattacharyya et al, 2006a; Nguyen et al, 2002). Alternatively, these domains can act in directly associating two or more proteins using a common localization signal in the absence of scaffolding proteins (Akella et al, 2008; Tanoue et al, 2000). It has been noted that the domains which target the peptide motifs are highly conserved and are less likely to undergo significant evolutionary changes around the binding site whereas the peptide motifs

appear to have more plasticity in terms of sequence surrounding the consensus site (Bhattacharyya et al, 2006b). We propose that these WNK-specific PF2 domains (WSPs) may utilize the latter model adaptable modularity to accomplish multiple roles of autoinhibition, substrate recognition, substrate occlusion or quaternary structure reorganization.

Based upon the measured affinities of the WNK1 autoinhibitory domain to the RFXV motifs derived from the kinase domain and the unstructured C-terminus of WNK1, we hypothesize that WNK1 autoinhibition occurs through the interaction of the autoinhibitory domain with the RFXV motif found between α D and α E found in the kinase domain. Although this interaction is weaker than that observed for the PF2 domain binding to a C-terminal RFXV motif derived from WNK4, we argue that a similar order of affinity is not necessary due to the high local concentration of the autoinhibitory domain relative to the kinase domain of WNK1 Villa et al (2007).

Closer inspection of the proximity of the secondary structural elements separating the domains show that there are only four amino acids linking the terminal alpha helix of the kinase domain to the N-terminus of the autoinhibitory domain. It would appear that this linker would permit limited flexibility of the autoinhibitory domain and constrain conformational variability of the domain to the environment immediately adjacent to the RFXV motif. This would presumably prohibit or allow limited access to that of the active site by substrates. Because of this, we hypothesize that this would promote an *in cis* mechanism of autoinhibition, although interaction *in trans* may still be

possible given the oligomeric state of the protein found *in vivo* Lenertz et al (2005).

The location of the autoinhibitory domain and its proximity to the RFXV motif suggests a multi-layered mechanism of regulation for attenuation of kinase activity. We hypothesize that the large and expanding array of cellular processes that the WNK kinases are involved in requires precise attenuation of kinase activity and not merely the presence of a binary switch.

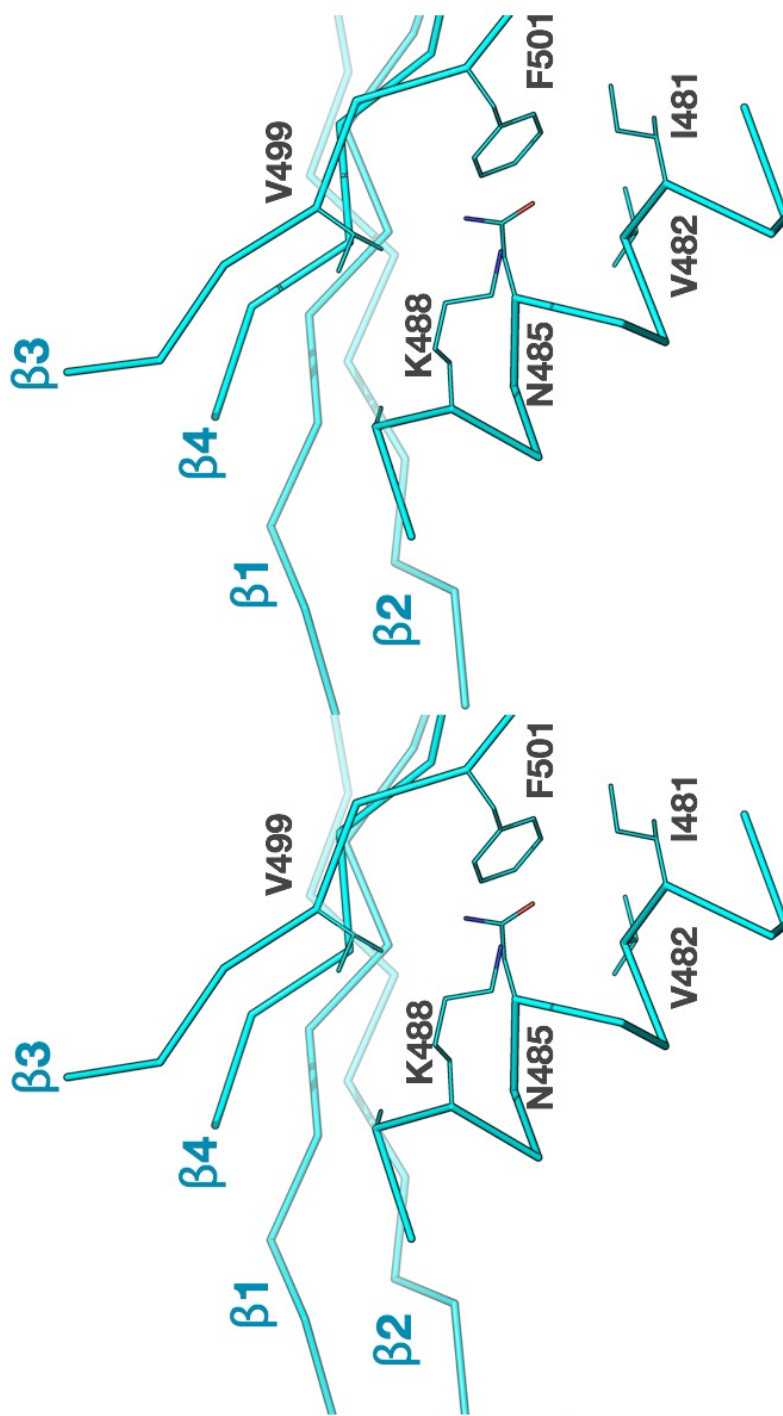


Figure 4.10: Stereo diagram showing $\beta 3/\alpha B$ interaction in the OSR-PF2 domain.

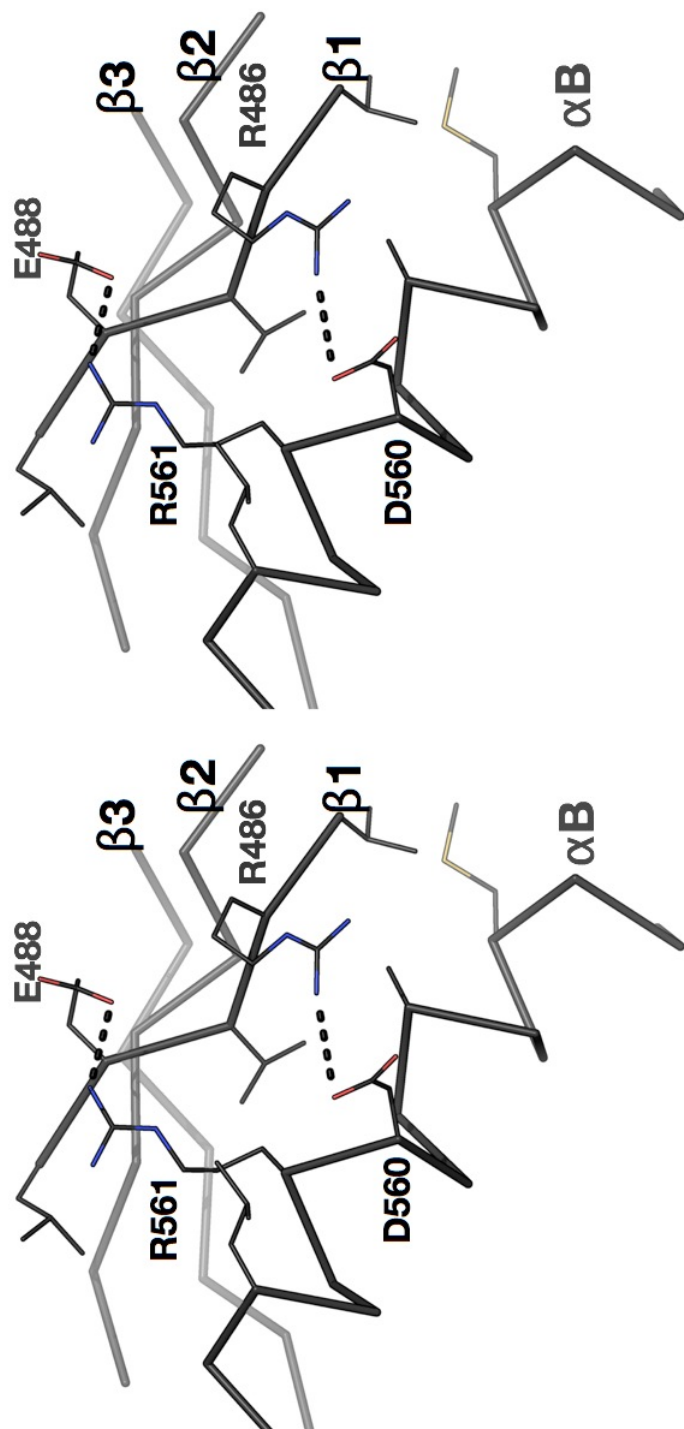


Figure 4.11: Stereo diagram showing β 1/ α B interaction in the WNK1-AI domain

Chapter 5

Expression, Purification and Crystallization of the Active WNK1 Kinase Domain

5.1 Introduction

In conducting an examination of the inactive kinase domain (WNK1 194-483 S382A), while designing a construct that could be amenable for structure determination of the active form of the WNK1 kinase domain, it was noted that both monomers in the asymmetric of the structure reported by Min *et al* unit lacked electron density for the N-terminal residues from 194-209. In addition to this, I noted that X. Min had made a wild-type construct that encompassed residues 209-483 (Table 1.1). Using this information and the knowledge that the wild-type WNK1 kinase domain autophosphorylates to completion (S378* and S382*), expression and purification the truncated kinase was attempted, which, ultimately, resulted in crystals that diffracted to 1.8 Å

5.2 Expression

To express the active, truncated WNK1 kinase, one microliter of pHis-parallel vector encoding the construct was transformed into Rosetta (Novagen)

E. coli, and the cells were plated on agar plates containing LB, ampicillin and chloramphenicol and, and the plates were incubated for 16-18 hours at 37°C. Single colonies were picked, and a 60 mL starter culture containing LB, ampicillin and chloramphenicol was grown 16-20 hours. A total of 5 mL of starter culture was refreshed in identical medium for 1 hour. The refreshed starter culture (10 mL) was used to inoculate 2.4 L Fernbach flasks containing 1 L of LB, ampicillin and chloramphenicol. These larger cultures were grown at 37°C, 220 rpm until the optical density of the media reached 0.85. The culture was induced with a final concentration of 1 mM IPTG and was cooled to 20°C and incubated at 200 rpm for 20 hours to express the protein. Following growth and expression, the cells were pelleted using centrifugation (4000 rpm, 4°C, 35 min) and resuspended in 5 mL/L Ni Buffer A (Table 5.1). The resuspended pellets were flash frozen in N_{2(l)} and stored at -80°C.

5.3 Purification

The pellets containing WNK (209-483) were thawed and incubated with 6 mL of protease inhibitor cocktail (Sigma) before being passed through an Emulsiflex C5 (Avastin) for three iterations to ensure homogeneity and adequate lysis of the sample. The insoluble fraction was separated from the mixture by centrifugation of the sample at 40,000 rpm for 1 hour at 4°C. The supernatant was removed from the samples and passed through a 0.45 μ m filter and then loaded onto a precharged Ni²⁺-sepharose column (GE). Ten column volumes of Ni Buffer A (Table 5.1) were used to wash the column

prior to loading onto an AKTA FPLC (Pharmacia) for a programmed 6-step elution procedure (Figure 5.1) with a final concentration (100%B) of 250 mM imidazole. Fractions containing WNK1 (209-483) were pooled and dialyzed overnight into MonoQ buffer A (Table 5.1). The sample was dialyzed in the absence of TEV protease due to the fact that the presence of the His₆ tag would promote the early elution of the protein due to the increase in positive charge.

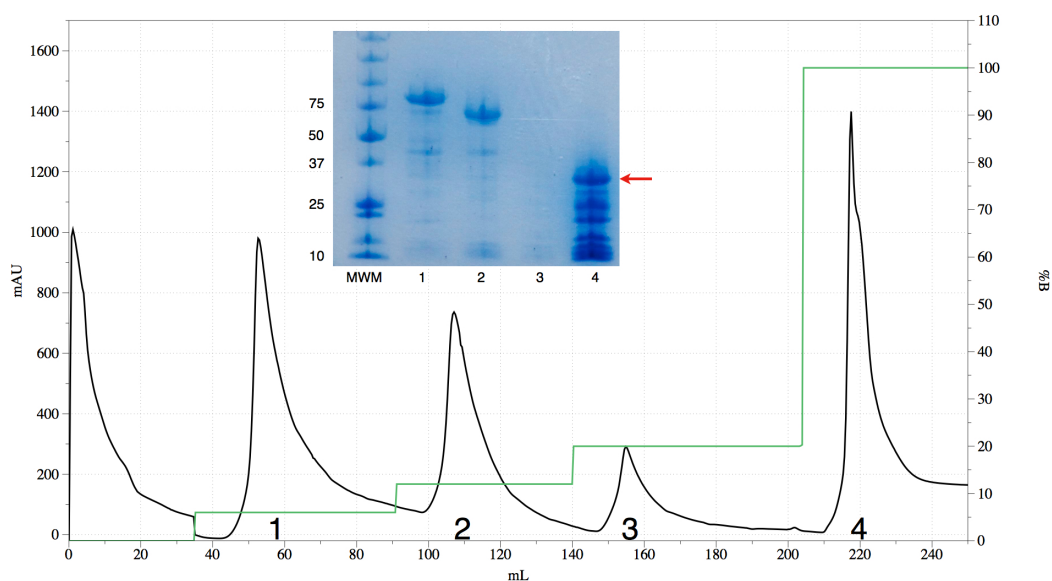


Figure 5.1: Ni²⁺-sepharose of WNK1 (209-483 S378* S382*). Samples numbers designated on the PAGE gel are representative of the peak associated on the chromatogram. The arrow designates the protein of interest on an SDS-PAGE gel.

The dialyzed protein solution was concentrated and loaded onto a MonoQ 5/5 column (GE) and eluted using a program similar to that previously shown in Chapter 2 (Figure 5.2). The fractions containing the protein of interest were pooled and dialyzed into gel filtration buffer (Table 5.1) overnight

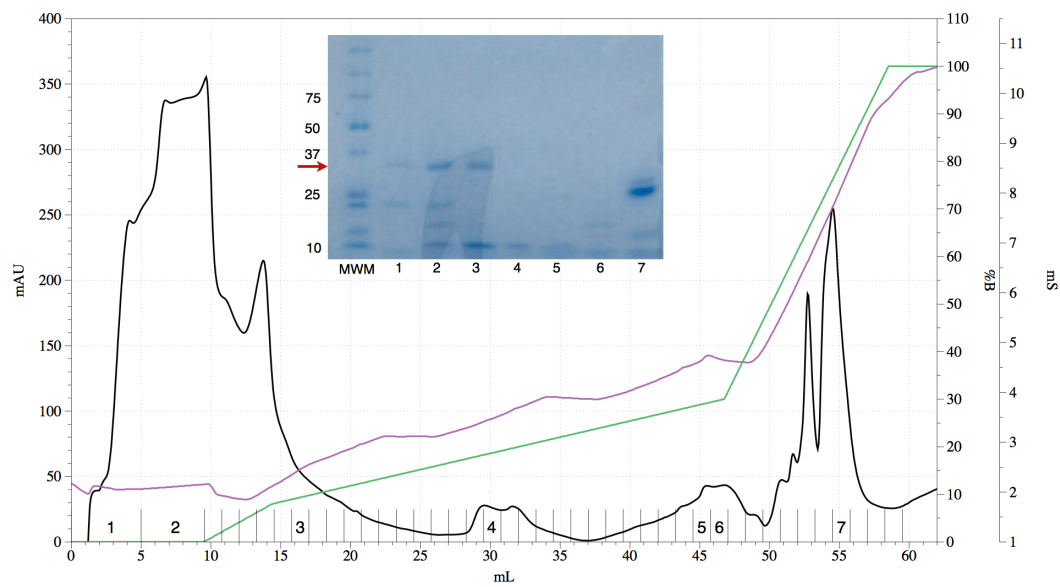


Figure 5.2: MonoQ of WNK1 (209-483 S378* S382*). Sample numbers shown on the PAGE gel are designated in the fractions shown in the chromatogram.

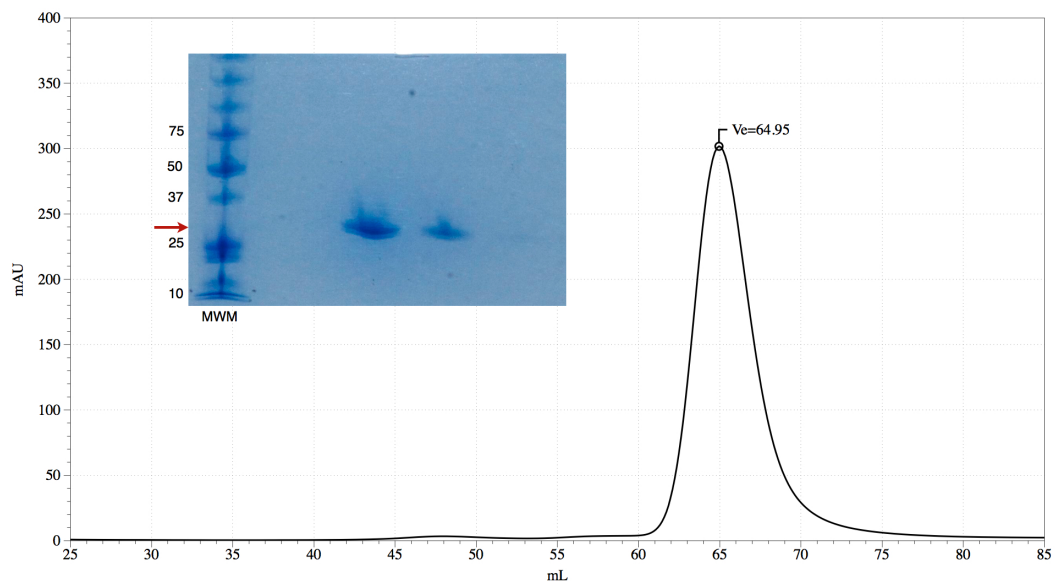


Figure 5.3: Superdex 75 (16/60) of WNK1 (209-483 S378* S382*)

(16-18 hours) in the presence of 1 mg of TEV protease. The dialysis/proteolysis products were applied to a 2 mL Ni²⁺-agarose column and concentrated to be loaded onto a Superdex 75 (16/60) size-exclusion column (GE) that had been equilibrated with Gel Filtration buffer. The protein was eluted isocratically with an elution volume of 65 mL (Figure 5.3). The eluted protein was checked for purity by SDS-PAGE gel and concentrated to 8 mg/mL as assessed by Bradford assay. Aliquots of 50 μ L were divided into 0.5 mL tubes, flash frozen in N_{2(l)}, and stored at -80°C.

5.3.1 Materials

Table 5.1: Buffers for Purification of WNK1 (209-483)

Ni ²⁺ Buffer A	50 mM Tris pH=8.0 300 mM NaCl 20 mM Imidazole
Ni ²⁺ Buffer B	50 mM Tris pH=8.0 300 mM NaCl 250 mM Imidazole
MonoQ Buffer A	50 mM Tris pH=8.0 50 mM NaCl 1 mM EDTA 1 mM DTT
MonoQ Buffer B	50 mM Tris pH=8.0 500 mM NaCl 1 mM EDTA 1 mM DTT
Gel Filtration Buffer	50 mM Hepes pH=8.0 50 mM NaCl 1 mM DTT

5.4 Crystallization of WNK1 (209-483 S378* S378*)

In June of 2011, 300 μ L of WNK1 (209-483) was thawed on ice and centrifuged to degas and remove any precipitate (although none was observed). The Phenix robotic system (Art Robbins) was utilized to set up seven nanodrop trays utilizing one sitting drop well per reservoir. The suites used were as follows: Qiagen Classics, Hampton PEG/Ion, Hampton PEG R, Hampton Salt R, Hampton Index, Qiagen JCSG+ and Qiagen ComPAS. The drops were plated in 1:1 ratios (200 nL+200 nL) at 20°C and stored in a vibration resistant crystallization refrigerator at 16°C.

After one day, the trays were checked and several trays seem to contain pseudo-crystalline material but not large enough to identify defined edges. The trays were placed back in the 16°C incubator for one month. A small crystal with defined edges was identified in July, 2011 in the condition: 0.2 M monobasic potassium phosphate, 20% w/v PEG 3350. An expanded screen to test different molecular weight PEGs was set up according to Table 5.2. The drops were plated in 1 μ L+1 μ L drops on siliconized glass coverslips and suspended in the hanging drop vapor diffusion technique over 200 μ L of well solution.

After incubating for 1 month at 16°C, the trays were checked and a 350 μ m multi-crystal cluster was observed in the well containing 0.2 M KH_2PO_4 and 19% PEG 3350 (Figure 5.4). Smaller crystals were observed in the adjacent well containing 20% PEG 3350, and these crystals were used to microseed into new wells in a dilution series that ranged from no dilution to

1/1000 in increments of an order of magnitude. Following growth of crystals from macroseeding, streak seeding was also attempted using a crystal probe (Hampton) with a higher success rate than microseeding. During this process, although streak seeding was reproducible, macroscopic twinning of the crystals was apparent (Figure 5.4). To resolve this problem, before attempting an additive screen, the amount of monobasic potassium phosphate was varied from 0.1-0.35 M by 0.05 M increments.

It was observed that as the KH_2PO_4 concentration increased, there was remarkable improvement in obtaining single crystals (Figure 5.5). The final optimized crystals were harvested from 0.3-0.35M KH_2PO_4 , 19% PEG 3350 at 16°C after one week of growth. A total of eight crystals were harvested and cryoprotected in 0.35M KH_2PO_4 , 19% PEG 3350, 30% PEG 400 using a μ -droplet setup on the glass coverslip. Briefly, following identification of ideal crystals for data collection, a 1 μ L droplet of cryoprotectant was incubated with an equal quantity of precipitant solution on the exposed coverslip containing the droplet with the crystals to be harvested. This is conducted in a humid environment to prevent droplet evaporation. A 2 μ L droplet is placed adjacent to the precipitant/cryoprotectant mixture to reduce the time crystals are exposed to the atmosphere. Crystals were transferred stepwise from the 50% cryoprotectant solution to the 100% solution with incubation times ranging from 5-15 seconds. Following cryoprotection, samples mounted on robotic pins were plunged into 800mL of $\text{N}_2(l)$ and capped.

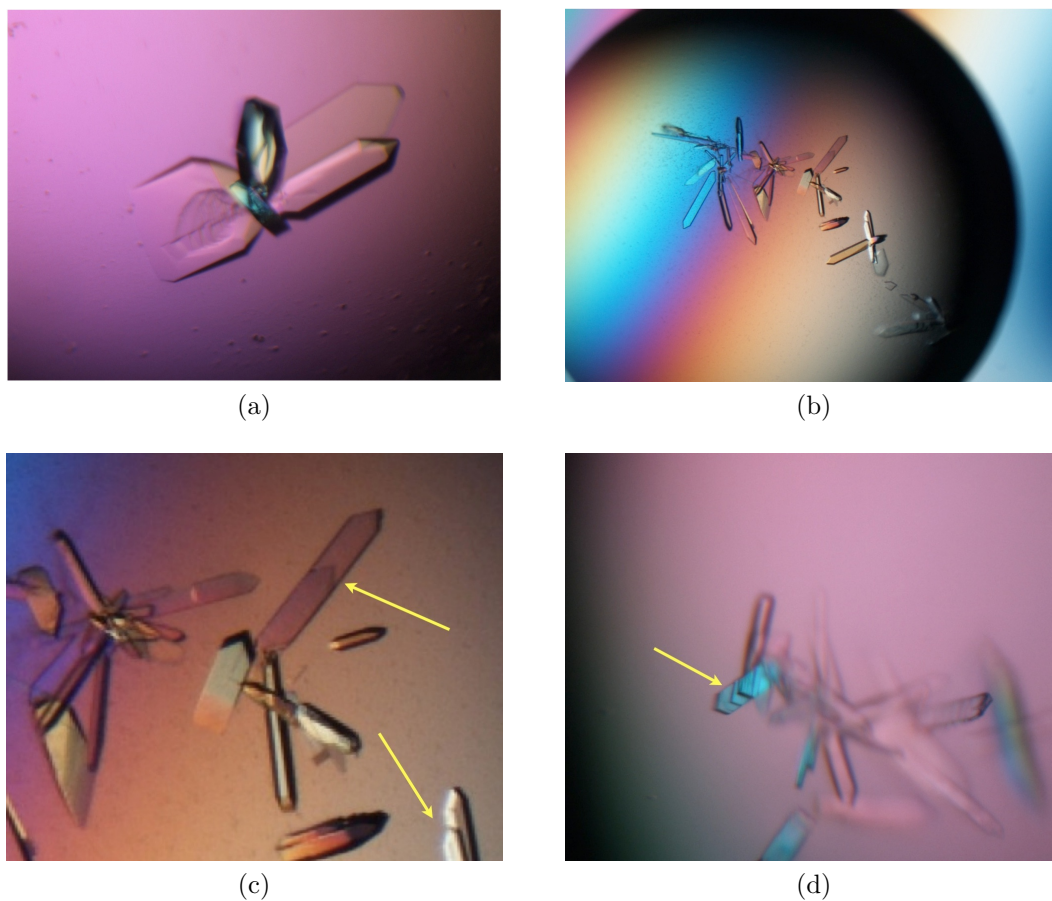


Figure 5.4: Initial crystallization of WNK1 (209-483 S378* S382*) a) Initial crystals obtained in 0.2M KH_2PO_4 , 19% PEG3350. b) crystals obtained after streak seeding c),d) arrows indicate presence of macroscopic twinning observed in low concentrations of KH_2PO_4



Figure 5.5: Crystallization of WNK1 (209-483 S378* S382*) in increasing KH_2PO_4
a) 0.1M b) 0.15M c) 0.2M d) 0.25M e) 0.3M f) 0.35M

Table 5.2: WNK1 (209-483) PEG Screen

		[PEG](% v/v) [†]					
		18%	19%	20%	21%	22%	23%
	1.5M KH ₂ PO ₄	130 μ L	130 μ L	130 μ L	130 μ L	130 μ L	130 μ L
PEG 2000	50% v/v PEG	360 μ L	380 μ L	400 μ L	420 μ L	440 μ L	460 μ L
	H ₂ O	510 μ L	490 μ L	470 μ L	450 μ L	430 μ L	410 μ L
	Total Vol.	1 mL	1 mL	1 mL	1 mL	1 mL	1 mL
PEG 3350		"	"	"	"	"	"
PEG 4000		"	"	"	"	"	"
PEG 5000		"	"	"	"	"	"
PEG 8000		"	"	"	"	"	"

[†]All wells contain 0.2M KH₂PO₄

Chapter 6

Structure Determination and Analysis of the Activated WNK1 Kinase Domain

6.1 Theory

6.1.1 Diffraction by crystalline substances

When light interacts with matter, two processes can occur. The light can be absorbed by the material or scattered. In X-ray diffraction by a crystal, elastic scattering is considered. For a single atom in a vacuum, the scattering can be described by:

$$f_n = 2\rho(r)\cos(2\pi r\mathbf{S})dv_r \quad (6.1)$$

where $\rho(r)$ is the centrosymmetric distribution of electrons about the nucleus, the volume of which is dv_r . \mathbf{S} is the scattering vector or the difference between the incident vector and the scattered vector. When a collection of atoms are arranged in a crystal with a unit cell of volume $(a \times b \times c)$, the structure factor of all atoms in the unit cell can be expressed as

$$F(S) = \sum_{j=1}^n f_j e^{2\pi i r_j \mathbf{S}} \quad (6.2)$$

where r_j is the number of atoms from $j = 1$ to $j = n$. \mathbf{S} now has the value

$$|\mathbf{S}| = \frac{2d\sin\theta}{\lambda} \quad (6.3)$$

d is the distance between the scattering planes, θ is the scattering angle and λ is the wavelength of light probing the crystal, assuming n number of atoms contributing to the sum of all atomic scattering factors f_j . Further, the structure factor for the individual unit cell can be expanded into separate vectors for the unit cell dimensions (a,b,c). The scattering for n unit cells in a crystal can be expressed as a summation of the individual unit cells.

$$W(S) = F(S) \times \sum_{t=0}^{n_1} e^{2\pi i t a \mathbf{S}} \times \sum_{u=0}^{n_2} e^{2\pi i u b \mathbf{S}} \times \sum_{v=0}^{n_3} e^{2\pi i v c \mathbf{S}} \quad (6.4)$$

The components $a\mathbf{S}$, $b\mathbf{S}$, $c\mathbf{S}$ arise from the addition of the scattering vectors and are known as the Laue conditions such that

$$\begin{aligned} a\mathbf{S} &= h \\ b\mathbf{S} &= k \\ c\mathbf{S} &= l \end{aligned} \quad (6.5)$$

where h, k, l are integer values. Since the vector \mathbf{S} is perpendicular to the reflecting plane, it becomes difficult to see how the Laue conditions for coherent diffraction are satisfied by being integer values. Mathematically, we can satisfy this by creating an orthonormal set of axes called the reciprocal lattice such that

$$a_i * a_j^* = \delta_{ij} \begin{cases} i = j & 1 \\ i \neq j & 0 \end{cases} \quad (6.6)$$

The orthonormality of the set of axes a^* , b^* , c^* is important because a^* has the property that it is parallel to the bc plane represented by $(h = 1, k = 0, l = 0)$. Accordingly, b^* is represented as $h = 0, k = 1, l = 0$ and c^* is $h = 0, k = 0, l = 1$. Since \mathbf{S} is a function of hkl , it can be split into vectors along the reciprocal

lattice lines.

$$a\mathbf{S} = aa^* + ab^* + ac^* \quad (6.7)$$

$$h = 1 \quad 0 \quad 0$$

It follows that application of b^* and c^* in a similar fashion will produce the lattice points hkl in reciprocal space. If the Laue conditions are satisfied, diffraction coherence in the unit cell of the crystal will coincide with a point in the reciprocal lattice.

6.1.2 The phase problem

Over the entire unit cell, the structure factor can be thought of as a area measurement of the electron density along continuous vectors

$$F_{hkl} = V \iiint_{x,y,z=0}^1 \rho(xyz) e^{2\pi i(hx+ky+lz)} dx dy dz \quad (6.8)$$

which is the Fourier transform of electron density. The inverse Fourier transform from structure factor amplitude can be represented

$$\rho(xyz) = \frac{1}{V} \sum_h \sum_k \sum_l |F(hkl)| e^{-2\pi i(hx+ky+lz) + i\alpha(hkl)} \quad (6.9)$$

where $i\alpha(hkl)$ is the phase information. During data collection, the structure factor amplitudes are available from the measured peak intensities but the phase information is not. Thus giving rise to the well-known "phase problem."

6.2 Data Collection

Crystals of WNK1 209-483 S378* S382* were shipped to the Advanced Photon Source at Argonne National Laboratory in Argonne, IL and data were

collected at the 19-ID beamline, using remote data collection. The use of an ACTOR robotic arm to manipulate crystal mounting and dismounting from the goniometer was employed. A total of eight crystals were shipped to be tested and two of the crystals yielded diffraction of 1.9 Å or better where the signal to noise (I/σ_I) was greater than 2 in the final resolution bin. For the crystal that was used to determine the structure of the activated WNK1 kinase domain, 180° of data was collected with an oscillation range of 1° using a wavelength of 0.97915 Å. Two seconds of diffraction data were collected per image with an attenuation of 9.38 and the detector set at a distance of 219.82 mm (6.1). The data were integrated and scaled in the $P 1 2_1 1$ space group using Denzo and Scalepack integrated in the HKL2000 software package (Otwinowski and Minor, 1997), the data from which can be seen in Figure 6.2. The space group of $P 1 2_1 1$ was chosen due to the observation of systematic absences along $0k0$ in the reciprocal lattice. Upon inspection of the diffraction pattern, the data appeared to be anisotropic. To analyze this possibility, the diffraction anisotropy server was utilized to analyze the MTZ file following integration and scaling by HKL2000 (Strong et al, 2006). The server detected slight anisotropy and scaled the dataset via ellipsoidal truncation. The resultant MTZ file (output_2_danisotrop.mtz) was used for molecular replacement.

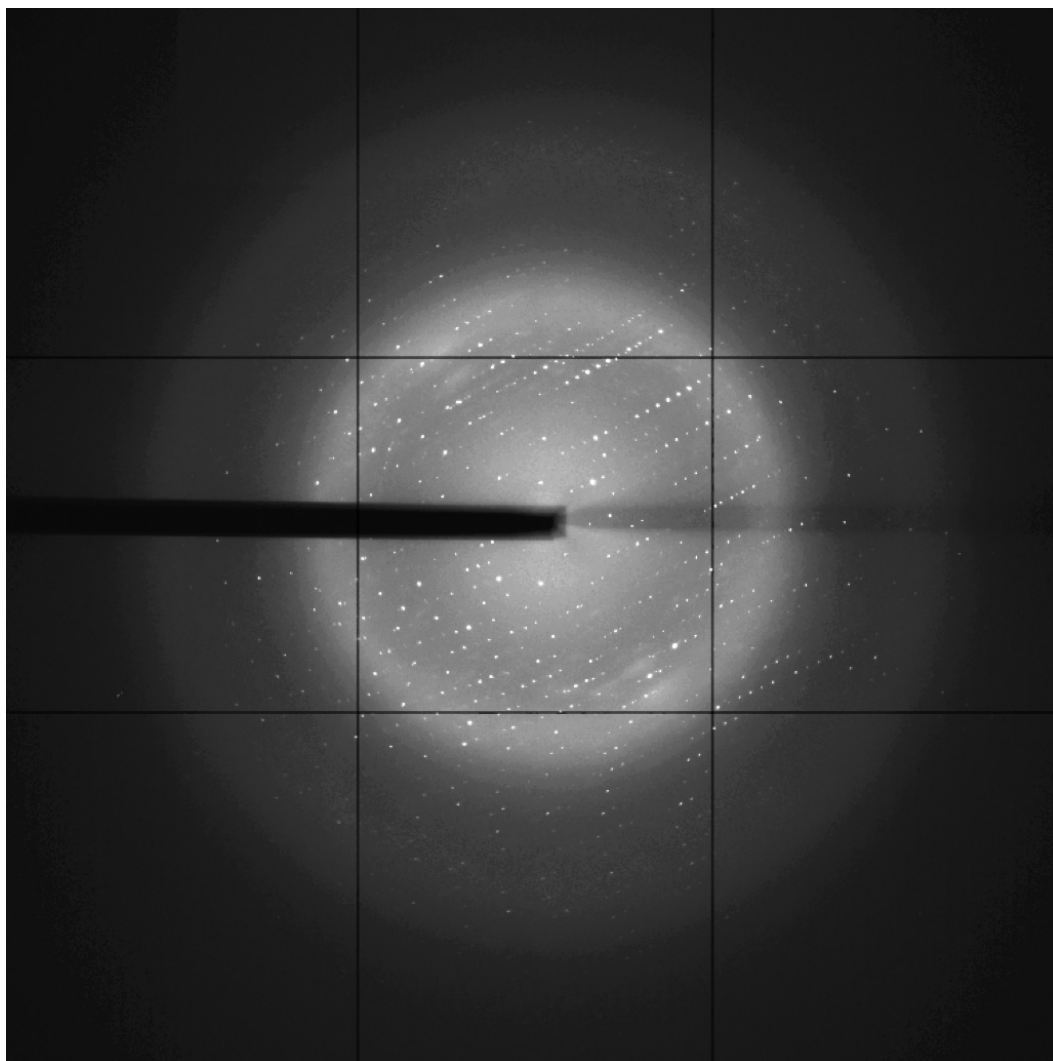


Figure 6.1: Diffraction Pattern of WNK1 (209-483 S378* S382*). The reflections extend to 1.6 Å although the $I/\sigma(I)$ at this resolution is low. The data was integrated and scaled at a resolution limit of 1.83 Å

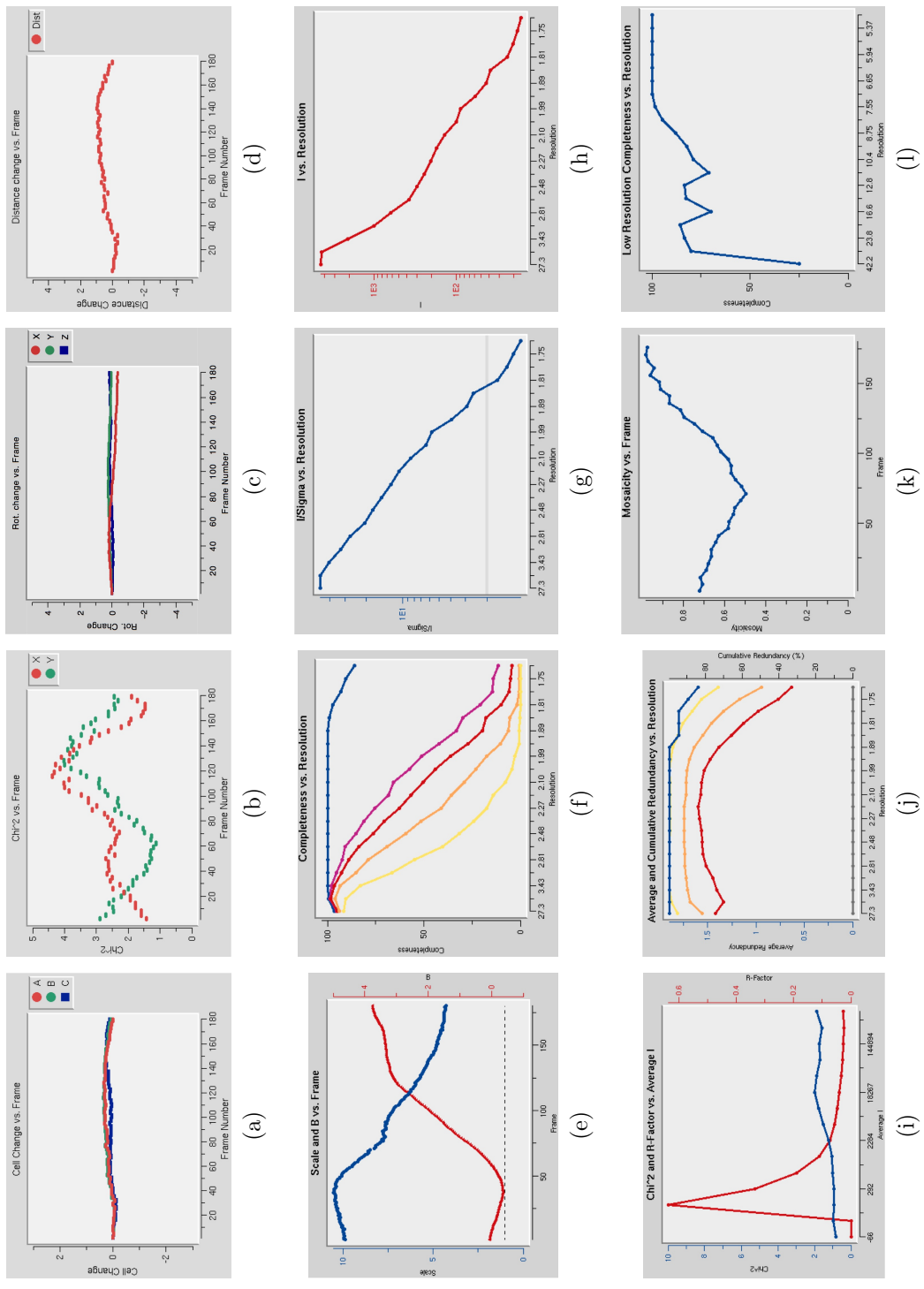


Figure 6.2: Statistical graphs from scaling and integration of data collected on WNK1 (209-483 S378* S382*) using the HKL2000 program (Otwinski and Minor, 1997)

6.2.1 Map Calculation

To solve the phase problem pertaining to the dataset collected for the activated WNK1 kinase (209-483 S378* S382*), molecular replacement was utilized. Currently, for macromolecular crystallography, there are only five solutions to the phase problem. Four of these solutions involve experimentally determined phases using single or multiple isomorphous replacement with heavy atoms paired with single or multi-wavelength measurements. Because the sequence of the inactive WNK1 kinase domain is over 99% identical to the activated kinase domain, molecular replacement is considered to be a viable option. (In general, any model with over 30% sequence identity to the target can be considered as a candidate for molecular replacement (MR) (Rupp, 2009)).

The MR solution to the phase problem uses a combination of rotation and translation functions to find the maximum likelihood coefficient by comparing the Patterson maps of the native data set and the search model. The Patterson function is the product of a convolution of the electron density at a specific point in the unit cell over the entire unit cell. More simply, if two atoms are separated by a vector \mathbf{u} , the distance between those atoms will be related by a centrosymmetric peak about the axis points of the unit cell according to

$$\begin{aligned} P(\mathbf{u}) &= \int \rho(\mathbf{r}) \times \rho(\mathbf{r} + \mathbf{u}) dv \\ &= \frac{1}{V} \sum_{\mathbf{S}} |F(\mathbf{S})|^2 e^{2\pi i \mathbf{u} \cdot \mathbf{S}} \end{aligned} \tag{6.10}$$

It is important to note that the Patterson map is generated *only* as a function of the structure factors and *does not* require phase information.

To begin the molecular replacement procedure, the previously determined structure of WNK1 194-483 S382A was modified by CHAINSAW in the CCP4 suite to mutate S382A back to a serine. Also, the lobes of the kinase domain were divided into N and C-terminal fragments to be used as search models simultaneously in the MR process (Stein, 2008; Collaborative Computational Project, 1994). The two lobes consisted of the residues 210-305 (N) and 306-480 (C). The PHENIX v.1.7.2 software suite's implementation of Phaser was used to carry out the molecular replacement (Adams et al, 2010; McCoy et al, 2007). The fast rotation and translation functions were used to align the Pattersons of the search model and native dataset (Crowther and Blow, 1967; Crowther, 1972). Following molecular replacement, the log likelihood gain indicated a strong solution with a value of 952.5.

6.2.2 Model Building and Refinement

Following molecular replacement, autobuild was used to generate the initial model of the protein using the initial electron-density map generated by PHENIX. Initially, the program built some of the protein model into areas that lacked electron density, which included the area where the activation loop is expected. To improve the model, the amino acids for areas lacking electron density were removed by modification in the software program COOT (Emsley et al, 2010) and the resulting model was refined using simulated annealing.

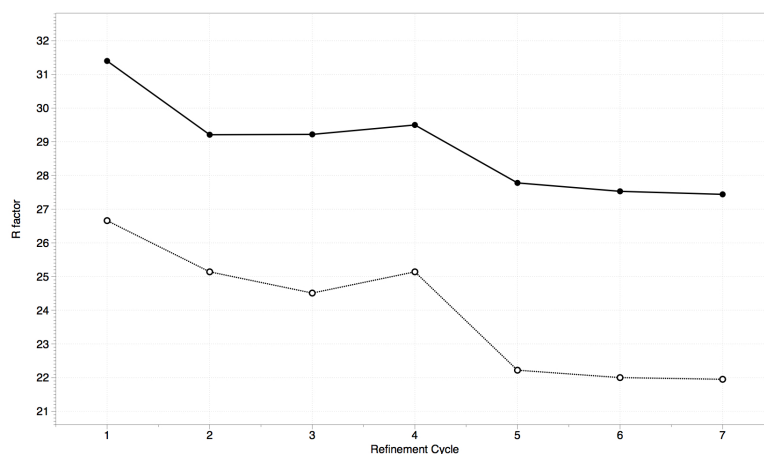


Figure 6.3: Refinement plot for WNK1 (209-483 S378* S382*)

This model building process continued for a total of seven rounds of refinement which eventually included the use of TLS (translation, libration, screw) refinement utilizing both the built-in PHENIX/TLS server and the independent web-based server if PHENIX failed to generate an adequate number of TLS groups (Painter and Merritt, 2006b,a). The R_{work} and R_{free} values as a function of the refinement step number can be seen in Figure 6.3. Following refinement, the statistics for the model of the activated WNK1 kinase are presented in 6.1.

6.3 Structure of the activated WNK1 kinase domain

6.3.1 General topology

The structure of the activated WNK1 kinase domain is composed of a dual-domain architecture that is common to all protein kinases. The N-

Table 6.1: Data collection and Refinement Statistics for WNK1 (209-483)

Space Group	P 1 2 ₁ 1
Unit Cell	a=44.74 Å, b=64.23 Å, c=42.08 Å $\alpha=90^\circ, \beta=92^\circ, \gamma=90^\circ$
Resolution (Å)	35.1-1.83 (1.86-1.83)
Observed Reflections	75,996
Unique Reflections	19,748
Completeness	99.6 (98.8)
I/ σ_I	30.8 (2.6)
Redundancy	3.7 (3.4)
R _{work} (%) [‡]	21.9
R _{free} (%)	27.4
Number of groups	
Protein Atoms	2050
Water	149
RMSD	
Bond Length, Å	0.008
Bond Angle, °	1.12
Average B factor, Å ²	37.2
Ramachandran Map (%)	
Favorable	97.4
Allowed	2.6
Disallowed	0

[†] Values in Parentheses indicate the highest resolution shell

[‡] R_{work} = $\sum ||F_{obs} - |F_{calc}|| / \sum |F_{obs}|$, where F_{obs} and F_{calc} are the observed and calculated structure factors, respectively.

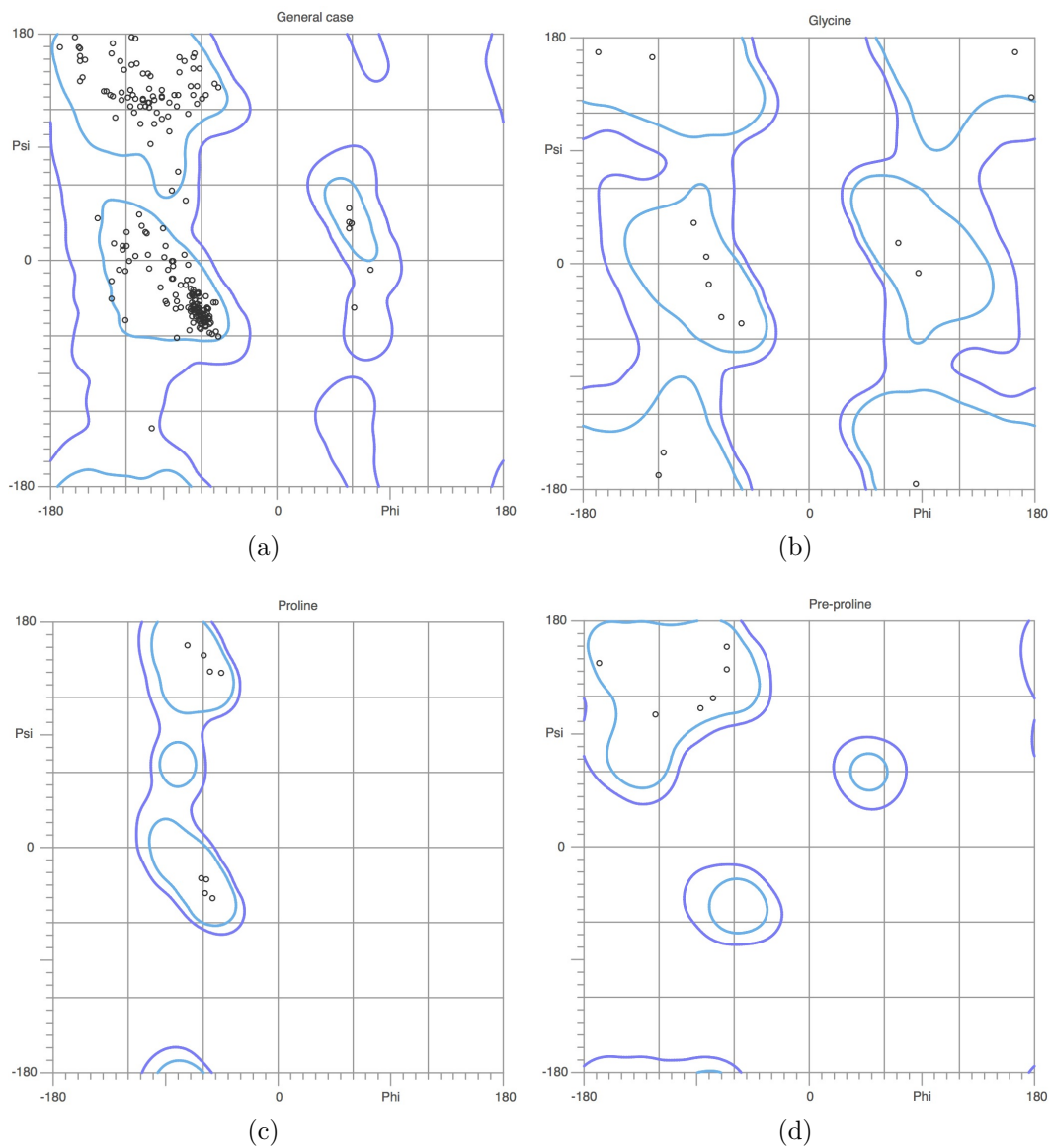


Figure 6.4: Ramachandran map for WNK1 (209-483 S378*, S382*) as determined by MOLPROBITY (Chen et al, 2010). Phi/Psi plots are shown for a) general amino-acid residues b) glycine c) proline and d) residues preceding prolines

terminal lobe is constituted by a near-complete β -barrel, which is made of seven antiparallel β strands, while the C-terminus contains all α -helices. In the structures of protein kinases, the activation loop is usually found bridging the two lobes; however, in the structure of the activated WNK1 kinase domain, the loop is disordered. The disordering of the activation loop is found in some activated (phosphorylated) kinase domain structures (Rothweiler et al, 2011; Xie et al, 1998) and is usually correlated with movement of α C toward the ATP site to allow access of the glutamate (E268) to stabilize the catalytic lysine during the phospho-transfer reaction. However, the activation loop is not the only loop that is disordered in the protein. There are a total of six disordered regions in the protein encompassing residues (231-232, 255-263, 290-294, 373-386, 396-397, 428). This includes the glycine-rich loop adjacent to the catalytic lysine, the activation loop, and the majority of the N-terminal portion of α C and its preceding loop emanating from β 4 (Figure 6.5).

As observed by biochemical studies (Chapter 7), the WNK1 kinase domain appears to be highly dynamic in the presence of low salt concentrations, as indicated by the midpoint melting temperature (T_m) provided by the analysis of differential scanning fluorimetry data. When salt is titrated into the protein sample, the midpoint melting temperature increases. Paired with this observation, is the fact that the activity of the kinase toward the generic kinase substrate MBP decreases as salt is added to the reaction buffer. This corresponds to an IC_{50} of 130mM for NaCl inhibition of WNK1.

The activated structure of the WNK1 kinase domain was crystallized

in the presence of 25 mM NaCl which would indicate that the kinase should be active and dynamic. The lack of observed electron density for the catalytic loop, α C, and many of the loops that are located in the front portion of the kinase domain can possibly be accounted for in the lack of crystal contacts in this region. As shown in Figure 6.6, there are extensive packing interactions present on the back side of both the N and C lobes. These packing contacts continue along the bottom of the C-terminal lobe in interactions involving the N-terminal lobe of the adjacent unit cell. Despite these tight packing interactions between unit cells in the majority of the space, there is a specific lack of contact between the front of the protein kinase, where the activation loop is located, involving symmetry-related molecules. These crystallization conditions an adjunct to the fact that the structure of the mutant, inactive form of the WNK1 kinase domain was solved in conditions of 300 mM NaCl.

As mentioned in the preceding chapter on the crystallization of the activated WNK1 kinase, increasing the dibasic potassium phosphate concentration from 0.1 M to 0.35 M in the presence of streak seeding greatly improved the formation of single crystals. In the crystal structure, a possible mechanism for the improvement of the crystals is found in the binding of a single phosphate molecule between alpha helices E and I in the C-terminus of the kinase domain. As seen in Figure 6.7, the phosphate interacts with three water molecules that, in turn, interact with Q336. The binding of the phosphate is stabilized by hydrophilic interactions to the imidazole group of H339 and to the backbone amide of I470. A similar interaction between a sulfate molecule siting between

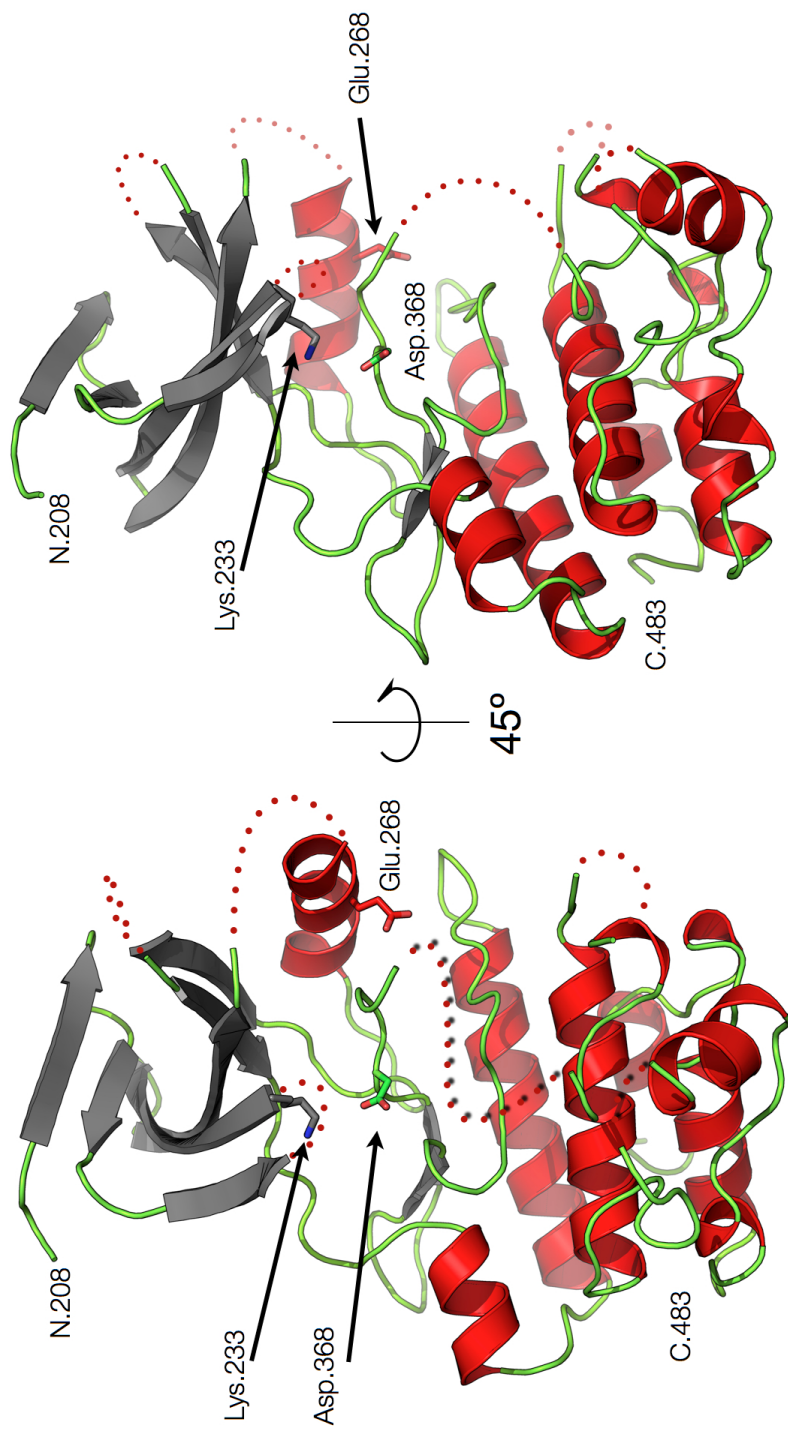


Figure 6.5: Crystal structure of the activated WNK1 kinase domain. α helices are colored in red, β strands grey and loops in green. Missing regions (loops and α C) are designated with red dots connecting the two termini.

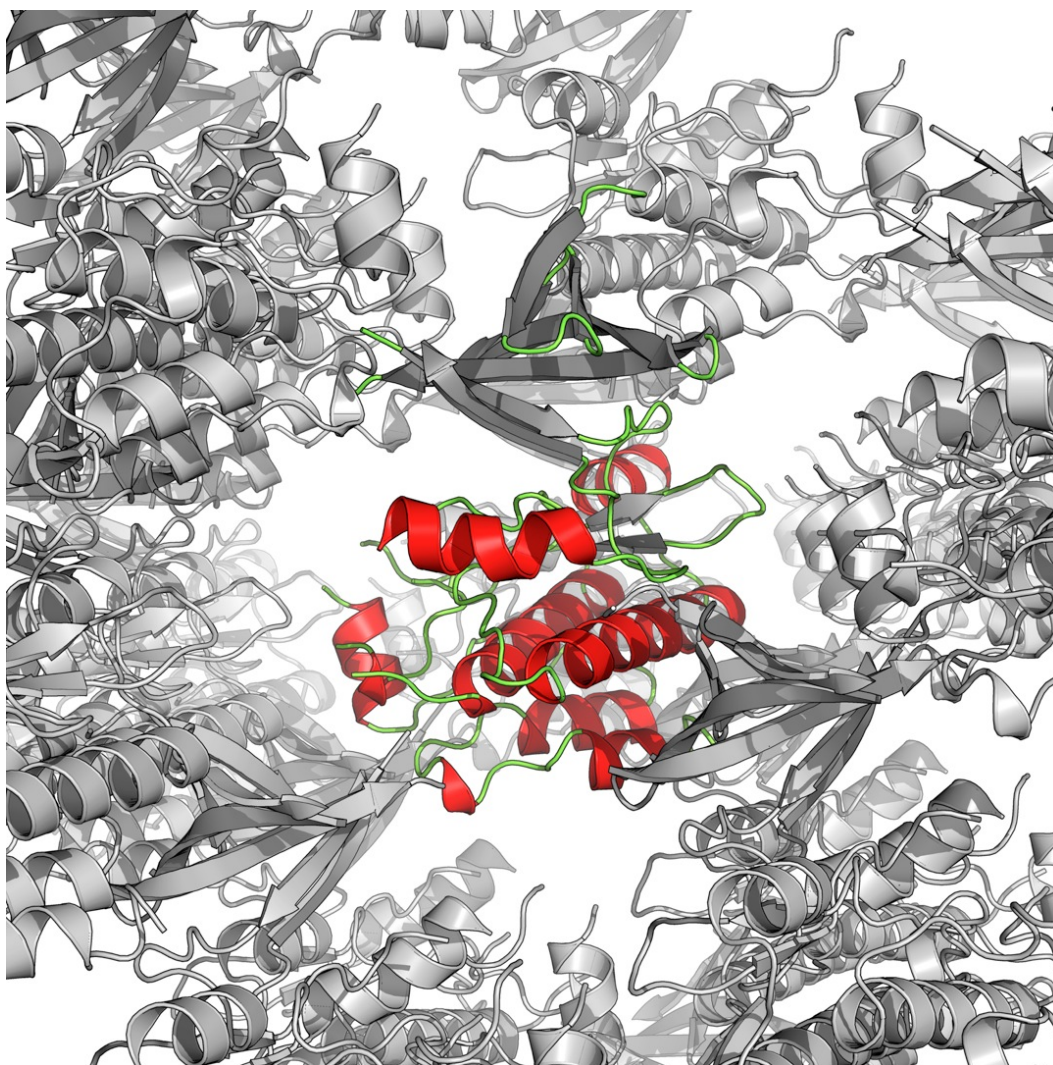


Figure 6.6: Crystal packing for the activated WNK1 kinase domain. The figure displays a large gap between the front of the protein, where the activation loop is located and the adjacent unit cell.

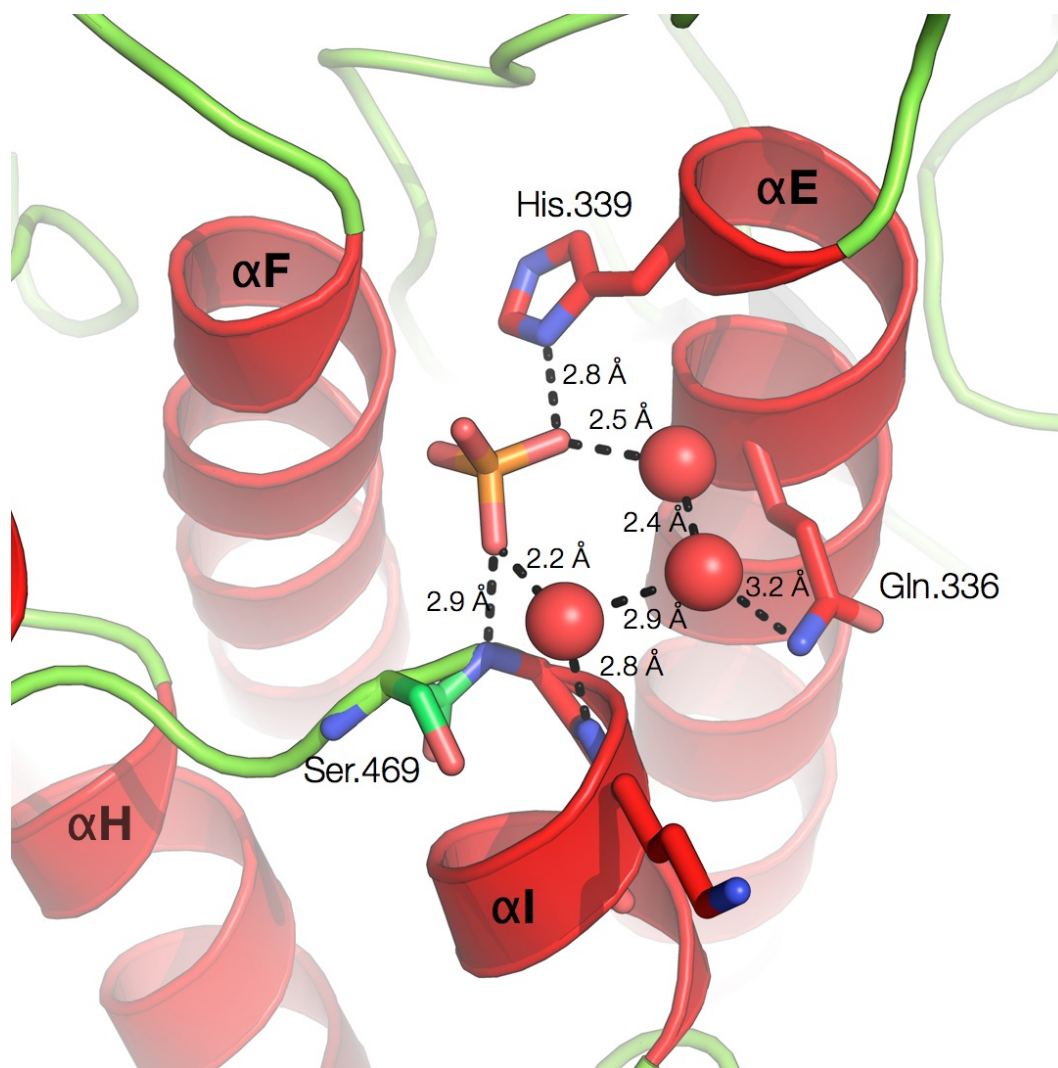


Figure 6.7: Phosphate interaction with $\alpha E/\alpha I$ in C-terminus

α C and the catalytic loop in subunit B of the mutant, inactive structure can be observed and may have aided in crystallization as well, although Min et al (2004) do not note the presence of this sulfate ion in the reported structure or in the crystal conditions. Thus its importance to generation of crystals of the inactive form for data collection can only be speculated.

6.3.2 The active site

The active site of the activated WNK1 kinase retains structural similarity to that of an inactive kinase. The catalytic lysine is pointed into the ATP binding site, and the aspartic acid of the DLG (DFG consensus from other kinases) sequence adopts a similar conformation to that seen in the mutant, inactive kinase. The canonical glycine-rich loop that precedes the catalytic lysine in WNK1 is fully disordered and it may be hypothesized that the flexibility of this loop would allow for ATP to bind and then be stabilized by interactions with the β/γ phosphates from ATP similarly to other kinases. The glutamate from α C (E268) that is required for catalytic activity is located outside the ATP-binding site and is not in a ready position to stabilize K233 for a phosphotransfer reaction.

6.3.3 Comparison to the inactive kinase domain

The structure of the activated WNK1 kinase adopts some similarities to those of both monomers found in the asymmetric unit of the structure of the mutant, inactive kinase domain. The similarities and differences between

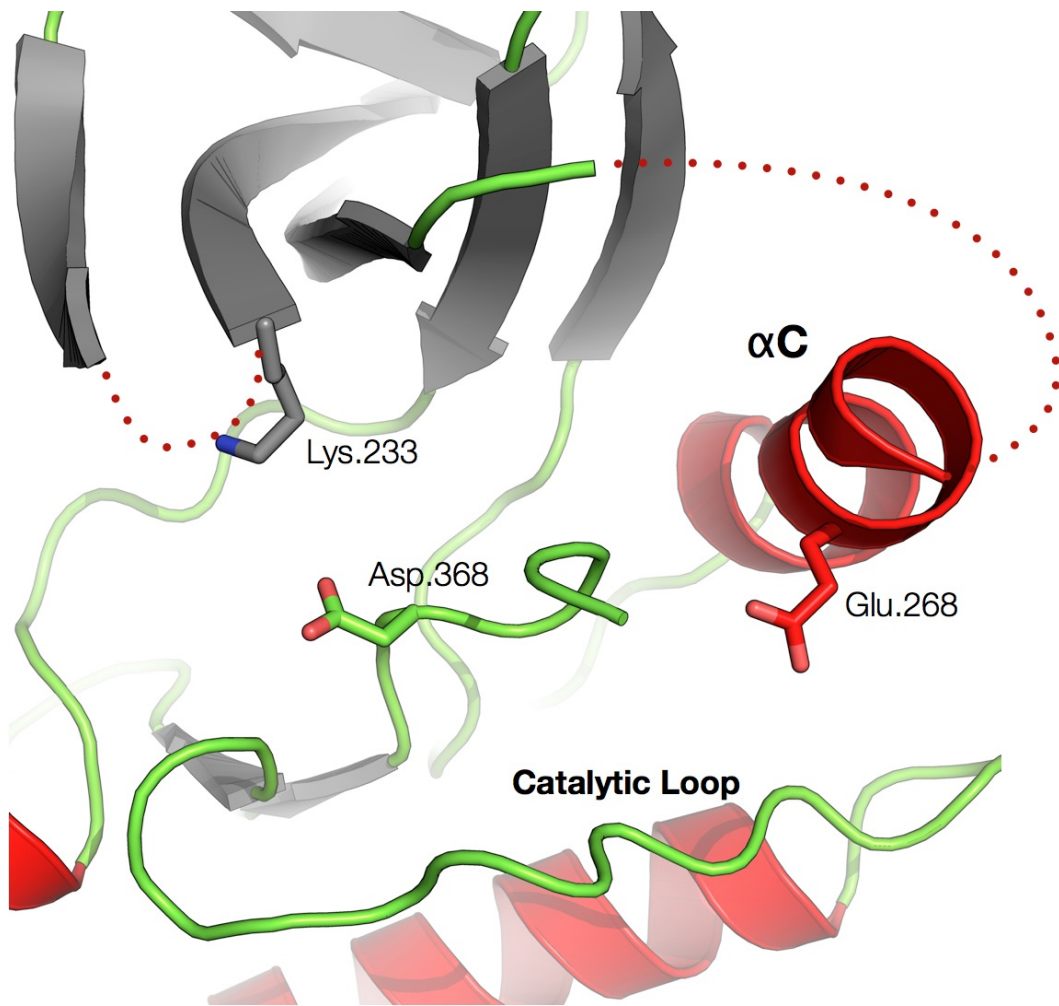


Figure 6.8: Active Site of the activated WNK1 kinase domain

both monomers and the activated kinase can be broken down into two regions: 1) the placement of the catalytic lysine and the N-terminal lobe β strands. 2) the orientation of α C. The remainder of the activated kinase, less the amino acids that do not have any associated electron density, align well with the structures of the inactive monomers including the RFXV and DFG motifs and the catalytic loop.

When comparing just the monomers of the inactive kinase domain, distinct differences between the placement of the β strands in monomer A compared to monomer B become apparent. In the activated WNK1 kinase domain structure, the β strands are shifted toward α C compared to those of monomer A (Figure 6.9a). The disposition of the β strands therefore resembles that of monomer B from the inactive structure. This can be seen more clearly by looking at the placement of the catalytic lysine in Figures 6.9c and 6.9d. In the activated kinase, compared to monomer A, the lysine has been shifted by 1.5 Å up and away from its placement in the inactive structure; whereas, in monomer B, the location of C_α is essentially identical.

The second structural difference between the activated and inactive monomers is the orientation of α C. Unlike the placement of the β barrel, the orientation of α C in the activated structure resembles monomer A most closely due to its orientation away from the ATP-binding site compared to monomer B where α C bends back toward the kinase. This bending of the helix may be due to a crystal artifact caused by the location of a sulfate ion bridging α C and the catalytic loop of monomer B. This sulfate ion is also involved in forming

crystal contacts between asymmetric units.

6.3.4 Comparison of WNK1 Kinase Domain Structures to Active PKA

The term 'activated' and not active is used to describe this structure of the WNK1 kinase domain because, aside from being autophosphorylated at S378 and S382 during expression, the structure appears to be in an inactive conformation relative to the placement of several catalytic residues. In addition, the structure was solved in an *apo* form, devoid of ATP or an ATP analog such as AMP-PNP.

The catalytic lysine (K233) C α is located in a position which is essentially identical to that of the mutant, inactive subunit A placement. Compared to that of PKA, the C α position for this lysine is shifted by one β strand equivalent away from α C and sits directly over the ATP binding site. Although, compared to the structures of the mutant, inactive WNK1 kinase domain, the lysine adopts a slightly different conformation by rotating up and back away from the ATP binding site. Since we do not observe electron density for the glycine-rich region adjacent to the catalytic lysine, this may suggest a mechanism for ATP to bind. It remains to be investigated what the exact placement of the catalytic lysine will be when ATP or an analog binds to the active site.

The second catalytic residue that adopts an inactive conformation is the aspartic acid of the DLG motif, which is known to aid in coordinating Mg²⁺ ions during similar to that found in the structure of active PKA (Zheng et al, 1993). In the activated WNK1 kinase domain structure, this aspartic

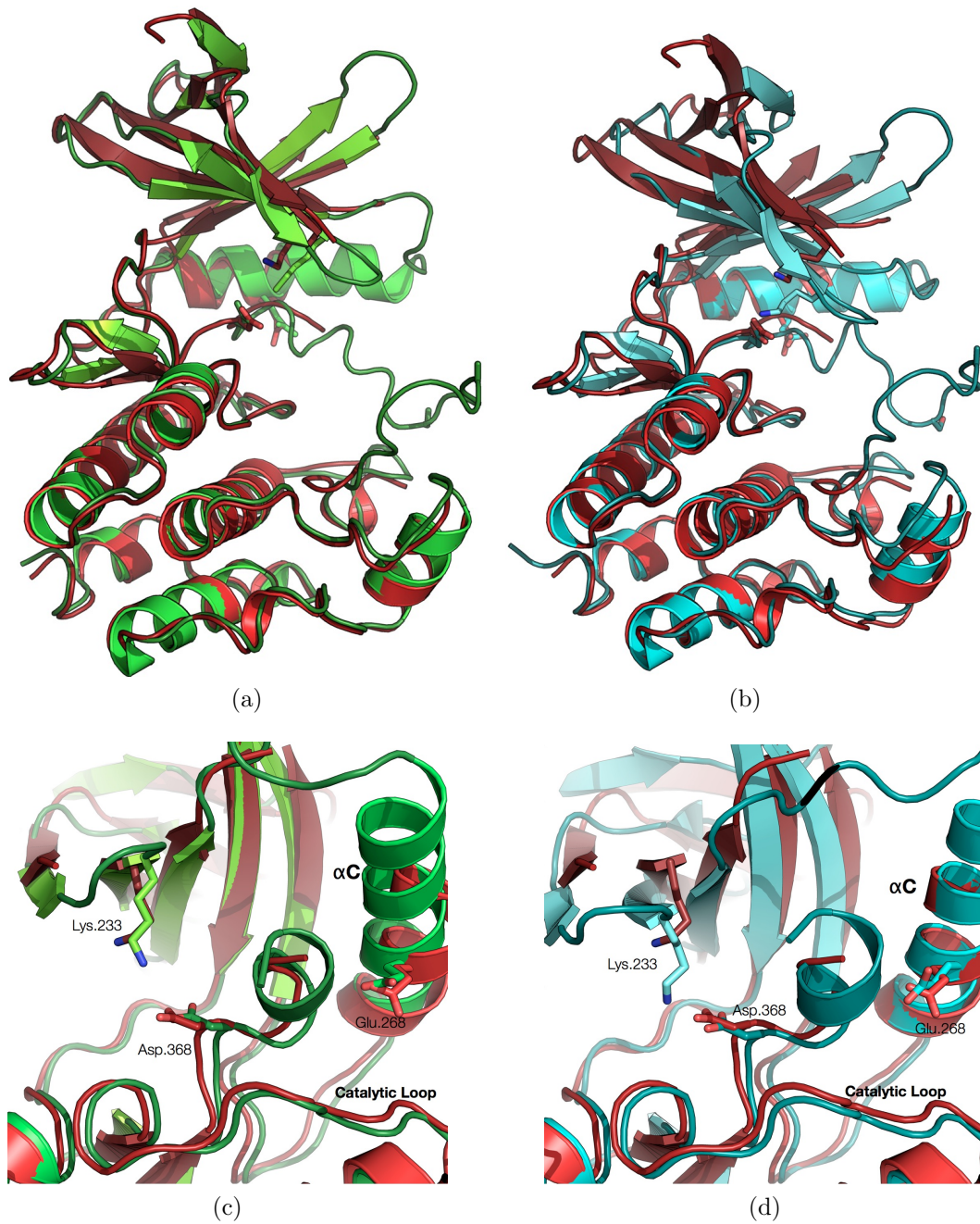


Figure 6.9: a) Structural alignment of the mutant inactive WNK1 kinase domain subunit A (green) with the activated kinase domain (209-483)(red) b) Structural alignment of the mutant, inactive WNK1 kinase domain subunit B (cyan) with the activated kinase domain (red). c),d) active site comparison of the inactive kinase domain subunits A/B respectively with the activated kinase. Min et al (2004)

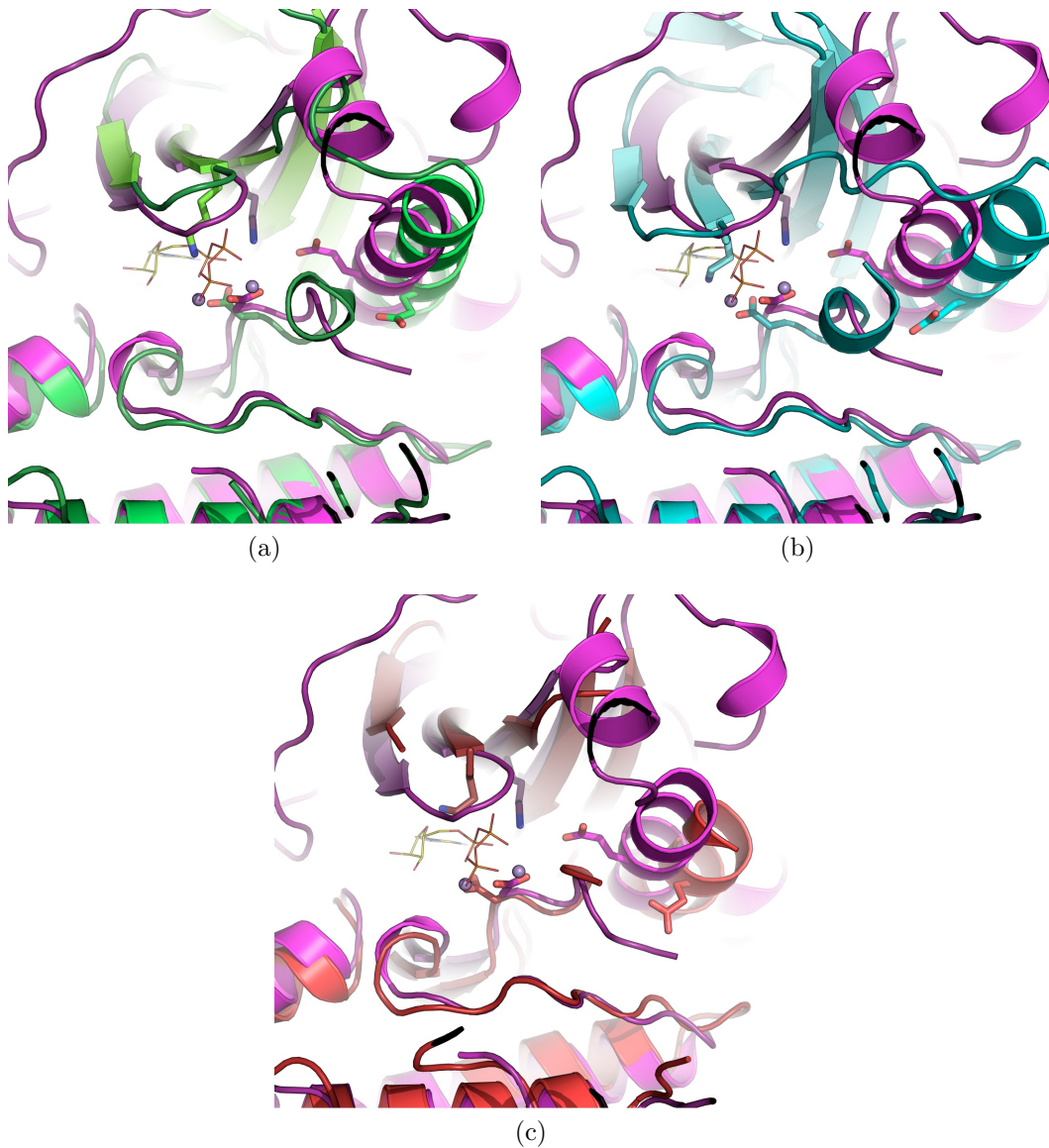


Figure 6.10: a) The active site of PKA (magenta) bound to ATP/Mn²⁺ compared to the inactive kinase domain (WNK1 194-483 S382A) subunit A (green) is shown. b) The active site of PKA (magenta) bound to ATP/Mn²⁺ compared to the inactive kinase domain (WNK1 194-483 S382A) subunit B (cyan) is shown. A shift of the N-terminal β strands downward into the ATP binding site is observed. c) The active site of PKA (magenta) bound to ATP/Mn²⁺ compared to the active kinase domain (WNK1 209-483 S378*,S382*) (red) is shown. The sidechain of the catalytic lysine, compared to that of the inactive monomers is slightly shifted upward out of the ATP binding site and the glycine-rich loop is disordered. Zheng et al (1993)

acid is directed away from the active site and adopts a conformation identical to that of both subunits of the mutant, inactive kinase domain structure.

Glutamic acid 268 is the final catalytic residue that adopts an inactive conformation in the activated WNK1 kinase domain structure. In an active structure, such as that of PKA, this glutamate is inserted into the active site and associates with the catalytic lysine and is thought to help stabilize the lysine during the phosphotransfer reaction. This insertion of the glutamate in the active site is also associated with a concomitant movement of α C toward the center of mass of the kinase domain. In the activated WNK1 kinase domain structure, we see a similar structure to that of both subunits found in the mutant, inactive structure. Notably, the sidechain of this glutamate is disordered but is generally oriented in the same direction as the other two structures. What is interesting in the activated structure is the dynamic nature of α C compared to that of the other two structures of the WNK1 kinase domain. In subunit A of the inactive structure, α C is bent toward the kinase domain's center of mass compared to subunit B where it is straightened and its interaction with the catalytic loop is stabilized by a phosphate group. I believe this is an important feature of the inactivated WNK1 kinase, whether phosphorylated or unphosphorylated. This hypothesis will be discussed in greater detail in the final chapter of the thesis.

Chapter 7

Biochemical and Biophysical Analysis of the WNK1 Kinase Domain

The WNK1 kinase is best known for its involvement in the regulation of CCC activity. Previous articles and reviews of the involvement of WNK1 in this cascade implicated hypertonic conditions as a source of WNK1 activation (Anselmo et al, 2006; Richardson and Alessi, 2008; Zagorska et al, 2006). However, a previous report by Moriguchi et al (2005) shows that substitution of sodium chloride for sodium gluconate caused activation of WNK1 toward its SPAK substrate *in vitro* and *in vivo*. Here, it is demonstrated that increasing sodium chloride levels *inhibits* WNK1 kinase activity *in vitro* ($IC_{50}=130$ mM). Further, increasing sodium chloride concentrations cause an increase in midpoint melting temperature of the WNK1 kinase domain as assessed by differential scanning fluorimetry. This effect appears to be driven by a single binding-site interaction of the WNK1 kinase domain with chloride ion, based on the hyperbolic shape associated with plotting T_m as a function total amount of chloride present. This suggests a mechanism of salt regulation in cells driven by chloride influx through the CCCs.

7.1 Biochemical analysis of the WNK1 kinase

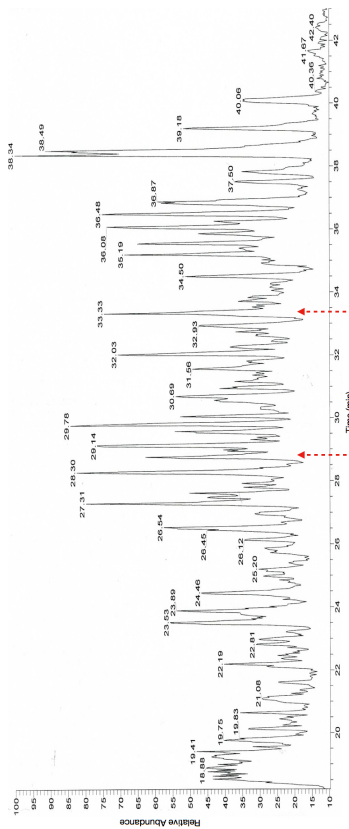
7.1.1 Mass spectrometry analysis of the WNK1 kinase domain and associated mutants

To probe the phosphorylation state of the activation-loop of the WNK1 kinase domain, purified WNK1 194-483 and associated activation-loop mutants were purified from *E. coli* and purified to homogeneity. The resultant proteins were subjected to digestion with chymotrypsin, the resultant peptides were separated by reverse-phase HPLC and analyzed by electrospray ionization mass spectrometry (ESI/MS).

When the wild-type kinase domain of WNK1 was analyzed following purification, WNK1 is doubly phosphorylated at S378 and S382 (7.1). No peptides associated with unphosphorylated forms of the activation loop were found. This observation suggests that WNK1 autophosphorylates during *E. coli* expression (Figure 7.1). To test whether mutations of these serines to aspartic acid or alanines would affect phosphorylation, constructs of 194-483 with the following mutants were expressed and purified to homogeneity (S378D, S378A, S382D, S382A)¹.

For mutants associated with S378, it was observed following ESI/MS analysis that the kinase is monophosphorylated at S382 as seen in Figure 7.2. The unphosphorylated peptide for this site was searched for in the dataset and, although it is absent, its absence does not completely rule out that there may

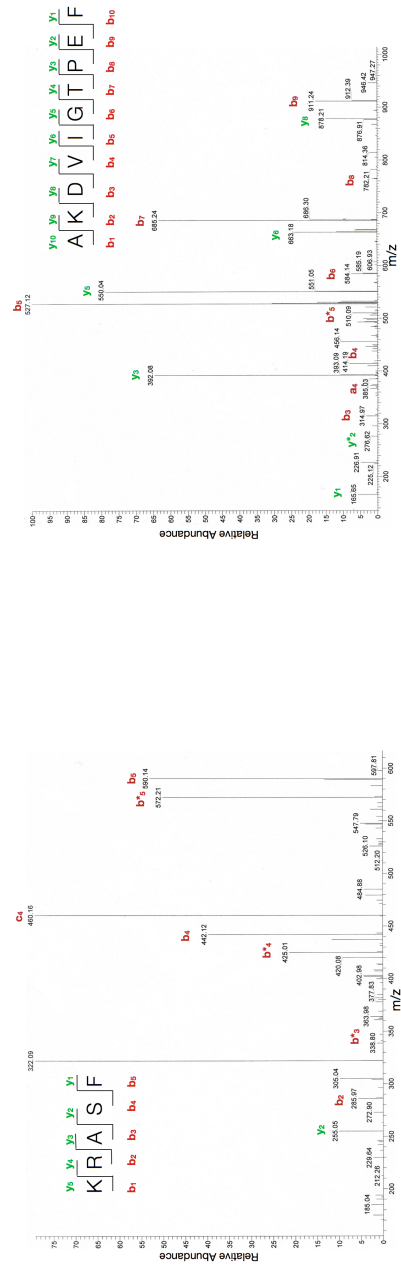
¹ESI/MS data for mutants S378D and S382D are shown graphically. The data for the mutants S378A and S382A was not able to be found in the computer although notes in the laboratory notebook corroborate the observations presented. Obviously, these data will need to be replicated if they are to be published.



KRASF (28.88 min)

AKDVIQTPEF (33.33 min)

(a)



(b)

(c)

Figure 7.3: ESI/MS of WNK1 194-483 S382D

be a small fraction of unphosphorylated peptide that may or may not have been adequately separated or selected by the instrument to be analyzed due to low sample abundance. However, the current data collected suggest that these two mutants still allow for the WNK1 kinase domain to autophosphorylate to near homogeneity at S382.

When the mutations associated with S382 were analyzed, peptides which were identified as the *unphosphorylated* peptide containing S378 were found (Figure 7.3). In a similar phenomenon to what was previously described, the phosphorylated peptide from the activation loop could not be identified in the dataset. This may indicate that mutation of S382 is not amenable to be mimicked by aspartic acid and that abolition of the phosphorylation site at S382 prevents autophosphorylation at S378. Notably, S382 is homologous in sequence to the primary activating serine in serine/threonine protein kinases.

7.1.2 Activity assays of the WNK1 kinase domain

Xu et al (2002) had observed autoinhibition of WNK1 protein kinase activity when the kinase domain was expressed *in cis* with the autoinhibitory fragment (1-555). The authors also observed inhibition *in trans*. To try and recapitulate these results, the WNK1 autoinhibitory domain (480-572) was incubated with the activated kinase domain in the presence of MBP substrate and γ -³²P-ATP, no appreciable inhibition of kinase activity was observed (Figure 7.4). The experiment was repeated in triplicate and extended to include a 100-fold molar excess of WNK1 autoinhibitory domain relative to the

kinase domain. Even with this change, and controlling for the possibility of WNK1 phosphorylation of the autoinhibitory domain, *in trans* autoinhibition of the WNK1 kinase domain was not observed.

Considering that WNK1 appeared to be activated by hyperosmotic

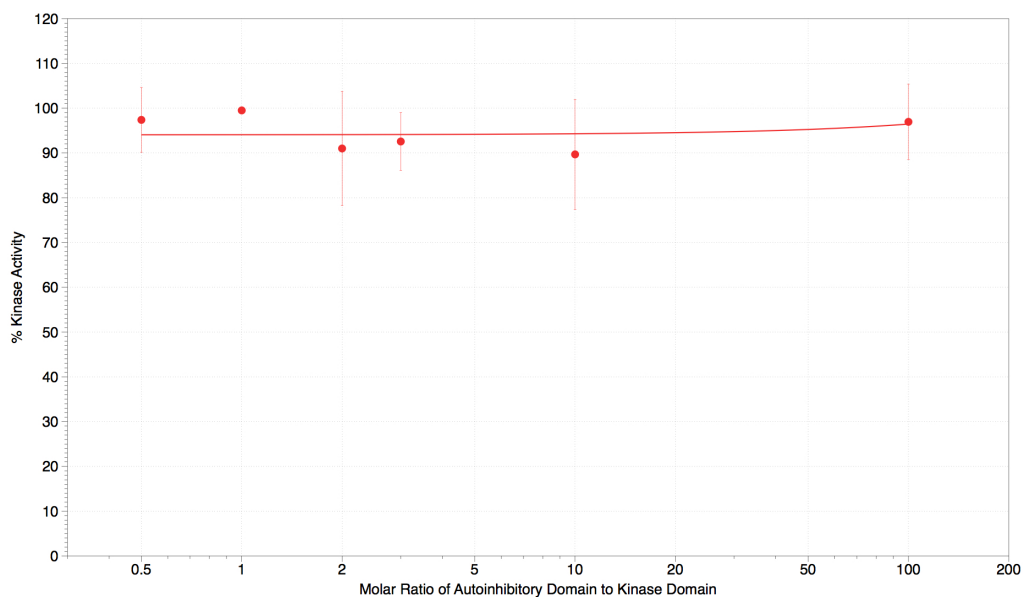


Figure 7.4: WNK1 kinase (194-483) activity while titrated with WNK1 (480-572)

conditions as described by Xu et al (2002), an activity assay was run to assess the effectiveness of the autoinhibitory domain in varying concentrations of sodium chloride. For this assay, two sets of reactions were run simultaneously: 1) an assay to probe kinase activity in the presence of varying salt concentration (as a control) and 2) an assay to probe kinase activity in the presence of one molar equivalent of the WNK1 autoinhibitory domain (480-572). When the reactions were run, it was observed that the kinase activity in the pres-

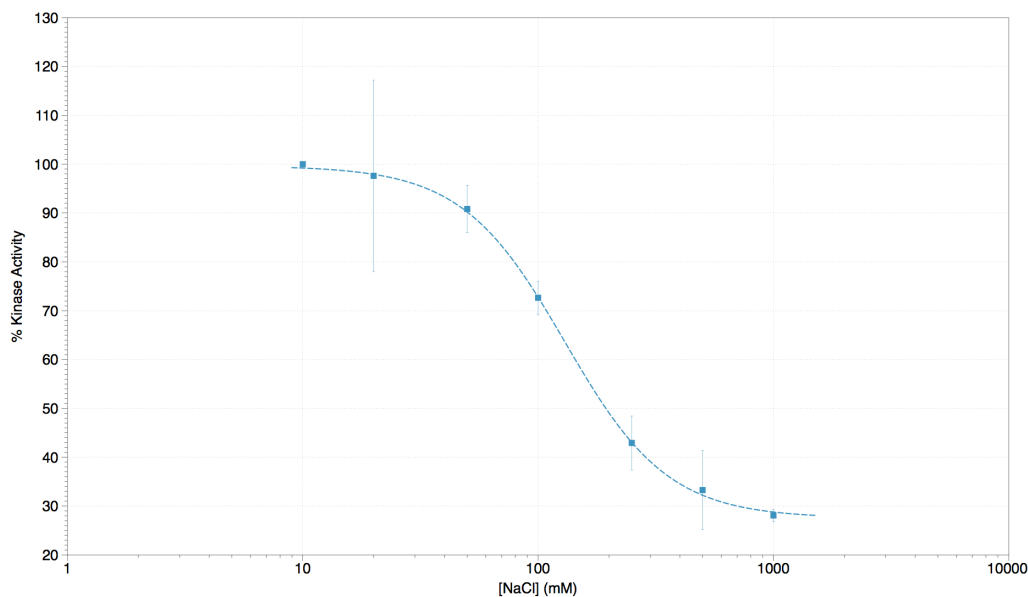


Figure 7.5: WNK1 kinase (194-483) activity while titrated with NaCl. The kinase is inhibited by increasing NaCl concentrations with an IC_{50} of 130 ± 1 mM.

ence of one molar equivalent of WNK1 autoinhibitory domain decreased as the sodium chloride concentration increased. However, the same observation was recorded for the control experiment (Figure 7.10) After repeating the control experiment in triplicate, it was concluded that the WNK1 kinase is *inhibited* by exposure to hypertonic solution with an IC_{50} of 130 ± 1 mM (Figure 7.5).

7.2 Biophysical analysis of the WNK1 kinase domain by Differential Scanning Fluorimetry

To test the hypothesis that WNK1 kinase activity is inhibited by exposure to increasing sodium chloride concentrations, an assay for biophysical changes associated with the interaction of the WNK1 kinase domain with

sodium chloride was designed. The experimental technique of differential scanning fluorimetry (DSF) utilizes the temperature associated with the physical unfolding of a globular protein as a measure of protein stability. Fluorescence intensity measurements of a small-molecule fluorophore are recorded at discrete temperatures as a Peltier block heater increases the sample temperature incrementally.

As the temperature increases and the population of protein in the sample begins to unfold, the fluorescent dye can interact with the newly exposed hydrophobic parts of the protein. Normally, the fluorophore is quenched in the presence of aqueous solvent but the binding to exposed hydrophobic patches in the protein allows the fluorophore to emit light. The raw data, as shown in Figure 7.6 are a sigmoidal curve which can be differentiated in the signal dimension to yield a curve with a single point maximum which corresponds to the inflection point of the raw fluorescent data. This point is called the midpoint melting temperature (T_m) of unfolding of the protein. If DSF is run in the presence of a ligand that associates with the protein of interest, the T_m is shifted to a higher value because of internal stabilization of the protein from contacts from the protein to the ligand (Pantoliano et al, 2001; Niesen et al, 2007).

To assess whether the decrease in WNK1 activity could be associated with a physical change in WNK1 kinase domain stability, an initial DSF experiment was conducted on wild-type WNK1 194-483 under the same array of concentrations of sodium chloride as tested in the activity screen. The

experiment showed that the WNK1 kinase domain responded to rising salt concentrations by an observed increase in thermal stability (i.e. resistance to unfolding) as seen in Figure 7.7. When mutants of the WNK1 kinase domain S378A and S832A were run independently, the graphs display similar curvature to that of the wild-type kinase domain; but, the S378A mutant was generally destabilized and showed a downward shift in the T_m by 6°C.

To test whether this property of stabilization in the presence of increasing salt was unique to the WNK1 kinase, control experiments utilizing the MAP kinase cascade components of TAO2, MEK6, and p38 α were run in the presence of increasing sodium chloride concentration. As shown in Figure 7.8, the MAP kinase cascade components do not display a similar profile compared to that of the WNK1 kinase. The MAP1K, MAP2K, and MAP3K kinases, instead, follow a linear trajectory relative to increasing sodium chloride concentration. Further, in research involving the phosphorylation of MEK6 by TAO2, John Humphreys, Ph.D. ran activity assays of TAO2 toward MEK6 substrate in increasing quantities of sodium chloride and saw no appreciable change in kinase activity of TAO2 (data not shown).

As a final DSF assay, the wild-type WNK1 kinase domain (194-483) was tested to determine if the kinase may be responding as an effect of cations or anions binding to the kinase domain. To run this experiment, a series of cation-chloride salts (LiCl, NaCl and KCl) were assayed by increasing the concentration of the salts over the same range as tested in previous experiments. A similar panel was conducted with sodium-anion salts (NaCl, NaBr, NaI).

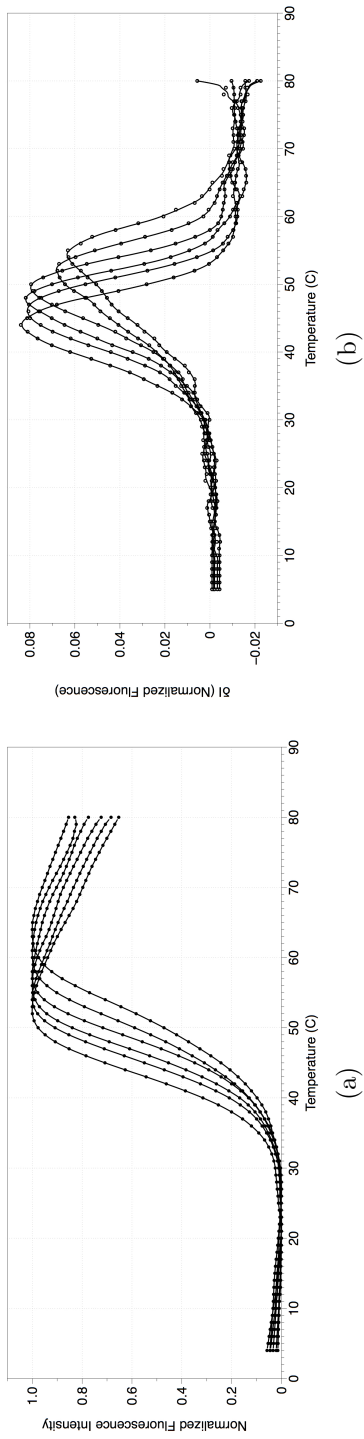
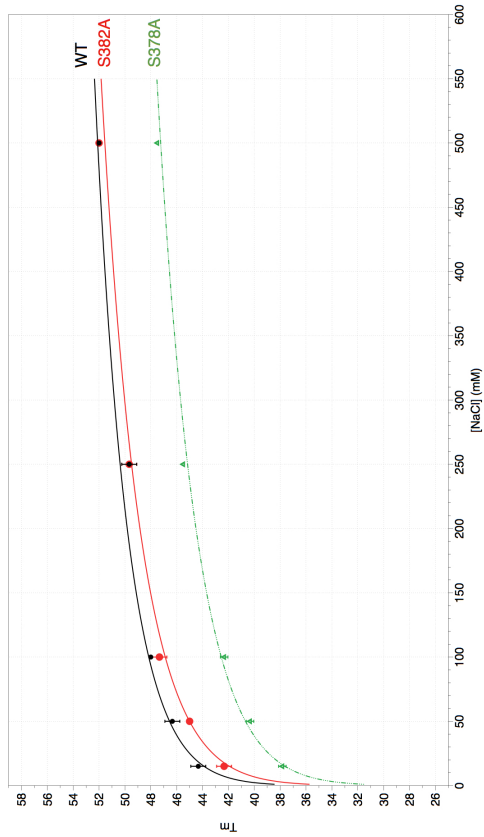
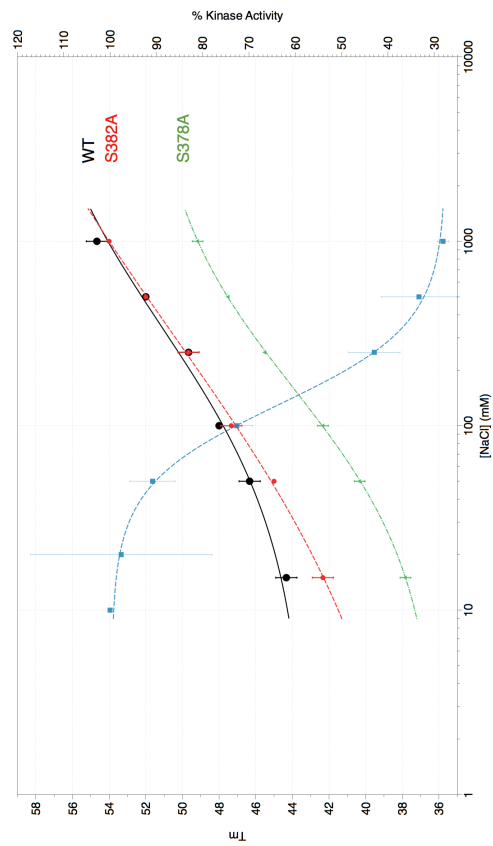


Figure 7.6: DSF raw data curves of WNK1 kinase domain and associated mutants while titrated with NaCl.



(a)



(b)

Figure 7.7: DSF curve of WNK1 kinase domain and associated mutants while titrated with NaCl.

As seen in Figure 7.9a and 7.9b, the cation screen displayed similar curves to that of sodium chloride; however, when the anion panel was run, there was no appreciable change associated with bromide substitution but a marked change in curvature when iodide was used (Figure 7.9c,7.9d).

7.3 Discussion

Activity assays of the WNK1 kinase domain paired with stability curves assessed by DSF point toward a unique role for the WNK1 kinase in the signaling cascade that is thought to regulate salt reuptake in the distal convoluted tubule of the kidney (Anselmo et al, 2006; Richardson and Alessi, 2008; Zagorska et al, 2006). Currently, WNK1 is the principal kinase in the cascade, and no direct activators of the WNK1 kinase have been discovered to date. The activity of WNK1 is clearly influenced by the concentration of sodium chloride present in the reaction buffer. Moreover, the calculated IC_{50} value of 130mM is thought to be within the physiological operating concentration of chloride in kidney cells (30-230 mM) (Gedde et al, 1997; Stokes, 1989; Reilly and Ellison, 2000; Macknight, 1985; Cook and Macknight, 1984).

The tracking of the midpoint melting temperatures associated with each assayed sodium chloride concentration fits a one-site binding curve for all activation loop mutants and wild-type WNK1 kinase domain. The single site binding appears to be anion specific as assessed by the flattening of the curve when the kinase domain was exposed to sodium iodide. As well, the flattening of the curve in response to the presence of iodide suggests a discreet

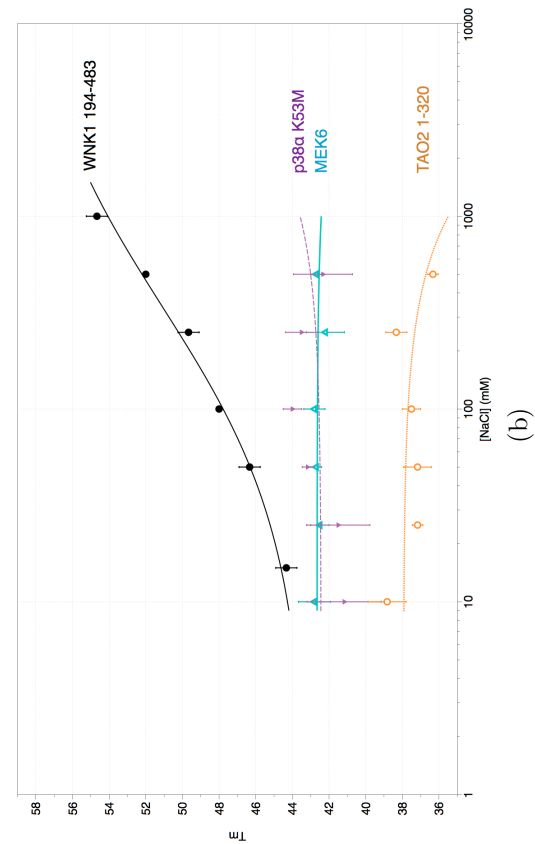
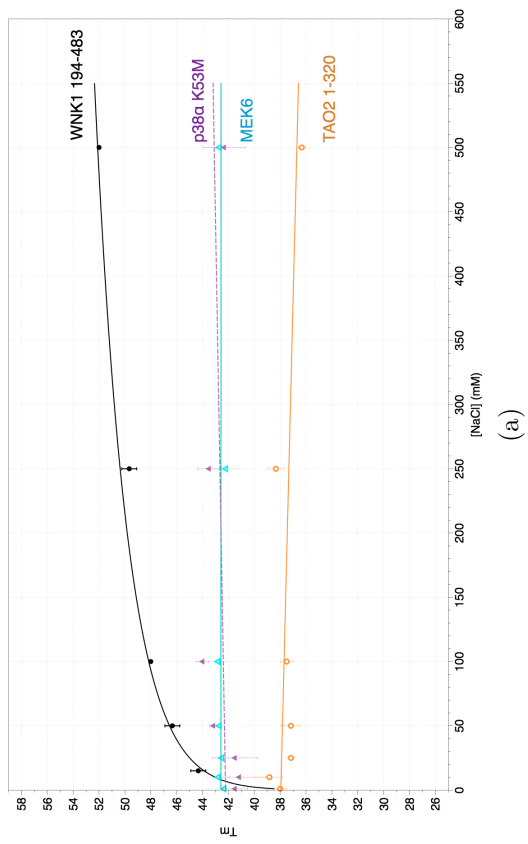


Figure 7.8: DSF curve of WNK1 and MAP kinases titrated with NaCl.

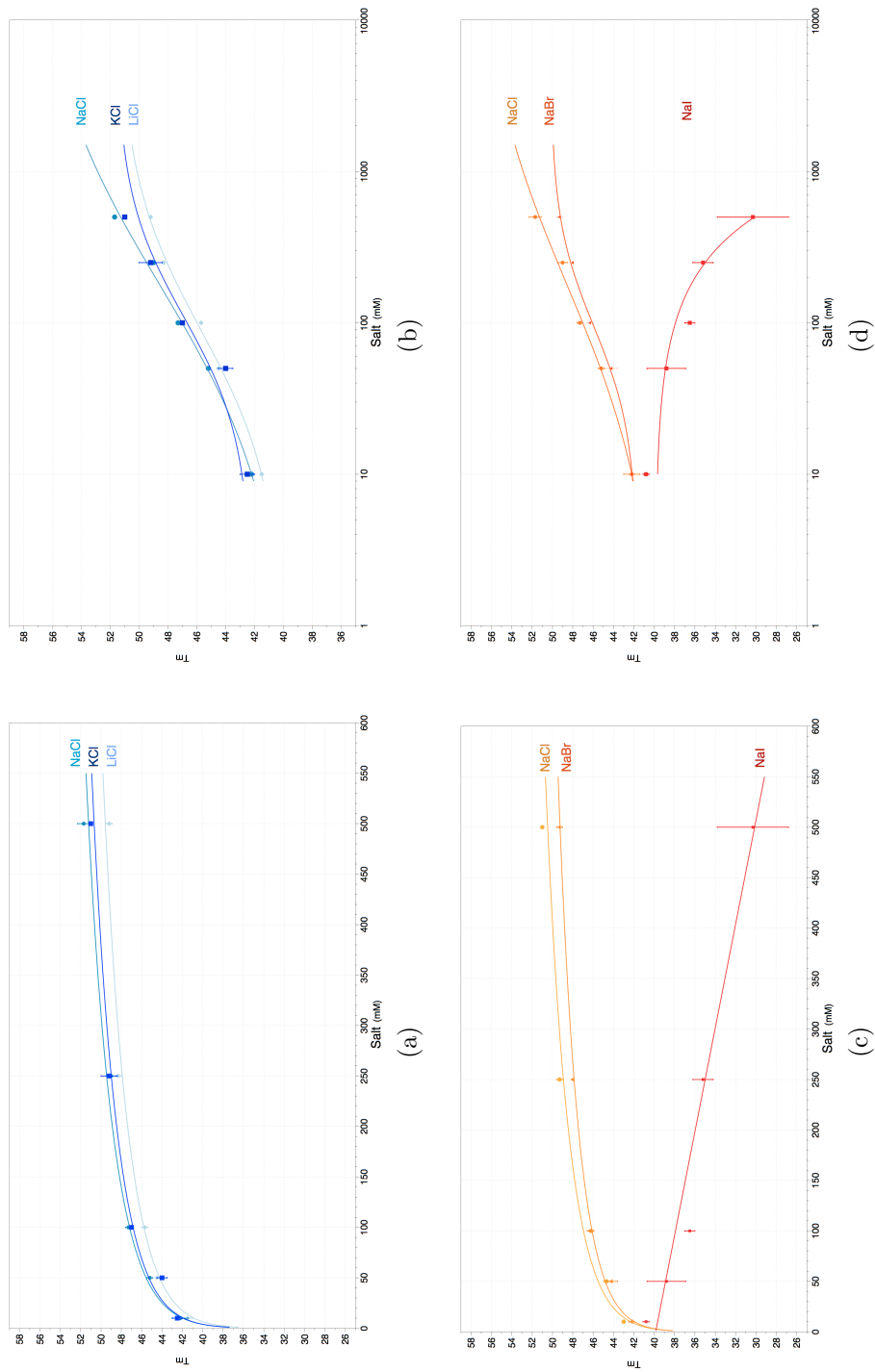


Figure 7.9: DSF curve of WNK1 kinase domain titrated with different salts.

binding site that is not accessible due to steric interactions by the large ionic radius of iodide. However, since bromide is able to bind, one can assume that the binding site allows for an ionic radius of at least the size of a bromide ion. Since the difference in ionic radius between bromide and iodide is 0.3 Å, compared to a 0.1 Å difference between chloride and bromide, the tolerance for the site seems to be quite low.

The *in trans* autoinhibition of the WNK1 kinase domain by the autoinhibitory domain could not be replicated using the refined autoinhibitory domain construct used to calculate the solution structure. In a 10mM concentration of sodium chloride, there was no change in kinase activity spanning from fractions of molar equivalences up to 100-fold molar excess of autoinhibitory domain. From the data collected, it is not clear why this is the case. However, what we know from comparing the construct dimensions of the domain used in Xu et al (2002) to that used to solve the solution structure of the autoinhibitory domain, there are significant structural features that were omitted in the former construct. The construct expressed with residues 485-555 lacks the first β strand and terminal α helix that interact to form tertiary structure features. It is unclear what structure the autoinhibitory domain construct of 485-555 would take when expressed. However, from our initial characterization of this autoinhibitory domain fragment, the 485-555 construct was insoluble when cleaved from the GST tag (see Chapter 2). Furthermore, in the assay conditions cited, GST-tagged autoinhibitory domain was mixed with GST-tagged kinase domain. Therefore, the mixed heterodimerization of

GST constructs may have influenced the local concentration of the autoinhibitory domain relative to the kinase domain and influenced the measured IC_{50} reported by Xu et al (2002).

7.4 Experimental design and protocol

7.4.1 Mass spectrometry

To collect information on the phosphorylation state of wild-type and mutant forms of the WNK1 kinase domain following expression and purification from *E. coli*, 1000 pmol of WNK1 kinase was digested in a 25:1 molar ratio with chymotrypsin in the presence of 100 mM Tris pH=8.0, 10 mM $CaCl_2$ and 0.3 mM $MgCl_2$ (100 μ L total reaction volume). The reaction was allowed to proceed at 37°C overnight. Following digestion, 25 μ L of reaction mixture was added to a vial suitable for injection onto an Agilent 1100 HPLC and eluted off of a C18 reverse-phase column using a gradient of acetonitrile from 4% to 30%. As the peptides are eluted from the column, they are injected onto a LCQ Deca XP (Thermo) fitted with an orthogonal ESI source. For tandem MS identification, Helium was used as a collision source to fragment the peptides of interest. The data was analyzed by Xcalibur (Thermo) and MASCOT (Matrix Science).

7.4.2 Activity assays

To repeat the experiments involving *in trans* inhibition of WNK1 by its autoinhibitory domain as presented in Xu et al (2002), the new construct

of the autoinhibitory domain (WNK1 480-572) was titrated *in trans* into a kinase assay monitoring WNK1 ^{32}P incorporation into the generic kinase substrate MBP. The titration utilized a total concentration of $2\mu\text{M}$ WNK1 194-483 S378*,S382* in a 1:10 molar ratio to MBP substrate. The experimental setup is shown in detail as Table 7.1. To summarize, doubly distilled water, MgCl_2 and HEPES (pH=8) were aliquotted into individual tubes. WNK1 194-483 and WNK1 480-572 were prethawed on ice from storage at -80°C and added to the tubes following the precalculated volumes given the specified concentration protein in the tube. MBP substrate was added and the reaction mixture was incubated on ice while the ATP mixture was made. In a fume hood fitted for radioactivity assays, radiolabeled $\gamma\text{-}^{32}\text{P}\text{-ATP}$ (25 mCi) and unlabeled ATP were premixed in a 3.33 molar excess of hot ATP to cold. To begin each reaction, $1.3\mu\text{L}$ of ATP mixture was combined with the premixed reaction to make a combined $30\mu\text{L}$. The reactions were incubated with ATP mixture in 1 minute intervals and placed sequentially into a 30°C water bath and allowed to incubate for 1 hour.

Detection by phosphor screen

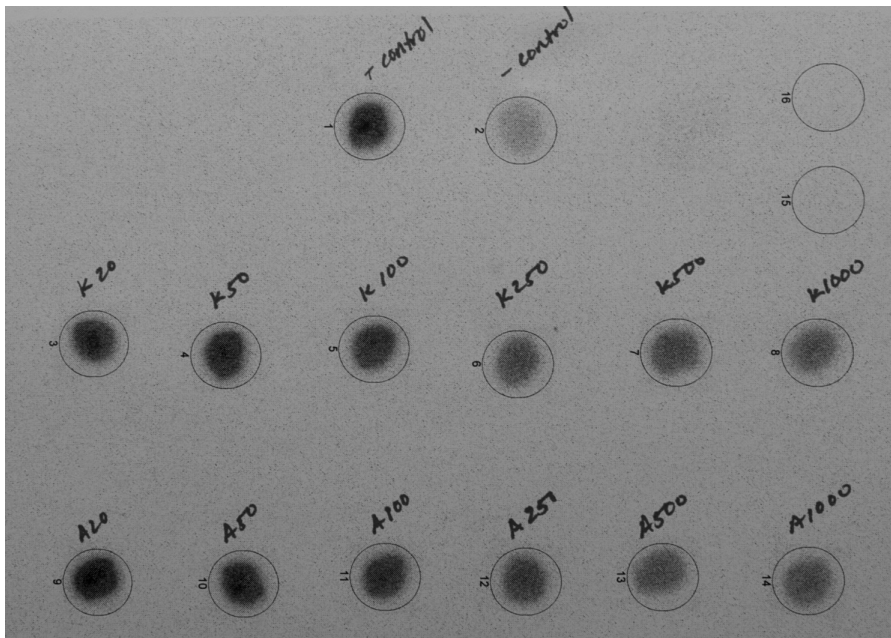
To terminate the reaction, $20\mu\text{L}$ of sample from each reaction was blotted onto a $1\text{cm} \times 1\text{cm}$ piece of cellulose paper and allowed to air dry for 10-15 seconds before being plunged into a 10% solution of trichloroacetic acid in water. The spotted reactions were washed a minimum of 3 times to wash away any residual radioactivity not covalently attached to the MBP absorbed onto

the cellulose. To ensure that the residual radioactivity was removed, the negative control-which was run in the absence of WNK1 kinase domain-was tested for radioactivity by detection with a Geiger counter. The cellulose squares were dried using a vacuum gel drier and were then exposed to a phosphor screen at room temperature for 2 hours. The total number of counts were determined by reading the phosphor screen with a Storm Molecular Imager (Molecular Dynamics).

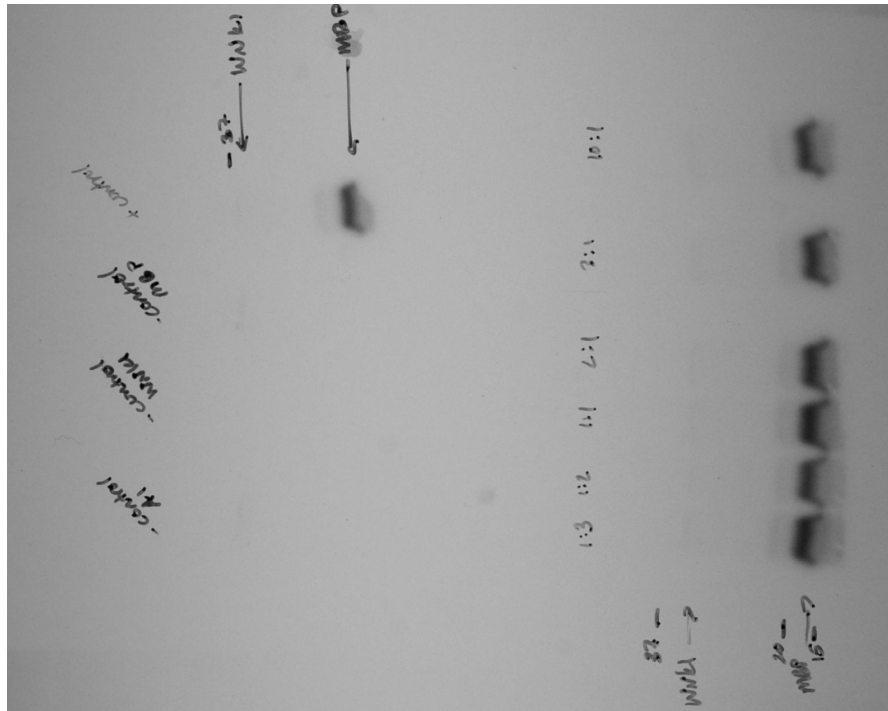
Detection by scintillation counting

Following incubation at 30°C, 10 μ L of 4X SDS-Coomassie (Laemmli's) buffer was added to the reaction mixtures and boiled for 3 minutes. The samples were separated on a 12% SDS-PAGE gel (BioRad) and stained overnight with Coomassie brilliant blue. The following morning, the gel was destained twice (1 hour/destain cycle) and exposed to photosensitive film (KODAK BioMax XAR) for 1 hour to detect radiolabeling of MBP. This was followed by a two hour exposure on the phosphor plate with quantitative detection by a Storm Molecular Imager. This was followed by band excision of phosphorylated MBP from the PAGE gel and incubating the excised fragments in 1mL of scintillation fluid. The vials were then analysed by a scintillation counter. In general, there was no statistical difference between analysis by bulk counting (cellulose-blotting) and scintillation counting of excised band fragments.

Measuring salt sensitivity



(a)



(b)

Figure 7.10: Raw sample activity data for WNK1 194-483

To assess the WNK1 kinase domain's sensitivity to sodium chloride, the molar equivalence of autoinhibitory domain added was replaced by a total concentration of NaCl in the reaction vial. The specific reaction conditions can be found in Table 7.1 but are essentially identical to that described for measuring kinase domain activity in the presence of the autoinhibitory domain.

7.4.3 Differential scanning fluorimetry

To run the differential scanning fluorimetry experiments, a total of $75\mu\text{L}$ of sample was prepared for each salt titration and divided into three separate wells on the 96-well plate to test for pipetting error. Therefore, a total volume of $25\mu\text{L}$ is used for each well volume on the 96-well plate. It is important to set the instrument to a different well volume if a $50\mu\text{L}$ sample or if a different type of 96-well plate is desired.

To prepare each sample, the protein sample to be tested is thawed on ice for 30 minutes and centrifuged at 13,000 rpm for 5 minutes to remove any precipitate and to degas the sample. In a $500\mu\text{L}$ snap cap tube on ice, the protein sample, 10mM Tris pH=8.0 and NaCl are combined. When utilizing the WNK1 protein kinase, a typical protein concentration for a $75\mu\text{L}$ sample is $5\mu\text{M}$, or a total of 375pmol of protein. After combining the premixed kinase, buffer and salt, $1\mu\text{L}$ is taken from the 5000X concentrated dye and diluted 1/1000 in water. This solution of 5X SYPRO orange is then added to the mixture of protein, buffer and salt which dilutes the starting solution by a

Table 7.1: Protocol for activity assays of the WNK1 kinase domain

	Controls			Molar Ratio of AI domain:Kinase domain						
	(+)	(-) MBP	(-) WNK1KD	(-) WNK1AT [‡]	1:3	1:2	1:1	2:1	3:1	10:1
H ₂ O (μ L)	17.3	19.7	21.7	18.9	17	16.9	16.4	15.6	14.8	13.9
1M HEPES pH=8.0 (μ L)	1	1	1	1	1	1	1	1	1	1
1M MgCl ₂ (μ L)	0.5	0.5	0.5	0.5	0.5	0.5	0.5	0.5	0.5	0.5
100mM Benzamidine (μ L)	0.5	0.5	0.5	0.5	0.5	0.5	0.5	0.5	0.5	0.5
100mM DTT (μ L)	0.5	0.5	0.5	0.5	0.5	0.5	0.5	0.5	0.5	0.5
2mg/mL BSA (μ L)	4.5	4.5	4.5	4.5	4.5	4.5	4.5	4.5	4.5	4.5
5mM ATP (μ L)	0.3	0.3	0.3	0.3	0.3	0.3	0.3	0.3	0.3	0.3
γ - ³² P-ATP (μ L)	1	1	1	1	1	1	1	1	1	1
30pmol/ μ L (1mg/mL) WNK1 194-483 [†] (μ L)	2	2	-	2	2	2	2	2	2	2
10mg/mL MBP (μ L)	2.4	-	-	-	2.4	2.4	2.4	2.4	2.4	2.4
70pmol/ μ L WNK1 480-572 (μ L)	-	-	-	0.85	0.29	0.4	0.85	1.7	2.5	3.4
Total Vol.	30	30	30	30	30	30	30	30	30	30

[†] Buffer is 10mM Tris pH=8.0, 100mM NaCl

[‡] Control was conducted to determine whether WNK1 phosphorylated its own autoinhibitory domain

factor of two. This procedure makes a final SYPRO working concentration of 2.5X and dilutes the protein premix to the proper concentration for analysis.

The fractions, which were premixed, are then divided into 25 μ L samples and placed into the 96-well plate using a 1 well spacer between each sample on the plate. The plate was then centrifuged at 3000 rpm at 4°C for 5 minutes to remove any bubbles created by pipetting. A CFX-96 (BioRad) with real-time PCR capabilities was utilized for DSF analysis of the WNK1 kinase domain. The fluorescence intensity of SYPRO orange was probed by using a broad-spectrum excitation followed by detection with a FAM-filtered diode array detector. The temperature in each well was cycled from an initial 4°C to 80°C using 0.5°C increments. The detected signal was exported to an EXCEL file spreadsheet (Microsoft) and analyzed by Prism (GraphPad) to generate normalized fluorescence curves. These curves were differentiated along the temperature value to generate a single peak maximum which corresponds to the midpoint melting temperature (T_m) of the protein. For each protein examined, the T_m value was plotted for each concentration of NaCl. The experiments were repeated in triplicate and error bars plotted as the standard deviation.

7.4.4 Expression and purification of WNK1 constructs

The expression and purification of WNK1 194-483 S378*, S382* is essentially the same as it was described for WNK1 209-483 S378*, S382* (Chapter 5) and WNK1 480-572 (Chapter 2). Briefly, recombinant WNK1 194-483

Table 7.2: Protocol for DSF of the WNK1 kinase domain

	15 [‡]	20 [‡]	50 [‡]	100 [‡]	250 [§]	500 [§]	1000 [§]
	[NaCl] (mM)						
100pmol/ μ L WNK1 194-483 [†] (μ L)	3.75	3.75	3.75	3.75	3.75	3.75	3.75
NaCl (μ L)	0.75	1.13	3.38	7.13	3.68	7.43	14.9
10mM Tris pH=8.0 (μ L)	33	32.6	30.4	26.6	30.1	26.3	18.9
5X SYPRO Orange (μ L)	37.5	37.5	37.5	37.5	37.5	37.5	37.5
Total Vol.	75	75	75	75	75	75	75

[†] Buffer is 10mM Tris pH=8.0, 100mM NaCl

[‡] 1M NaCl stock

[§] 5M NaCl stock

was expressed in Rosetta (Novagen) *E. coli* and grown in Luria broth supplemented with ampicillin and chloramphenicol to an optical density (595 nm) of cells equal to 0.6 and induced by adding a final concentration of 1mM IPTG. The cells were shaken at 220rpm for 18-20 hours at 20°C and harvested by centrifugation at 4000rpm for 35 minutes. Cell pellets were resuspended in 5mL of Ni buffer A per liter of cells harvested, flash frozen in N_{2,l} and stored at -80°C, until the protein was purified.

To purify the protein, the pellets were thawed in hot water and incubated with 1mL of protease inhibitor cocktail (Sigma) per liter of cells expressed. The cells were lysed by homogenization in an Emulsiflex C5 (Avestin) using at least three passes through the machine. The homogenized lysate was centrifuged at 40,000 rpm for 1 hour at 4°C and the supernatant was passed through a 0.45μm filter to clarify. The clarified lysate was loaded onto a Ni-sepharose column (GE) pre-equilibrated with Ni buffer A and eluted on a linear gradient with a final imidazole concentration of 250mM.

The single peak from the elution was dialyzed overnight into Mono Q buffer A containing 1 milligram of TEV protease. A key step in the purification protocol of the WNK1 kinase domain is the first dialysis step in the presence of TEV protease. During this step, there is significant precipitation of *E. coli* proteins without loss of the WNK1 kinase domain. Following dialysis, the sample is passed through a 0.45μm filter unit and a 3mL sample of pre-rinsed Ni-agarose beads to remove any His₆ tag cleavage products and protein that was not cleaved and the TEV protease. The resulting sample was

concentrated and loaded into a 10mL SuperLoop (GE).

The protein was then loaded onto a positively charged quaternary amine Mono Q 5/5 column (GE) and eluted on a gradient with a final NaCl concentration of 500mM. Without the His₆ tag attached, the protein elutes at approximately the midpoint of the elution profile for the anion-exchange column. Following this step, the protein sample is dialyzed overnight into gel filtration buffer and concentrated to below 2mL. The sample is loaded into a 2mL superloop and eluted isocratically after loading onto a Superdex 75 (16/60) column (GE). This step is primarily to check for homogeneity of the sample and consistent peak elution off of the column, not as an essential step in protein separation from contaminants.

The fractions containing protein were pooled and concentrated to 30 μ M, aliquotted into 100 μ L fractions and flash frozen in liquid nitrogen before being stored at -80°C.

Chapter 8

Structure Determination and Analysis of the placement of Chloride in the Inactive WNK1 Kinase Domain

8.1 Introduction

As observed in Chapter 7, the WNK1 kinase domain responds to the presence of NaCl by decreasing its kinase activity toward MBP and increasing its midpoint melting temperature as assessed by differential scanning fluorimetry. It was determined by varying the anion and cation composition of different monovalent salts that chloride is the probable inactivating species and, the curve derived from the DSF data fit a one-site binding isotherm. To determine the binding site of the chloride ion, WNK1 194-483 S382A was crystallized in the presence of sodium bromide and data were collected at the bromine anomalous edge at the Advanced Photon Source at Argonne National Laboratories. In this chapter, the structure of the inactive WNK1 kinase domain bound to a chloride ion in the active site is presented. The location of the binding site along the amide backbone in the DFG motif suggests a mechanism of stabilization of the 3.10 helix in the N-terminus of the activation loop. It is postulated that stabilization of the helix acts to occlude glutamic acid 268 on α C from entering the active site to promote catalysis through stabilization of

the catalytic lysine.

8.2 Cocrystallization of WNK1 194-483 S382A, in sodium bromide

8.2.1 Expression

The construct used for determining the site of chloride binding in the inactive kinase domain of WNK1 (194-483 S382A) was expressed and purified as described by Min et al (2004). Briefly, Rosetta (Novagen) *E. coli* were transformed with pHis-parallel plasmid containing WNK1 194-483 S382A. A single colony was selected from an agar plate containing Luria broth, ampicillin, and chloramphenicol, and bacteria were grown as discussed in Chapter 5. Bacterial cultures were pelleted by centrifugation at 4000 rpm for 30 minutes at 4°C and then resuspended in 5mL per liter of bacterial culture in 50mM Tris pH=8.0, 300mM NaCl and 20mM imidazole. Resuspended pellets were flash frozen in $N_2(l)$, and stored at -80°C.

8.2.2 Purification of WNK1 194-483 S382A

Purification of the inactive kinase domain was accomplished by applying the soluble fraction of the homogenized bacterial lysate to a Ni-sepharose IMAC column (GE) and eluted using a linear gradient (100%B=250 mM imidazole). Fractions containing the protein were dialyzed overnight into 50 mM Tris pH=8.0, 50 mM NaCl, 1 mM EDTA, and 1 mM DTT in the presence of

a 1:20 mass ratio of TEV protease. The products of this reaction were passed over a 2mL Ni-agarose column to remove the protease, the cleaved His-tag product, and any uncleaved His-tagged protein. The collected fractions were concentrated to less than 10 mL and loaded onto a MonoQ quaternary amine column (GE). The protein was eluted using a gradient with a final concentration of 500 mM NaCl. Finally, the protein sample was dialyzed a second time into 50 mM HEPES pH=8.0, 100 mM NaCl and 1mM DTT overnight at 4°C. Following dialysis, the sample was applied to a Superdex 75 16/60 column (GE) and isocratically eluted using the previously described buffer. The peak containing the protein sample was concentrated to 8 mg/mL and aliquotted into 100 μ L and flash frozen in $N_2(l)$. Fractions were stored at -80°C until they were used for crystallization trials.

8.2.3 Crystallization of WNK1 194-483 S382 in NaBr

Purified WNK1 194-483 S382A was thawed on ice and centrifuged at 13,000 rpm for 5 minutes to remove any precipitated protein, and to degas the sample. Crystallization trays were set up using a variant of the condition used by Min et al (2004). A mixture of 24% w/v PEG 2000 monomethyl ether, 100 mM HEPES pH=8.0, 300 mM NaBr was used to set up Nextal hanging drop vapor diffusion crystal trays (Qiagen). Sodium bromide was substituted for sodium chloride so that the anion-binding site could be detected by measuring anomalous scattering at the bromine X-ray absorption edge (0.92 Å). Crystal trays were set up using a 1 to 1 (2 μ L) ratio of protein to precipitant solution

per droplet.

After 2 days, macroscopically twinned crystals were observed and grew to 200 μm in size after one week of incubation. A Seed Bead (Hampton) was used to homogenize crystals for micro-seeding experiments using dilutions of 1:10 to 1:10,000 in order-of-magnitude increments. Micro-seeding resulted in continued growth of macroscopically twinned crystals that were not amenable to data collection. To generate single crystals, streak-seeding was used in combination with very long incubation times. Large crystals were chosen and were perturbed with a crystal probe (Hampton) on the face of the crystal that did not contain multiple lattices. The probe was used to streak 3 separate droplets per perturbation of the crystal. Following streak-seeding the trays incubated at 16°C. Although crystals did not appear in the first few weeks of incubation, crystals were discovered in the plates one year later. Five crystals from these plates were cryoprotected using the method described in Chapter 5 in 20% glycerol, 24% PEG 2000 MME, 100 mM HEPES pH=8.0, 300 mM NaBr. Following cryoprotection, samples mounted on robotic pins were plunged into 800mL of $\text{N}_2(l)$ and capped.

8.3 Data Collection

Crystals of WNK1 194-483 S382A were shipped to the Advanced Photon Source at Argonne National Laboratory in Argonne, IL and data were collected at the 19-ID hutch using remote data collection with use of an AC-TOR robotic arm to manipulate crystal mounting and dismounting from the

goniometer. A total of five crystals were shipped to be tested, and two of the crystals yielded diffraction of 2.8 Å, where the signal to noise (I/σ_I) was greater than 2 in the final resolution bin. For the crystal that was used to determine the placement of bromide/chloride in the structure of the inactivated WNK1 kinase domain, 350° of data were collected with an oscillation range of 0.5° using a wavelength of 0.9202 Å. Three seconds of diffraction data were collected per image with an attenuation of 9.11 and the image detector set at a distance of 351.66 mm (equivalent to diffraction at the corner of the detector corresponding to 2.2 Å Figure 6.1) . The data were integrated and scaled in the $P 1 2_1 1$ space group using Denzo and Scalepack integrated in the HKL2000 software package (Otwinowski and Minor, 1997). The space group of $P 1 2_1 1$ was chosen due to the observation of systematic absences along $0k0$ in the reciprocal lattice.

8.3.1 Map Calculation and Refinement

The structure of Br-soaked inactive WNK1 kinase (194-483 S382A) was solved by molecular replacement utilizing the A subunit from the inactive kinase domain (Min et al, 2004) (PDB: 3FPQ) by implementing molrep in the CCP4 program suite (Collaborative Computational Project, 1994). A single round of refinement using Refmac5 was used prior to exporting to PHENIX for further refinement. During the subsequent rounds of refinement, a combination of TLS and restrained refinement against the previously solved inactive structure was utilized. The anomalous difference fourier map was used to

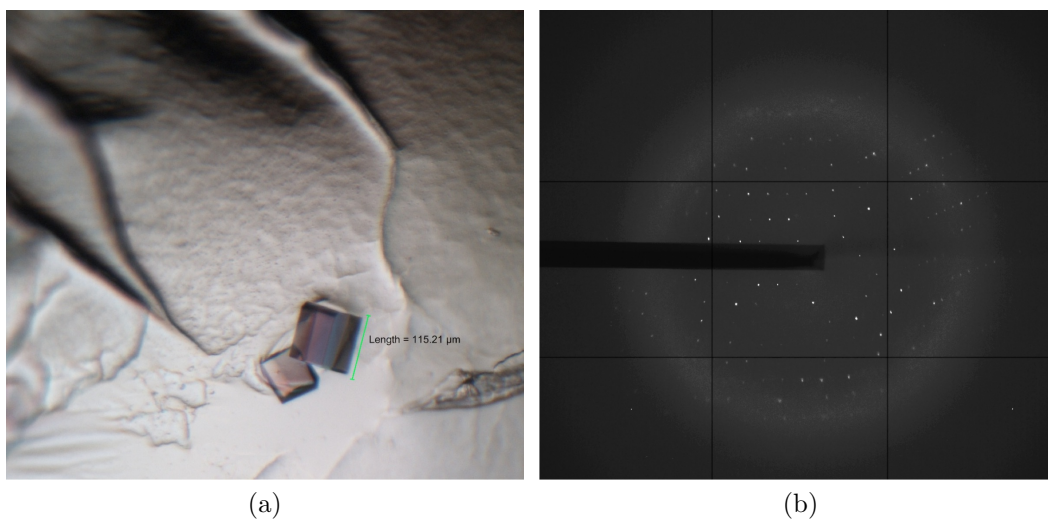


Figure 8.1: a) Diffraction Pattern for WNK1 194-483 S382A b) Crystals of WNK1 194-483 S382A grown in the presence of 300mM NaBr

confirm identify the positions of any bound bromide ions. The anomalous difference fourier map was created using the CAD program in CCP4 to merge the *mtz* file generated following scaling and the *mtz* file following a round of refinement (All columns on the former file were merged with FC, PHIC and FOM columns from the post-refinement *mtz*). Since the anomalous peak for bromide was present at only 5.2σ , suggesting low occupancy, chloride was used in subsequent refinement steps. The final refinement occupancy for the chloride ion is 86%. Following refinement, the statistics for the model of the activated WNK1 kinase are presented in 8.1.

Table 8.1: Data collection and Refinement Statistics for WNK1 (194-483 S382A)

Space Group	P 1 2 ₁ 1
Unit Cell	a=38.01 Å, b=58.30 Å, c=65.04 Å $\alpha=90^\circ$, $\beta=91.35^\circ$, $\gamma=90^\circ$
Resolution (Å)	43.41-2.82 (2.85-2.82)
Observed Reflections	47,703
Unique Reflections	6,887
Completeness	98.8 (96.1)
I/ σ_I	44.3 (4.3)
Redundancy	6.9 (6.6)
R _{work} (%) [‡]	22.5
R _{free} (%)	30.6
Number of groups	
Protein Atoms	1950
Water	16
RMSD	
Bond Length, Å	0.009
Bond Angle, °	1.23
Average B factor, Å ²	108.6
<i>Ramachandran Map (%)</i>	
Favorable	95.7
Allowed	3.9
Disallowed	0.4

[†] Values in Parentheses indicate the highest resolution shell

[‡] R_{work} = $\sum ||F_{obs} - F_{calc}|| / \sum |F_{obs}|$, where F_{obs} and F_{calc} are the observed and calculated structure factors, respectively.

8.4 Structure of the mutant, inactive WNK1 kinase domain bound to Bromide

The structure of the mutant inactive kinase domain cocrystallized in the presence of sodium bromide is similar to that of the structure determined by Min *et al*, but contains many regions of disorder in the N-terminus and in the activation loop. Although the space group is $P 1 2_1 1$, as evinced by systematic absences along $(0 k 0)$, there are interactions between the activation loop and the N-terminal β strands in the adjacent asymmetric unit, as observed in a similar manner reported by Min *et al* for the structure solved in the $P 1$ space group. As discussed in Chapter 1, the structure reported by Min, *et al* contains two distinct subunits with markedly different N-terminal regions and activation loop structures (Figure 1.4a).

The structure that is reported here contains 7 disordered regions in the N-terminus as well as in the activation loop after S378. Specifically, residues 230-233, 242, 252-258, 293-294, 297, 379-380, and 384-387 lack sufficient density to be modeled. Although there is a considerable amount of disorder in the N-terminus, the 2.8 Å structure of the kinase domain cocrystallized with sodium bromide has a low RMSD of C_α positions (all atom 0.31 Å) relative to subunit A in the inactive WNK1 structure described by Min *et al* (2004).

Of interest is the presence in the WNK1 structure of a 3.10 helix, which is initiated at the glycine of the DFG motif in the N-terminus of the activation loop. When the anomalous difference fourier map for peaks corresponding to the presence of bromine is calculated, there is a 5.2 σ peak that

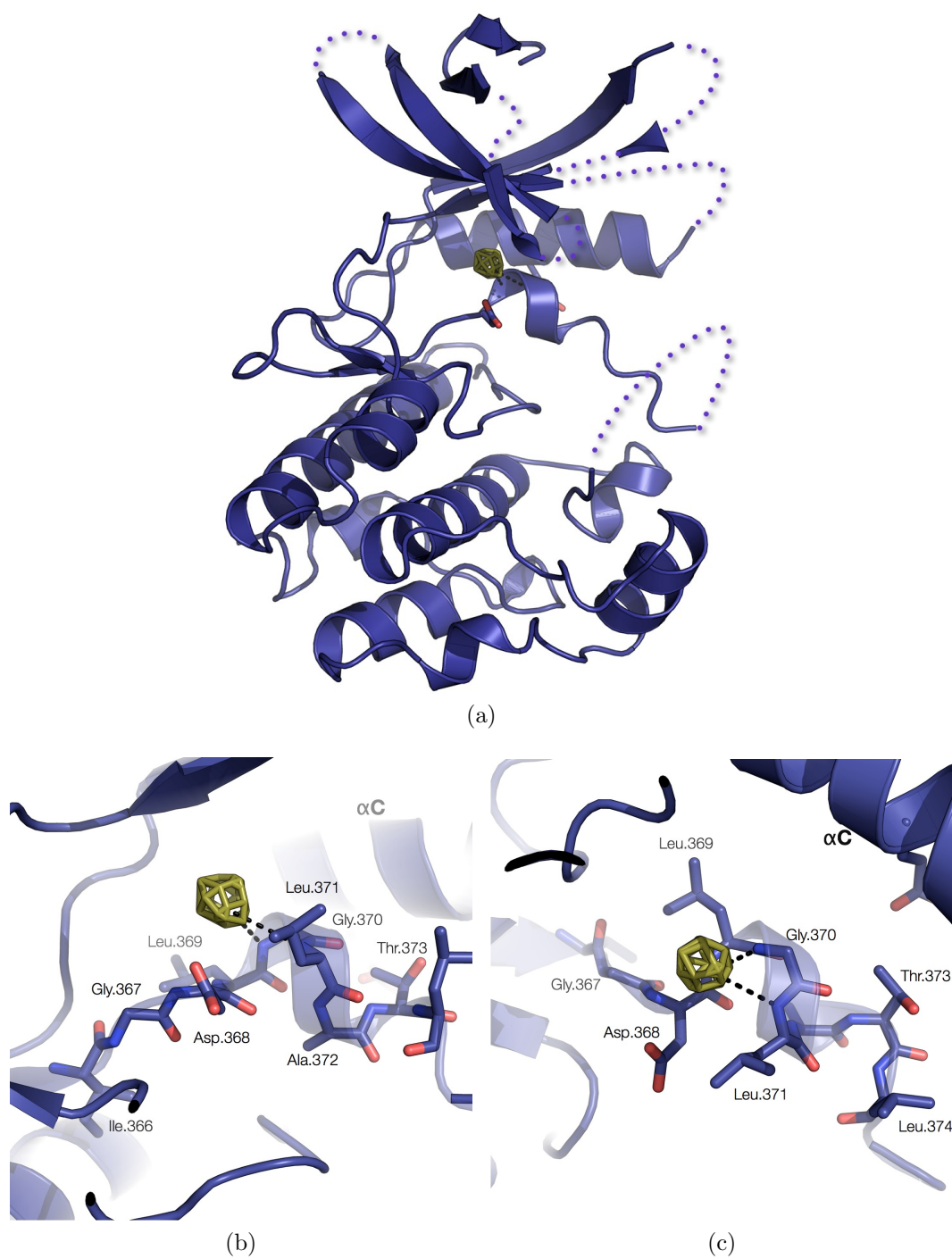
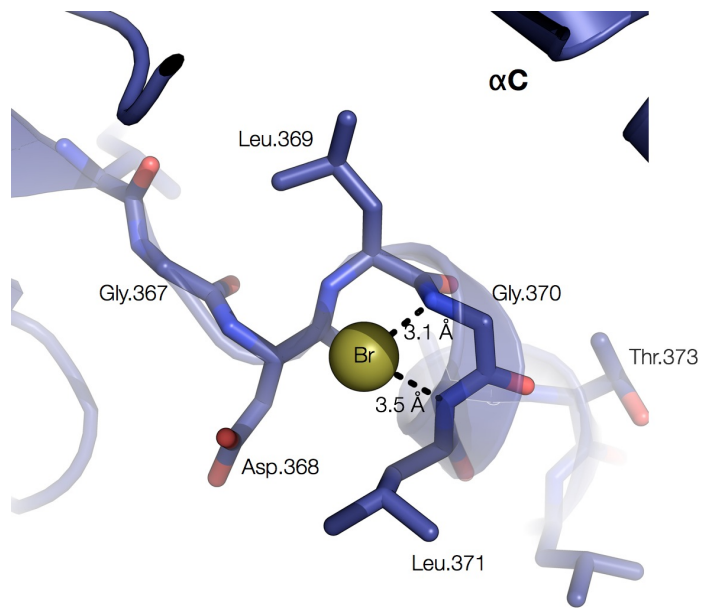


Figure 8.2: a) Crystal structure of WNK1 194-483 S382A cocrystallized in 300 mM NaBr. b,c) View of the anomalous difference fourier map (chartreuse) contoured at 3.5σ showing its position with respect to the DLG motif and the 3.10 helix present in the activation loop

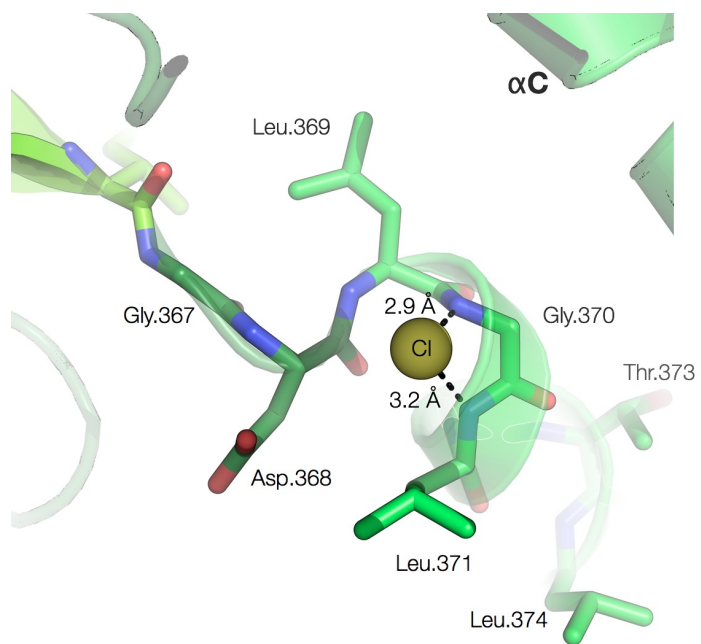
lies directly adjacent to the backbone at the DGF glycine (Gly 370) as seen in Figure 8.2. This signal is the most intense peak in the anomalous map, with the next largest peak being found at a 3.5σ contour. The relatively weak signal found in the anomalous data is a concern, but may be explained as part of a byproduct of the purification methods.

When the kinsae domain was purified by size-exclusion chromatography, a buffer of 50 mM HEPES pH=8.0 and 100 mM NaCl was used for isocratic elution. When the concentrated protein was mixed with an equal volume of precipitant solution containing 300 mM NaBr, it would be expected that nearly half of the population of protein in solution was bound to a chloride ion ($IC_{50}=130\text{mM}$). This suggests incomplete incorporation of bromide ion into the binding site due to competition from smaller chloride ions already present in solution prior to crystallography.

As shown in Figure 8.2, an ion at the center of the observed anomalous difference fourier peak may interact with the peptide backbone between residues Gly 370 and Leu 371. The hydrogen bonding distances between the ion and the amide backbone are 3.1 and 3.5 Å for residue 370 and 371 respectively. To corroborate this evidence of anomalous X-ray scattering, an atom labeled as water is observed making similar contacts to the amide backbone corresponding to residues Gly 370 and Leu 371 in the structure of subunit A determined by Min et al (2004). When the $2mF_o - DF_c$ map is calculated for this area, the "water" molecule interacting with the backbone has a 5.5σ peak intensity. To put this into perspective, the only atoms that retain density at that

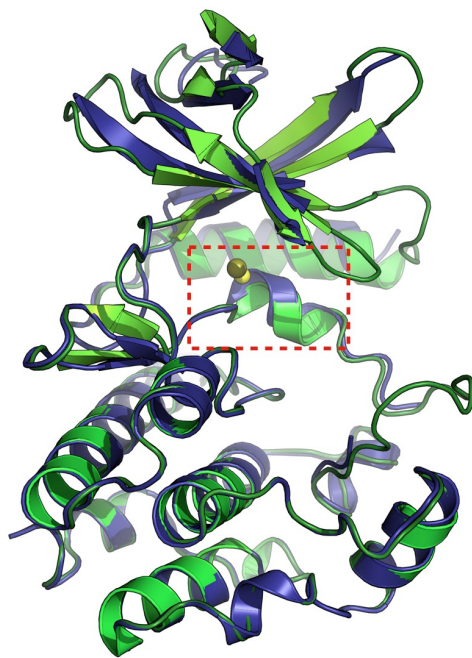


(a)

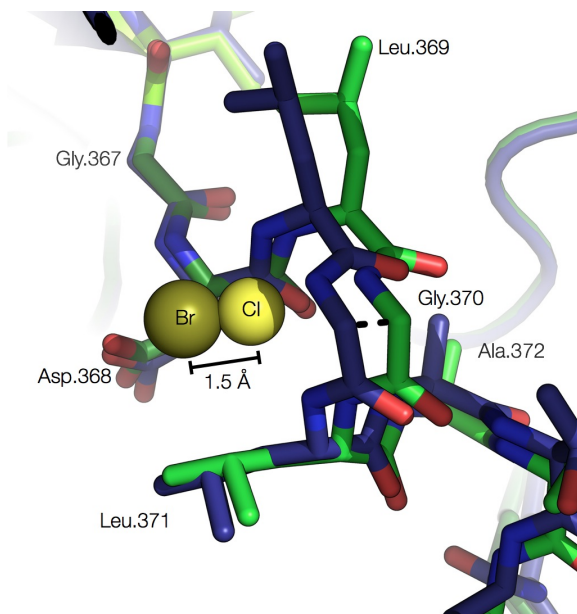


(b)

Figure 8.3: Comparison of the binding sites of the a) bromide-cocrystallized WNK1 kinase domain (purple) and b) the chloride-cocrystallized WNK1 kinase domain (green) originally reported by Min et al (2004)



(a)



(b)

Figure 8.4: a) An all-atom alignment (residues 309-483) of the bromide (purple) and chloride-cocrystallized (green) WNK1 kinase domains. b) The backbone of the 3.10 helix formed by halide binding is shifted by 1.5 Å from the chloride to the bromide-cocrystallized structures and is reflected in the respective placement of the halide in each structure.

level are sulfur from cysteine, the selenium from selenomethionine, and select backbone carbonyls. Notably, all of these species are electron rich. Because of this fact, the observed anomalous density observed for the 2.8 Å structure we have reassigned this as a chloride ion. The structure originally solved by Min et al (2004) was refined in PHENIX using chloride as a replacement for the electron-dense water observed near the N-terminus of the 3.10 helix. Prior to refinement, the water was identified as a B-factor outlier with a temperature factor of 14.4 Å² (average B for the structure is 25.2 Å²). When chloride was refined (occupancy, real-space, xyz, and individual B-factors), the temperature factor for that atom increased to 28 Å² (Average B for structure 26.2 Å²), and the peak for the chloride ion in the $2mF_o - DF_c$ map increased to 5.7 σ with a final occupancy refinement of 100 %. The final R_{work} and R_{free} for the refined structure were, essentially unchanged with values of 18.9 % and 22.4 %, respectively.

The interaction of this chloride with the backbone consists of similar contact distances as can be seen in Figure 8.3. When the two structures are aligned, a 1.5 Å perturbation is observed between the backbone of the bromide-containing structure and the native structure solved by Min *et al.* Associated with this shift in the protein backbone is a concomitant shift in the location of the Br⁻/Cl⁻ site of equal magnitude (Figure 8.4).

8.5 Discussion

The structure of the bromide-bound inactive WNK1 kinase domain was determined at 2.8 Å resolution and displays an anomalous difference fourier peak corresponding to the location of a bromide ion located at the N-terminus of a 3.10 helix present in the activation loop. The ion makes two contacts to the backbone amides of Gly 370 and Leu 371. A similar phenomenon is observed in subunit A of the inactive kinase domain reported by Min et al (2004). Present in the native structure is a 5.7 σ peak from the $2mF_o - DF_c$ map that mimics the placement of bromide found in the newly reported structure. The 3.10 helix of the native structure also appears to be maintained by contacts made from Gly 370 and Leu 371 to what appears to be a chloride ion.

In contrast, when the structure of the B subunit from Min, *et al* is examined, although there is a half-turn 3.10 helix present near the N-terminus of the activation loop, Gly 370 and Leu 371 are not interacting with a chloride ion or any solvent. Further, the two residues that appear to be necessary in promoting formation of the 3.10 helix by interaction with chloride or bromide ions are not involved in forming the helix. Unlike in subunit A from the Min, *et al* structure, the α C helix and its interaction with T373 appear to be driven by crystal contacts between subunit B and its adjacent unit cell. This interaction may promote the half-turn 3.10 helix in the activation loop even though it does not appear to be bound to a chloride ion (Figure C.1).

In general, the 2.8 Å structure of the bromide-soaked inactive WNK1 kinase domain paired with the discovery of an identical chloride binding site

present in subunit A of the structure solved by Min et al (2004) suggests a mechanism of WNK1 autoinhibition in response to increasing sodium chloride concentration. To fully develop an understanding of how the WNK1 kinase domain is autoinhibited in the presence of sodium chloride, the structures of the chloride and bromide-bound kinase domain can be compared to the structure of the activated WNK1 kinase domain and active, ATP-bound PKA.

When the structure of the A subunit of the inactive WNK1 kinase domain is compared to the activated structure of the WNK1 kinase domain, one observes that the DFG motif lacks secondary structure and the 3.10 helix has been lost. This corresponds to a 2.5 Å shift in Ala 372 away from the catalytic loop as seen in Figure 8.5. It is presumed from the change observed between the structures that, in the absence of chloride ions, the 3.10 helix is lost and the activation loop adopts a conformation more similar to that of an active kinase - such as PKA. In Figure 8.6, the DLG region for the inactive, chloride bound kinase domain and the activated kinase domain are compared to active PKA. It is observed that when the chloride ion is bound to the N-terminus of the 3.10 helix, it promotes hydrogen bonding interactions between Thr 373, R384 and E268 in the WNK1 kinase domain. The latter two residues are necessary for forming a catalytically competent kinase. The glutamate, as discussed previously in Chapter 6, is involved in stabilizing the catalytic lysine (K233). The activated WNK1 kinase domain contains similar elements that are indicative of an active kinase when assessed by comparison with protein kinase A. Although Glu 268 remains outside of the active site, Arg 398 adopts

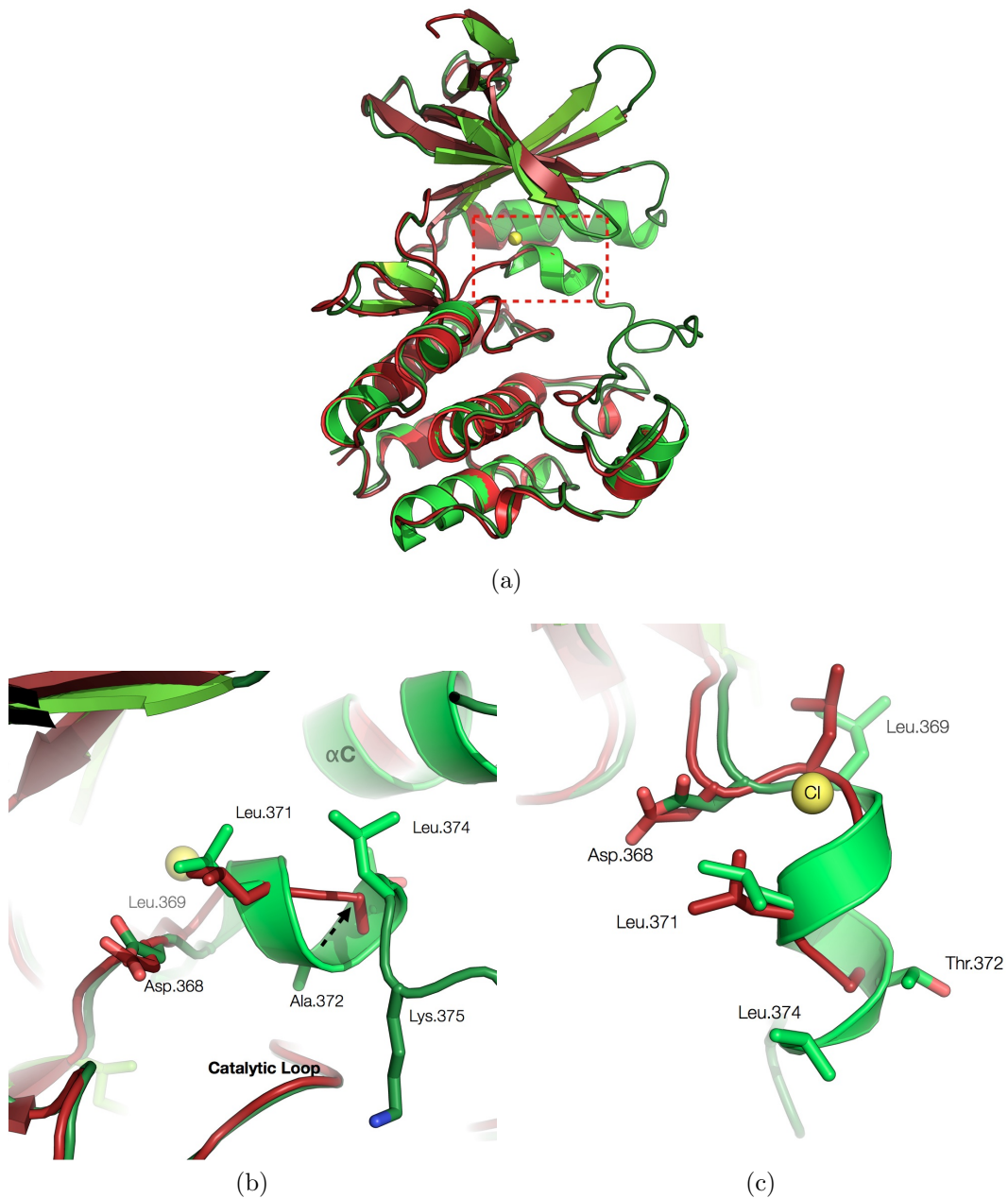


Figure 8.5: a) An all-atom alignment (residues 309-483) of the inactive, chloride bound (green) and the activated (red) WNK1 kinase domain. b,c) A comparison of the DLG chloride binding cleft. The activated, chloride-free structure displays a loop-like structure compared to the 3.10 helix formed by the interaction of amides from G370 and L371 with chloride. The placement of A372 C_{β} in the activated structure is displaced by 2.5 Å.

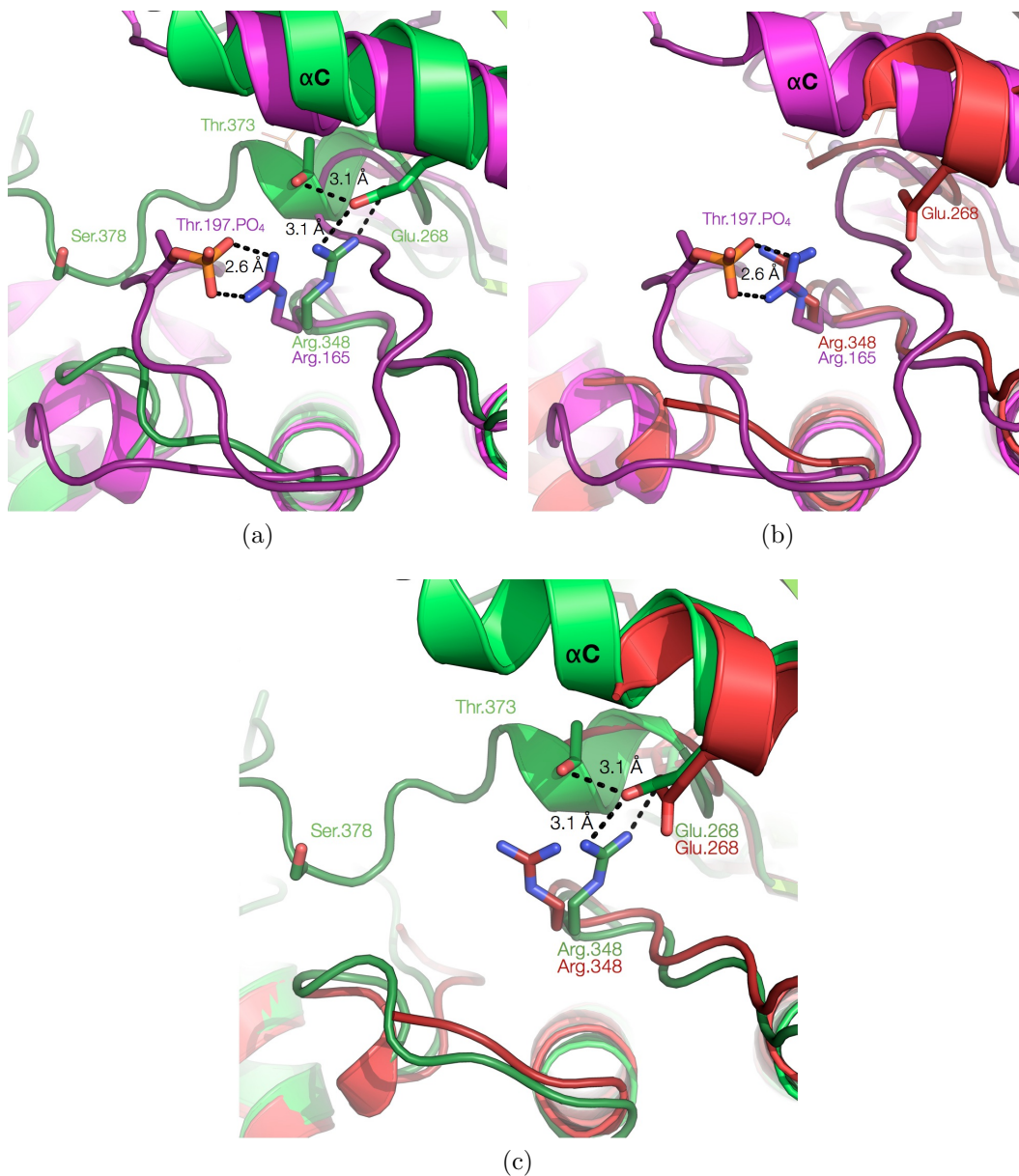


Figure 8.6: a) Comparison of active PKA (magenta, PDB ID: 1PKA) with the chloride-bound, inactive WNK1 kinase domain (green) showing the interaction of R348 through hydrogen bonding with T373 and E268. In PKA, the equivalent arginine (R165) is involved in interactions with a phosphothreonine b) The activated WNK1 kinase (red) adopts a conformation of R348 that is similar to active PKA (magenta). c) A comparison of R348 placement in the chloride-bound (green) and activated (red) WNK1 kinase domain structures showing a 3 Å shift in the placement of the N_ε of R348.

a more active conformation by moving away from its association with Glu 268 observed in the inactive WNK1 kinase structure. Instead it adopts a conformation similar to that observed from Arg 165 in PKA.

The location of the chloride binding site using anomalous X-ray scattering and corroboration of the location of an identical chloride site in the native inactive WNK1 kinase domain structure solved by Min *et al* has been found. From this data and comparison to subunit B from the Min *et al* structure and the previously presented activated WNK1 kinase domain, we have developed an idea of the structural mechanism involving chloride inactivation of the kinase domain. In addition, by pairing this structural information with our biochemical and biophysical findings regarding the salt sensitivity of the kinase, a general framework can be constructed for how cellular systems sense and respond to intracellular levels of salt. The ideas will be presented and discussed further in Chapter 9.

Chapter 9

Discussion

9.1 A mechanism of salt sensing by the WNK1 kinase domain

In the preceding two chapters, the salt sensitivity of the WNK1 kinase domain was analyzed by biochemical and biophysical methods. From the structural analysis of the WNK1 kinase domain in high (>300 mM) and low (10-20 mM) salt environments, and their subsequent comparison to the active form of protein kinase A, we were able to infer the mechanism involved in the activation/inactivation of the WNK1 kinase.

When WNK1 is present in an environment of high concentration of chloride ions, chloride becomes bound to the N-terminus of the activation loop. This binding event promotes the formation of a 3.10 helix through hydrogen bonding interactions of the chloride ion with the backbone amides for Gly 370 and Leu 371. The formation of this helix acts as not only a barrier to the entry of Glu 268 into the active site, but promotes the formation of hydrogen bonding between Thr 373 and Arg 348. By stabilizing this interaction, the 3.10 helix aids in the sequestration of the residues that are necessary for catalytic activity of the kinase - Glu 268 which is involved in stabilizing the catalytic lysine during the phosphotransfer reaction, and Arg 348, which interacts with

a phosphorylated residue in the activation loop.

When chloride concentrations drop and there is a release of chloride from the 3.10 helix the helix undergoes a loss of secondary structure; which, in turn, destabilizes the interaction between Thr 373, Glu 268 and Arg 348. This allows the arginine to adopt a conformation indicative of an active kinase. However, we observe that the placement of Glu 268 remains outside of the active site in the activated WNK1 structure. We hypothesize that during the ATP and Mg^{2+} binding event, Glu 268 responds by entering the active site and associating with the catalytic lysine by an "induced fit" mechanism. This hypothesis will need to be confirmed by crystallization of WNK1 in low salt in the presence of AMP-PNP or ATP and Mg^{2+} in addition to ATP affinity being assessed in the presence of increasing concentration of sodium chloride.

9.2 The chloride ion sensor WNK1 acts as a negative feedback loop regulator in cells

To corroborate the our findings that WNK1 is inactivated by chloride ions and suggest that the WNK kinase domain may act as the cellular salt sensor for eukaryotes, three central papers regarding the activity of WNK1 in relation to cystic fibrosis transmembrane conductance regulator (CFTR) and sodium, potassium, 2 chloride cotransporters (NKCCs) will be considered. In report presented by Yang et al (2007), WNK1 inactivated CFTR conductance over time and in a kinase-dependent fashion. CFTR is an ABC transmembrane transporter that relies on cAMP and ATP to catalyse the conductance of chlo-

ride ions across the plasma membrane from the cytoplasm to the extracellular space (Guggino and Stanton, 2006). Misfolding or inhibition of this protein in humans causes cystic fibrosis, which is characterized by the buildup of thick mucous in polarized epithelia. Inhibition of this protein by phosphorylation may occur, and WNK1 appears to modulate its activity through this mechanism (Yang et al, 2007). The authors report that when CFTR is activated by isoproterenol and 3-isobutyl-1-methylxanthine, conductance of chloride levels across the membrane in *Xenopus* oocytes is unabated. However, when WNK1 is coexpressed in the oocytes, CFTR conductance is repressed after the initial jump in chloride conductance. This is consistent with our biophysical findings and suggests that WNK1 responds to the decrease in chloride ion concentration by inhibiting CFTR function through phosphorylation.

In a report by Moriguchi et al (2005), the *in vitro* and *in vivo* activity of WNK1 on SPAK or NCC substrates was monitored using either isotonic (135 mM NaCl) or hypotonic (65 mM Na-gluconate) buffers. For the *in vitro* experiments, WNK1 was immunoprecipitated from endogenous HEK 293 cells and incubated with a fragment of the WNK1 substrate, SPAK (348-553) in either isotonic or hypotonic chloride buffer. A time-course assay measuring ³²P-incorporation into the substrate was monitored over 60 minutes. The authors observed a lack of incorporation of radio-labeled phosphate into SPAK when incubated in the isotonic media. However, when incubated in low-Cl⁻ buffer, the incorporation of radio-labeled phosphate was dramatically increased.

A similar experiment examining *in vivo* radio-labeling of NCC was con-

ducted with similar effects. HEK 293 cells were transfected with NCC containing a T7 epitope tag. Following transfection, cells were metabolically labeled with ^{32}P and allowed to incubate for 6 hours before being exposed to isotonic or hypotonic chloride buffers. When the NCC protein was immunoprecipitated using an antibody specific to the T7 epitope, the authors observed a dramatic increase in the amount of radio-labeled phosphate incorporated into the NCC in hypotonic media compared to that of the isotonic (135 mM NaCl) buffer Moriguchi et al (2005).

Finally, a more recent report by Ponce-Coria et al (2008) suggests that WNK3 may be involved in regulation of NKCC2 via a chloride-sensing mechanism. The authors report that, under hypotonic conditions, WNK3 increases the activity of NKCC2, allowing for an increase in ^{22}Na uptake as well as phosphorylation of NKCC2. The authors show a reduced sensitivity of WNK3 activation of NKCC2 under isotonic (92 mM NaCl) conditions. Although the authors show that inhibition of kinase activity in WNK3 D294A and mutation of the C-terminal RFXV motif decreases the uptake of ^{22}Na by NKCC2, a mechanism for how chloride may be sensed by the WNK3 kinase is not proposed.

9.2.1 How WNK1 may act to control chloride levels in cellular environments

In the human kidney, salt reabsorption is controlled through cells present in the distal convoluted tubule. This process is mediated by the import of sodium, potassium, and chloride ions (via an electroneutral mechanism) into

DCT cells under control by the cascade comprising the WNK1 kinase and its activation of the Sterile-20 kinases OSR and SPAK (Moriguchi et al, 2005). The export of chloride and sodium into the blood is controlled by a voltage-gated mechanism where a potential difference across the membrane is maintained by the Na^+/K^+ -ATPase and is utilized by the ClC-KB voltage-gated chloride transporter to ferry chloride anions out of the cell (Kramer et al, 2008). In kidney and many other cell types, isotonic chloride levels are maintained near a range of 90-150 mM (Cook and Macknight, 1984; Macknight, 1985; Gedde et al, 1997). This average value lies near the IC_{50} measured for the inhibition of WNK1 by chloride ions (130 mM) and succinctly explains the maintenance of cellular levels of chloride in this range.

There are two commonly reported values for the concentration of intracellular chloride. First, the concentration of intracellular chloride have recently been measured using fluorescence-based assays. These reports have described levels of chloride in the range of 5-50 mM for varying cell types (Achilles et al, 2007; Wöll et al, 1996). However, a report describing the *in vitro* addition of chloride to these methoxylquinolyl-based fluorophores described a K_d of 13 mM (Marandi et al, 2002). This would make the effective chloride measurement range for the fluorophore between 0 and 50 mM. Moreover, the authors note that when the fluorophore is transfected into cells, the apparent K_d for chloride binding is shifted to 40 mM. Notably, the initial description of these fluorescence-based indicators describe the inherent inconsistency between cell preparations and suggest that standard curves (utilizing ionophores to intro-

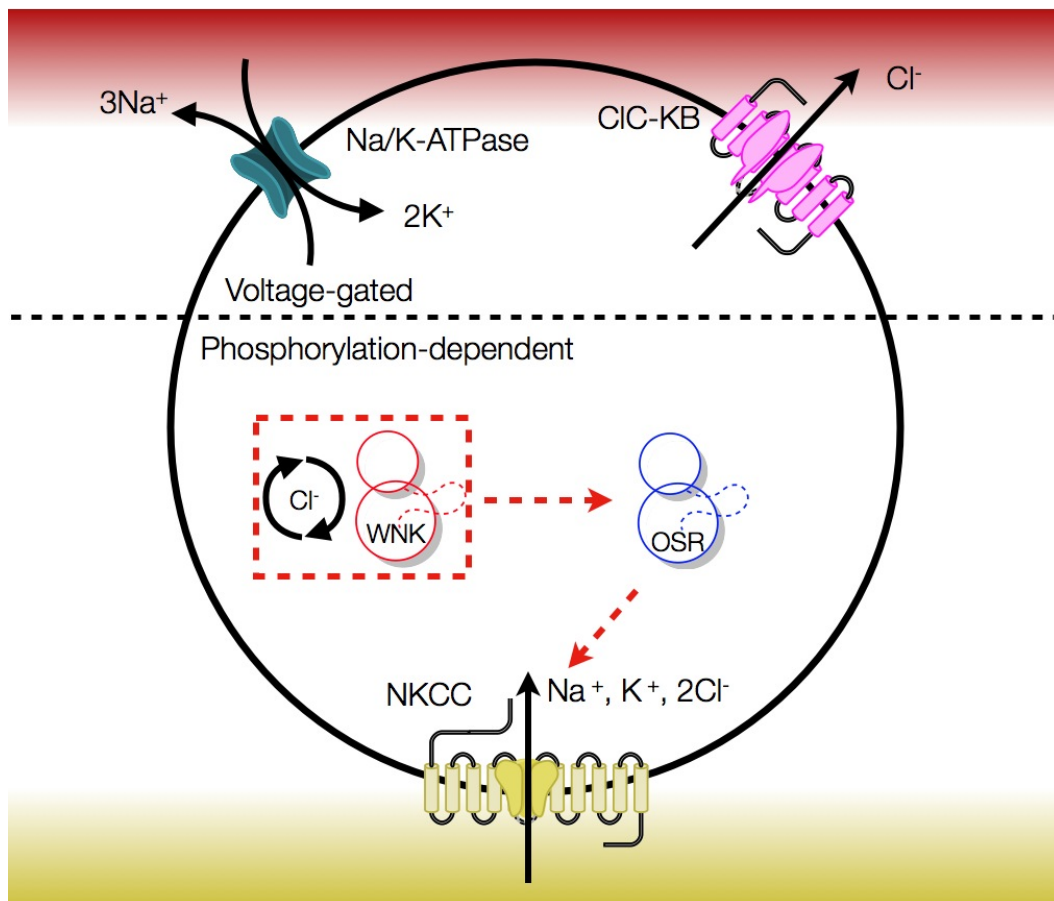


Figure 9.1: Proposed mechanism of cell volume regulation by the putative chloride sensor, WNK1. Cells in the distal convoluted tubule act to reabsorb salt from the urinary lumen (yellow) into the blood (red) to help maintain ion homeostasis (Richardson and Alessi, 2008). Based upon data outlined in Chapters 7 and 8, we propose a mechanism by which WNK1 activity modulates ion reabsorption. WNK1 kinase activity is affected by the concentration of chloride ions and undergoes a structural change upon chloride binding which renders the kinase inactive. In a simplified mechanism, the presence of a low chloride environment would serve to activate WNK1. This, in turn, activates the CCCs via OSR/SPAK, allowing for the import of sodium, potassium and chloride from the urinary lumen. As chloride levels rise, WNK1 activity is inhibited and the input signal is attenuated. Chloride export from the cell is driven via a voltage-gated mechanism linked to the Na/K-ATPase.

duce free chloride) for independent cell preparations be made.

Conversely, methods utilizing the incubation of cells with ^{36}Cl or measurement of chloride levels by argentometry (titration into a solution of silver nitrate) have reported concentration of chloride distributed near 100 mM (Cook and Macknight, 1984; Gedde et al, 1997). The use of these analytical methods are much less prone to interference by interactions with cellular constituents that may quench fluorescent dyes that associate with chloride ions such as gluconate, thiocyanate, and other halides (Inglefield and Schwartz-Bloom, 1999). Moreover, the results from radiometric or titrimetric measurements are more consistent and do not require repeated calibration from individual experiments.

The resulting mechanism for chloride ion sensing in kidney cells based upon the data presented in this thesis and the data gathered from the literature surrounding WNK1 is presented graphically in Figure 9.1. In the presence of low intracellular chloride content, WNK1 autophosphorylates and activates the NKCCs via the OSR/SPAK kinases. The NKCCs then pump Na^+ , K^+ and 2Cl^- across the membrane until an isotonic chloride concentration is met. WNK1 activity is then mitigated by the binding of chloride to the active site of WNK1, thus promoting the isolation of the key catalytic residues necessary for forming a catalytically competent kinase. We speculate that phosphatases would intervene to dephosphorylate OSR/SPAK and the NKCCs at some point to terminate the input signal. Chloride would then be pumped out by the Cl^- channel mediated by a voltage-gated mechanism linked to activity of the

Na⁺/K⁺-ATPase. This cellular mechanism for WNK1 activity mediated by chloride ion sensing allows for the cell to operate in hypotonic or hypertonic chloride environments. If the cell takes in too much chloride or is located in an environment of abundant chloride ions, WNK1 activity would remain low; whereas, if extracellular chloride is low, the WNK1 activity would remain high in order to import any available salt into the cell and maintain isotonic conditions.

The presence of multiple phosphorylation sites, poly-proline and RFXV motifs, as well as large regions of predicted disorder in the WNK1 protein kinase indicate that the activation of the WNK1 kinase is complex (Richardson and Alessi, 2008). This is reflected by initial investigations of the kinase where it appears to be activated in both hypertonic and hypotonic salt conditions (Lenertz et al, 2005), and is corroborated by studies of the NKCCs which demonstrated activation in an environment of high osmotic stress (Anselmo et al, 2006). Due to these observations of apparent WNK1 activation under hypertonic conditions, more investigation as to the mechanism of WNK1 activity in these conditions is merited in extended constructs not limited to the kinase domain.

9.3 Inhibition by the WNK1 autoinhibitory domain may be linked to the salt sensitivity of the kinase domain

Xu et al (2002) reported the inhibition of the WNK1 kinase domain by its autoinhibitory domain both *in cis* and *in trans*. However, as it was reported

in Chapter 2 and 4, the construct used by Xu *et al* (485-555) excluded the first β strand and the terminal α helix. These two elements were explicitly discussed and are critical in forming a folded and stable domain. It is unknown if the 485-555 construct used by Xu *et al* was affected by the exclusion of these elements.

When the construct was extended to include residues 480-572, an *in cis* titration of the autoinhibitory domain into the kinase domain in a low-salt buffer showed no appreciable inhibition of kinase activity. When the titration curves of different peptides into the autoinhibitory domain using different lengths of RFXV motifs derived from two different areas of the kinase were examined, we found that a dodecameric peptide derived from α D and α E in the kinase domain bound four times more tightly than a peptide derived from a region in the C-terminus with unknown composition of secondary structure elements. The dodecameric peptide was also found to bind tighter than the pentameric peptide by an order of magnitude. From this, it was inferred that, although we do not see an *in trans* inhibitory effect on kinase activity, it may be possible for the autoinhibitory domain to associate with the kinase domain via an *in cis* mechanism.

To test this, a construct consisting of residues 194-573 was expressed and purified in a fashion similar to what was described in Chapters 2 and 5. The following separation by MonoQ, the protein was concentrated in the presence of 10mM HEPES pH=8.0 and 10mM NaCl as a buffer to 5 mg/mL. At this point, it was observed that a white precipitate had formed in the cen-

trifuge vial (10,000 MWCO) used to concentrate the protein. The solution was centrifuged for 5 min at 13,000 rpm to pellet the insoluble fraction and the remaining soluble protein was run isocratically on a Superdex 75 16/60 size exclusion column (GE). There were two peaks observed in the chromatogram with elution volumes of 45.8 mL (void) and 50.33 mL. The latter elution volume corresponds to a species which matches the expected molecular weight of the tethered kinase and autoinhibitory domains (~ 45 kDa). The protein was collected following SDS-PAGE analysis.

An attempt to further concentrate the protein solution for crystallography was made. Upon concentrating the protein to higher than 5 mg/mL, precipitation was again observed. The protein with precipitate was resuspended and transferred to a 15 mL Falcon tube (BD) where a solution of 5 M NaCl was used to bring the NaCl concentration to 100 mM. The solution was vortexed briefly to mix the solution. During the vortexing, the precipitate returned to a colorless solution. The size-exclusion column was equilibrated with 10mM HEPES pH=8.0 and 100mM NaCl and the protein was isocratically eluted. The observed elution volume was recorded at 56.6 mL, which is similar to what is observed for the independently expressed kinase domain (Figure D.1a). The protein was subjected to proteolysis by trypsin and analyzed for phosphorylation state. The phosphorylation of Ser 382 was detected, but not Ser 378.

In an attempt to make a more homogeneous protein, Ser 378 was mutated to alanine and expressed in the same length of construct. The protein

was treated similarly as above; however, the protein was not concentrated to induce precipitation, but to 3 mg/mL for the 10mM NaCl sample and 5 mg/mL for the 100 mM NaCl sample (each sample contained 10 mM HEPES pH=8.0). An analytical size-exclusion column was used (Superdex 75 10/100 (GE)) to test each following dialysis into the respective buffer. As seen in Figure D.1b, the intermediate phosphorylation mutant displays a similar shift in elution volume. Although this phenomenon needs to be more thoroughly investigated, a working hypothesis for WNK1 autoinhibition by its autoinhibitory domain is presented in Figure 9.2. In this model, the autoinhibitory domain associates with the monophosphorylated WNK1 intermediate under high salt conditions. These are operating under similar conditions to the chloride ion promotion of 3.10 helix formation in the N-terminus of the activation loop. When the salt concentration lowers to approximately 10 mM, the WNK1 autoinhibitory domain dissociates from the kinase domain and allows for full WNK1 activation through autophosphorylation of Ser 378. I hypothesize that there may be an allosteric link between chloride binding and WNK1 autoinhibitory domain association with the kinase domain. The investigation to whether or not the autoinhibitory domain is binding to the RFXV motif location between α helices D and E should be investigated more thoroughly; but, the inhibition of the kinase domain by chloride ion does not fully depend on autoinhibitory domain binding. Further, when chloride inhibits the WNK1 kinase domain, there is some activity (\sim 20-30%) toward MBP. I think that the function of the autoinhibitory domain is to fully block the entry of ATP into the binding

site and fully suppress activity of the kinase.

The kinase activity of WNK1 appears to be regulated by three processes: autophosphorylation, chloride binding and autoinhibition. Based upon the findings presented, these three mechanisms appear to operate on a synergistic level to attenuate kinase activity. Although autophosphorylation of the kinase can occur, chloride binding to the DLG motif in the activation loop appears to act as a rheostat and appears to operate independent of kinase autophosphorylation. It remains to be seen whether the presence of increasing chloride concentrations can attenuate autophosphorylation. Further, initial investigations of the *in cis* construct of the WNK1 kinase and autoinhibitory domains (194-573) appear to demonstrate an allosteric linkage between salt increasing salt concentrations and autoinhibitory domain binding. By investigating the phosphorylation state of the kinase when these transitions between bound and unbound states are observed, we find that an intermediate phosphorylation state (S382*) may be a necessity for autoinhibitory domain binding to the kinase domain. Although these processes and their interplay need to be investigated further, it is clear that the three regulatory mechanisms are acting in concert to manage WNK1 activity.

9.4 Future directions for investigation of the WNK family of protein kinases

To further investigate the chloride sensitivity of WNK1 and the *in vitro* and *in vivo* effects that the kinase may have on substrates and autophospho-

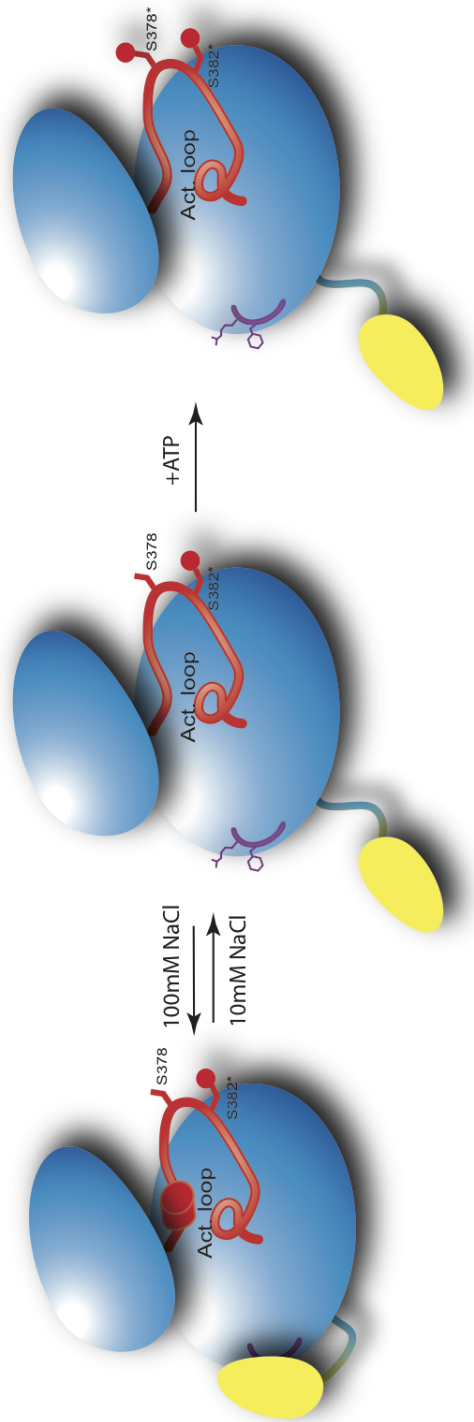


Figure 9.2: Model of allosteric linkage of the autoinhibitory domain to the kinase domain under the control of sodium chloride concentration. In the presence of elevated chloride ion concentrations, the 3.10 helix is formed in the N-terminus of the activation loop and the autoinhibitory domain is bound to the RFXV motif present between $\alpha D/E$ in the kinase domain. When chloride concentrations lower, the 3.10 helix dissolves and the autoinhibitory domain is released from the kinase domain. The presence of ATP promotes full activation of the kinase domain, although we predict that the introduction of chloride ions would inhibit kinase activity independent of the autoinhibitory domain.

rylation, a number of experiments and long-term goals need to be addressed.

9.4.1 Short-term goals addressing the chloride-sensitivity of the WNK1 kinase domain

Four experiments are needed to address the chloride sensitivity of the kinase domain. The WNK1 protein kinase shares over 95% homology to the other three homologues of WNK in the kinase domain (Min, 2004). These protein kinases share a conserved DLG motif in the N-terminus of their activation loops. From the analysis of the chloride-binding site in the WNK1 kinase, I expect for the other WNK kinase domains to behave similarly to that of that of WNK1. In addition, mutation of either Leu 369 and/or Leu 371 to phenylalanine may abolish the chloride-sensitivity of the domain ¹.

The chloride-sensitivity of WNK1 kinase domain autophosphorylation will also need to be assayed. Briefly, WNK1 (194-483) will be expressed in *E. coli* and then dephosphorylated using the shrimp alkaline (serine) phosphatase. Dephosphorylation of the kinase domain at S382 and S378 will be monitored by mass spectrometry. WNK1 autophosphorylation will be tracked by radiometric labeling of ATP in the presence of increasing chloride concentration.

Finally, crystallization of the WNK1 protein kinase in the presence of ATP (or ATP analogs) and magnesium should be examined. Crystals of phosphorylated WNK1 (209-483) in a low salt environment (25 mM) in the presence

¹Upon publication of this thesis, differential scanning fluorimetry of WNK1 194-483 L369F will have been conducted

of 10 mol. equivalences of AMP-PNP and magnesium sulfate have been grown in 19 % PEG 3350 and 0.3 M KH_2PO_4 . These crystals exhibit macroscopic twinning and need to be further optimized to generate single crystals amenable for data collection.

9.4.2 Long-term goals

Thus far, the investigation of the *in cis* mechanism of autoinhibition of the WNK1 kinase domain with its autoinhibitory domain has been limited to an observation of changes in elution volume from a gel-filtration assay under varying salt conditions. To confirm these observations, I think that analysis by both NMR and analytical ultracentrifugation (sedimentation velocity) would provide a consistent link to the assignments already provided by NMR analysis of the autoinhibitory domain and the observations by gel filtration. Crystallography of the high salt (bound) confirmation would be desirable in order to confirm the binding of the autoinhibitory domain to the RFXV motif in the kinase domain and assess whether the autoinhibitory domain may occlude nucleotide binding.

The presence of a separate WNK-specific PF2 domain (WSP) in the C-terminus of the WNK1 kinase is of interest. As mentioned in Chapter 4, this domain was located when a NCBI-BLAST search of the autoinhibitory domain of WNK1 showed homology to that of the OSR-PF2 domain. NMR or crystallography could be used to examine the domain and determine domain boundaries. It will be of interest whether this domain may bind unstructured

RFXV motifs in the C-terminus of WNK1 and regulate substrate binding or whether it may act as a localization factor to other proteins that contain RFXV motifs.

Finally, a long-term investigation of what proteins WNK1 is interacting with in the punctate patterns formed in the cell should be examined. In discussions with the Cobb lab, mere purification of these puncta is not feasible. I think that fluorescent immunostaining of several known large complexes of proteins (such as the WASP/WAVE architecture) would provide an initial direction on further bioinformatic and biochemical analysis of the interaction of WNK1 with other proteins to form these structures. WNK1 is known to have two separate poly-proline motifs which would interact with SH3 domains but it is unknown what the large unstructured region in the C-terminus may interact with. I think that discovering the composition of the puncta will ultimately point toward how the C-terminus plays a role in WNK activity.

This dissertation was typeset with \LaTeX^\dagger by the author.

[†] \LaTeX is a document preparation system developed by Leslie Lamport as a special version of Donald Knuth's \TeX Program.

Appendices

Appendix A

Supplementary Figures for Chapter 1



11200 Rockville Pike
Suite 302
Rockville, Maryland 20852

August 19, 2011

American Society for Biochemistry and Molecular Biology

To whom it may concern,

It is the policy of the American Society for Biochemistry and Molecular Biology to allow reuse of any material published in its journals (the Journal of Biological Chemistry, Molecular & Cellular Proteomics and the Journal of Lipid Research) in a thesis or dissertation at no cost and with no explicit permission needed. Please see our copyright permissions page on the journal site for more information.

Best wishes,

Sarah Crespi

[American Society for Biochemistry and Molecular Biology](#)

11200 Rockville Pike, Rockville, MD

Suite 302

240-283-6616

[JBC](#) | [MCP](#) | [JLR](#)

Tel: 240-283-6600 • Fax: 240-881-2080 • E-mail: asbmb@asbmb.org

Table A.1: WNK1 pHis-parallel Plasmids: X. Min Inventory c. 2004

WNK1 Construct	Start	End	Expression Level	Purification	Crystallization
Wild Type	194	483	Good	Pure	None
S382A	194	483	Good	Pure	Crystal*
S378A	194	483	Good	Pure	None
V318A	194	483	Good	Pure	None
Cluster I Mutant	194	483	Good	Pure	N/D
Cluster II Mutant	194	483	Good	Pure	N/D
Wild Type	209	483	Good	Not Stable	None
S382A	209	483	Good	Not Stable	Crystal
S378A	209	483	Good	Not Stable	Crystal
Wild Type	194	563	Low	Not Stable	None
Wild Type	218	563	Low	Not Stable	None
Wild Type	194	610	Medium	Pure	None
S382A	194	610	Medium	Pure	None
Wild Type	194	660	Good	Pure	None
S382A	194	660	Good	Pure	None
E268Q	194	660	Good	Pure	None
S382A/E268Q	194	660	Good	Pure	None
Wild Type	218	567	Low	N/D	N/D
Wild Type	218	610	Low	N/D	N/D
Wild Type	485	563	Good	Oligomer	No
Wild Type	485	614	Good	Monomer	No

1. Crystal Solved at 1.8Å (Min et al, 2004)

2. In his research, Xioshan Min made 21 separate constructs of the WNK1 kinase. Most of them encompass only the kinase domain-and mutants thereof. However, some of the constructs also include the autoinhibitory domain or are shortened constructs of the individual autoinhibitory domain (Table 1).

Appendix B

Supplementary Figures for Chapter 4

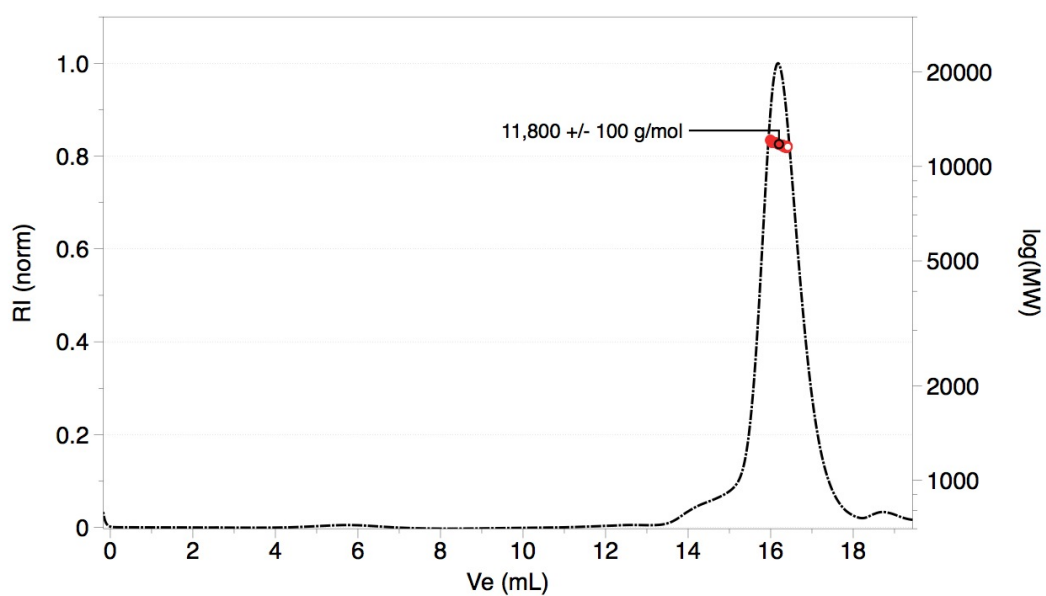


Figure B.1: Chromatographic trace of $U^{13}C,^{15}N$ -WNK1-(480-572) from MALLS analysis. 100L of 5mg/mL autoinhibitory domain was injected onto a S200 (10/300) column and isocratically eluted using a buffer of 10mM Tris pH=6.5, 10mM NaCl, 1mM DTT

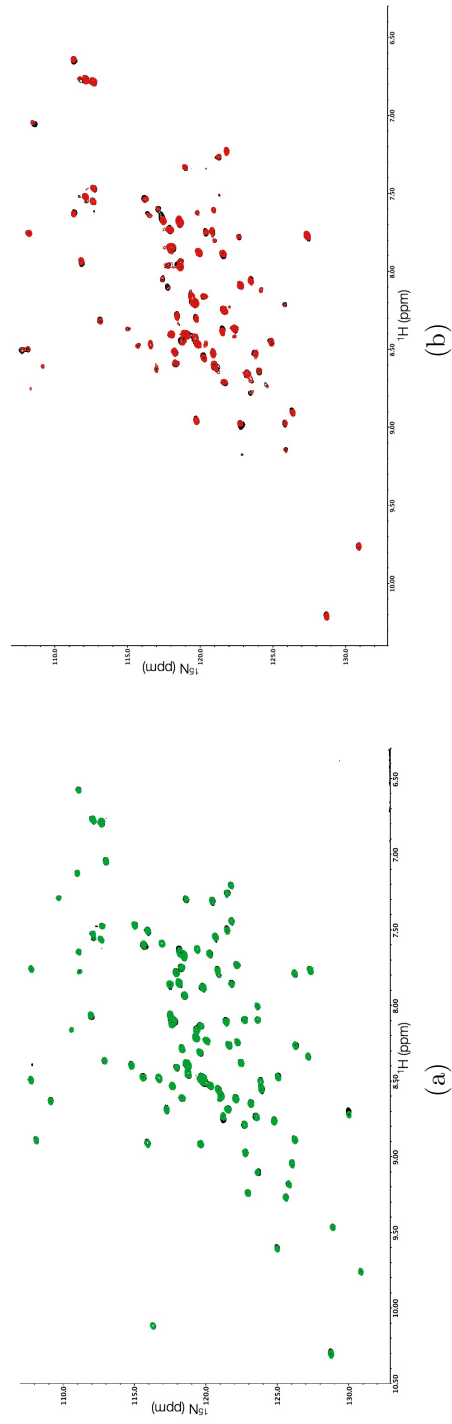


Figure B.2: a) ^1H , ^{15}N -HSQC of WNK1 (480-572) (apo black) titrated with 1 mol. equiv. GAFKV peptide in 10mM NaCl (green) shows that, similar to that of the PF2 domain, the WNK1 autoinhibitory domain primarily associates with the RFXV motif through interaction of the domain with the N-terminal arginine b) ^1H , ^{15}N -HSQC of WNK1 480-572 E539A (apo black) titrated with 1 mol. equiv. GRFKV peptide in 10mM NaCl (red)

Table B.1: Table of Statistics for Structure Calculation of WNK1 (480-572)

<i>Conformational Restraints</i>	
NOE distance restraints	
Total	2399
Unambiguous	1621
Ambiguous	778
Dihedral angle restraints	145
<i>Residual Violations</i>	
Distance Restraints > 0.3Å	1.40±0.96
Distance Restraints > 0.5Å	0
Dihedral Violations > 0.5Å	0
<i>Mean RMSD from Experimental Restraints</i>	
NOE, > 0.3 Å	0.03±0.0008
Dihedral Angles, °	0.18±0.05
<i>Mean RMSD from Idealized Geometry</i>	
Bond Length, Å	0.004
Bond Angle, °	0.52
Improper, °	1.40
<i>Ramachandran Map (%) (PROCHECK-NMR)</i>	
Favorable	87.6
Allowed	11.2
Generously Allowed	0.6
Disallowed	0.6
<i>RMSD (Å) residues 485-570</i>	
Backbone (N, C _α , C')	0.49±0.10
All heavy atoms	1.20±0.10

Appendix C

Supplementary Figures for Chapter 8

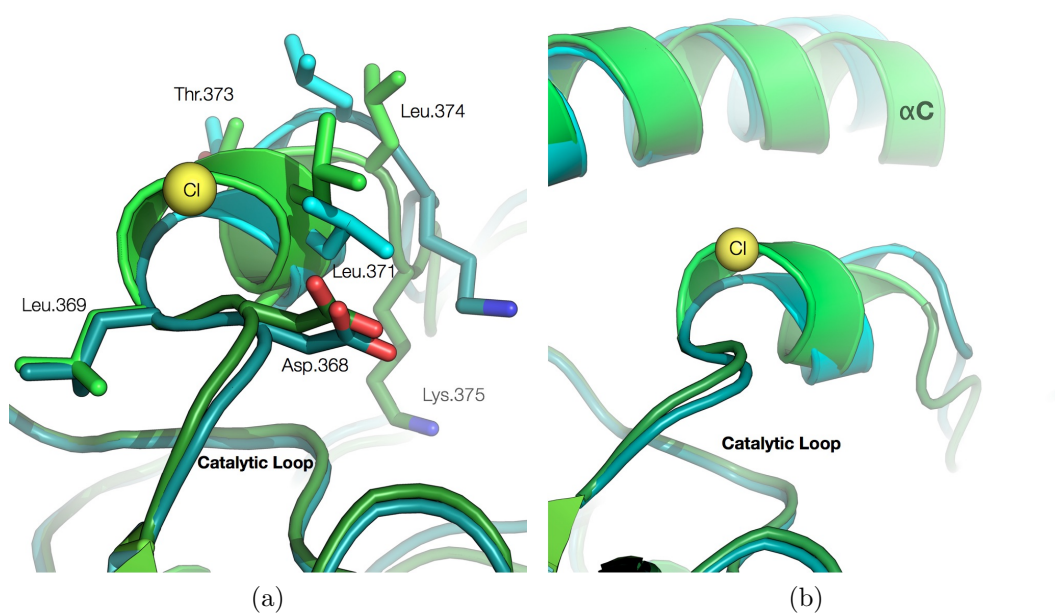
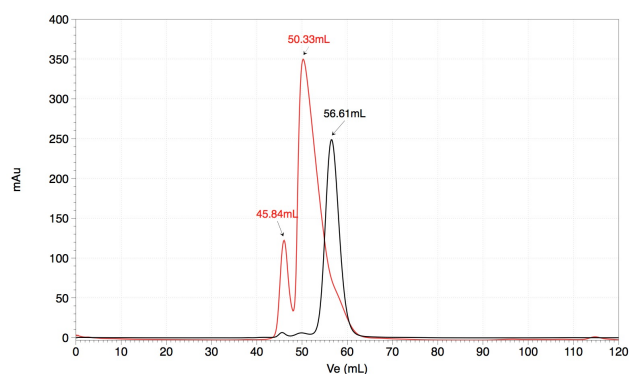


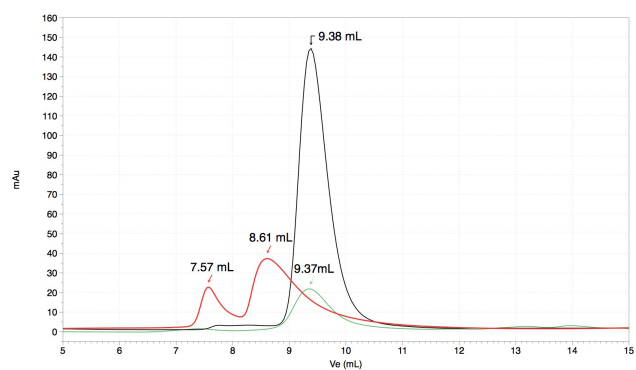
Figure C.1: Comparison of DLG motifs from WNK1 194-483 S382A subunit A (green) and b (cyan) originally determined by Min et al (2004) and re-refined in the presence of chloride ion. The presence of chloride ion is only observed in subunit A.

Appendix D

Supplementary Figures for Chapter 9



(a)



(b)

Figure D.1: a) Gel filtration trace (Superdex 75, 16/60) for WNK1 194-573 in 10 mM NaCl (red) and 100 mM NaCl (black). b) Gel filtration trace (Superdex 75, 10/300) for WNK1 194-573 S378A in 10 mM NaCl (red) and 100 mM NaCl (black). A standard elution profile for the WNK1 kinase domain (194-483 S382A) is shown in green.

Bibliography

- Achilles K, Okabe A, Ikeda M, Shimizu-Okabe C, Yamada J, Fukuda A, Luhmann HJ, Kilb W (2007) Kinetic properties of cl uptake mediated by na+-dependent k+-2cl cotransport in immature rat neocortical neurons. *The Journal of Neuroscience* 27(32):8616–8627
- Adams PD, Afonine PV, Bunkóczi G, Chen VB, Davis IW, Echols N, Headd JJ, Hung LW, Kapral GJ, Grosse-Kunstleve RW, McCoy AJ, Moriarty NW, Oeffner R, Read RJ, Richardson DC, Richardson JS, Terwilliger TC, Zwart PH (2010) Phenix: a comprehensive python-based system for macromolecular structure solution. *Acta Crystallographica Section D* 66(2):213–221
- Akella R, Moon TM, Goldsmith EJ (2008) Unique map kinase binding sites. *Biochimica et Biophysica Acta (BBA) - Proteins and Proteomics* 1784(1):48 – 55
- Altschul SF, Madden TL, Schäffer AA, Zhang J, Zhang Z, Miller W, Lipman DJ (1997) Gapped blast and psi-blast: a new generation of protein database search programs. *Nucleic Acids Research* 25(17):3389–3402
- Anselmo AN, Earnest S, Chen W, Juang YC, Kim SC, Zhao Y, Cobb MH (2006) Wnk1 and osr1 regulate the na+, k+, 2cl cotransporter in hela cells. *Proceedings of the National Academy of Sciences* 103(29):10,883–10,888

- Bax A, Clore GM, Gronenborn AM (1990) 1h-1h correlation via isotropic mixing of ^{13}C magnetization, a new three-dimensional approach for assigning 1h and ^{13}C spectra of ^{13}C -enriched proteins. *Journal of Magnetic Resonance* 88:425–431
- Bhattacharyya RP, Reményi A, Good MC, Bashor CJ, Falick AM, Lim WA (2006a) The ste5 scaffold allosterically modulates signaling output of the yeast mating pathway. *Science* 311(5762):822–826
- Bhattacharyya RP, Reményi A, Yeh BJ, Lim WA (2006b) Domains, motifs, and scaffolds: The role of modular interactions in the evolution and wiring of cell signaling circuits. *Annual Review of Biochemistry* 75(1):655–680
- Bossemeyer D, Engh RA, Kinzel V, Ponstingl H, Huber R (1993) Phosphotransferase and substrate binding mechanism of the camp-dependent protein kinase catalytic subunit from porcine heart as deduced from the 2.0 Å structure of the complex with Mn^{2+} adenylyl imidodiphosphate and inhibitor peptide pki(5-24). *EMBO J* 12(3):849–859
- Cavanagh J, Fairbrother W, Palmer A, Rance M, Skelton N (2007) *Protein NMR Spectroscopy: Principles and Practice*. Elsevier, San Diego
- Chapman ER (2002) Synaptotagmin: A Ca^{2+} sensor that triggers exocytosis? *Nature Reviews Molecular Cell Biology* 3(7):498–508
- Chen VB, Arendall WB III, Headd JJ, Keedy DA, Immormino RM, Kapral GJ, Murray LW, Richardson JS, Richardson DC (2010) *MolProbity: all-*

- atom structure validation for macromolecular crystallography. *Acta Crystallographica Section D* 66(1):12–21
- Chen W, Yazicioglu M, Cobb MH (2004) Characterization of *osr1*, a member of the mammalian *ste20p*/germinal center kinase subfamily. *Journal of Biological Chemistry* 279(12):11,129–11,136
- Cole C, Barber JD, Barton GJ (2008) The jpred 3 secondary structure prediction server. *Nucleic Acids Research* 36(suppl 2):W197–W201
- Collaborative Computational Project N (1994) The ccp4 suite: programs for protein crystallography. *Acta Crystallographica Section D* 50(5):760–763
- Cook KR, Macknight ADC (1984) Effects of medium acetate on cellular volume in rabbit renal cortical slices. *Journal of Physiology* 349:135–156
- Crowther R (1972) *The Molecular Replacement Method*, Gordon and Breach Science Publishers, New York, NY, chap The fast rotation function
- Crowther R, Blow D (1967) A method for positioning a known molecule in an unknown crystal structure. *Acta Crystallographica* 23:544–548
- Delaglio F, Grzesiek S, Vuister GW, Zhu G, Pfeifer J, Bax A (1995) Nmrpipe: A multidimensional spectral processing system based on unix pipes. *Journal of Biomolecular NMR* 6:277–293
- Disse-Nicodème S, Achard JM, Desitter I, Houot AM, Fournier A, Corvol P, Jeunemaitre X (2000) A new locus on chromosome 12p13.3 for pseudo-

- hypoadosteronism type ii, an autosomal dominant form of hypertension. American Journal of Human Genetics 67(2):302–310
- Emsley P, Lohkamp B, Scott WG, Cowtan K (2010) Features and development of coot. Acta Crystallographica Section D 66:486–501
- Gagnon KB, England R, Delpire E (2007) A single binding motif is required for spak activation of the na-k-2cl cotransporter. Cellular Physiology and Biochemistry 20:131–142
- Gardner KH, Kay LE (1998) The use of 2h, 13c, 15n multidimensional nmr to study the structure and dynamics of proteins. Annual Review of Biophysics and Biomolecular Structure 27(1):357–406
- Gedde MM, Davis DK, Huestis WH (1997) Cytoplasmic ph and human erythrocyte shape. Biophysical journal 72(3):1234–1246
- Grant BD, Hemmer W, Tsigelny I, Adams JA, Taylor SS (1998) Kinetic analyses of mutations in the glycine-rich loop of camp-dependent protein kinase. Biochemistry 37(21):7708–7715
- Grzesiek S, Bax A (1992) Correlating backbone amide and side chain resonances in larger proteins by multiple relayed triple resonance nmr. Journal of the American Chemical Society 114(16):6291–6293
- Grzesiek S, Anglister J, Bax A (1993) Correlation of backbone amide and aliphatic side-chain resonances in 13c/15n-enriched proteins by isotropic

- mixing of ^{13}C magnetization. *Journal of Magnetic Resonance, Series B* 101(1):114 – 119
- Grzesiek S, Bax A, Clore GM, Gronenborn AM, Hu JS, Kaufman J, Palmer I, Stahl SJ, Wingfield PT (1996) The solution structure of hiv-1 nef reveals an unexpected fold and permits delineation of the binding surface for the sh3 domain of hck tyrosine protein kinase. *Nature Structural Molecular Biology* 3(4):340–345
- Guggino WB, Stanton BA (2006) New insights into cystic fibrosis: molecular switches that regulate cftr. *Nature Reviews Molecular Cell Biology* 7:426–436
- Hanks S, Hunter T (1995) Protein kinases 6. the eukaryotic protein kinase superfamily: kinase (catalytic) domain structure and classification. *The FASEB Journal* 9(8):576–596
- He G, Wang HR, Huang SK, Huang CL (2007) Intersectin links wnk kinases to endocytosis of romk1. *The Journal of Clinical Investigation* 117(4):1078–1087
- Hoffmann EK, Sjøholm C, Simonsen LO (1983) Na^+ , Cl^- cotransport in ehrlich ascites tumor cells activated during volume regulation (regulatory volume increase). *Journal of Membrane Biology* 76:269–280
- Inglefield JR, Schwartz-Bloom RD (1999) [26] using confocal microscopy and the fluorescent indicator, 6-methoxy-n-ethylquinolinium iodide, to measure

- changes in intracellular chloride. In: Conn PM (ed) *Confocal Microscopy, Methods in Enzymology*, vol 307, Academic Press, pp 469 – 481
- Jeffrey P, Russo A, Polyak K, Gibbs E, Hurwitz J, Massague J, Pavletich N (1995) Mechanism of cdk activation revealed by the structure of a cyclin-cdk2 complex. *Nature* 376(6538):313–320
- Johnston AM, Naselli G, Gonez LJ, Martin RM, Harrison LC, DeAizpurua HJ (2000) Spak, a ste20/sps1-related kinase that activates the p38 pathway. *Oncogene* 19(37):4290–4297
- Kay LE, Ikura M, Tschudin R, Bax A (1990) Three-dimensional triple-resonance nmr spectroscopy of isotopically enriched proteins. *Journal of Magnetic Resonance* (1969) 89(3):496 – 514
- Kramer BK, Bergler T, Stoelcker B, Waldegger S (2008) Mechanisms of disease: the kidney-specific chloride channels clcka and clckb, the barttin subunit, and their clinical relevance. *Nature Clinical Practice Nephrology* 4:38–46
- Kupce E, Nishida T, Freeman R (2003) Hadamard nmr spectroscopy. *Progress in Nuclear Magnetic Resonance Spectroscopy* 42:95–122
- Laskowski RA, Rullmann JAC, MacArthur MW, Kaptein R, Thornton JM (1996) Aqua and procheck-nmr: Programs for checking the quality of protein structures solved by nmr. *Journal of Biomolecular NMR* 8(4):477–486

- Lee BH, Min X, Heise CJ, e Xu B, Chen S, Shu H, Luby-Phelps K, Goldsmith EJ, Cobb MH (2004) Wnk1 phosphorylates synaptotagmin 2 and modulates its membrane binding. *Molecular Cell* 15(5):741 – 751
- Lenertz LY, Lee BH, Min X, Xu Be, Wedin K, Earnest S, Goldsmith EJ, Cobb MH (2005) Properties of wnk1 and implications for other family members. *Journal of Biological Chemistry* 280(29):26,653–26,658
- Lytle C, Forbush B (1996) Regulatory phosphorylation of the secretory na-k-cl cotransporter: modulation by cytoplasmic cl. *American Journal of Physiology - Cell Physiology* 270(2):C437–C448
- Macknight ADC (1985) The role of anions in cellular volume regulation. *Pflugers Archiv* 405:S12–S16
- Manning G, Whyte DB, Martinez R, Hunter T, Sudarsanam S (2002) The protein kinase complement of the human genome. *Science* 298(5600):1912–1934
- Marandi N, Konnerth A, Garaschuk O (2002) Two-photon chloride imaging in neurons of brain slices. *Pflügers Archiv European Journal of Physiology* 445:357–365
- Marion D, Ikura M, Tschudin R, Bax A (1989) Rapid recording of 2d nmr spectra without phase cycling. application to the study of hydrogen exchange in proteins. *Journal of Magnetic Resonance* 85(2):393–399

- McCoy AJ, Grosse-Kunstleve RW, Adams PD, Winn MD, Storoni LC, Read RJ (2007) *Phaser* crystallographic software. *Journal of Applied Crystallography* 40(4):658–674
- Min X (2004) Structural analysis of two protein kinases: Wnk1 and p38 map kinase. Dissertation, The University of Texas Southwestern Medical Center at Dallas, 5323 Harry Hines Blvd. Dallas, TX 75235
- Min X, Lee BH, Cobb MH, Goldsmith EJ (2004) Crystal structure of the kinase domain of wnk1, a kinase that causes a hereditary form of hypertension. *Structure* 12(7):1303 – 1311
- Montelione GT, Lyons BA, Emerson SD, Tashiro M (1992) An efficient triple resonance experiment using carbon-13 isotropic mixing for determining sequence-specific resonance assignments of isotopically-enriched proteins. *Journal of the American Chemical Society* 114(27):10,974–10,975
- Moriguchi T, Urushiyama S, Hisamoto N, Iemura Si, Uchida S, Natsume T, Matsumoto K, Shibuya H (2005) Wnk1 regulates phosphorylation of cation-chloride-coupled cotransporters via the ste20-related kinases, spak and osr1. *Journal of Biological Chemistry* 280(52):42,685–42,693
- Mukherjee S, Ghosh RN, Maxfield FR (1997) Endocytosis. *Physiological Reviews* 77(3):759–803
- Nguyen A, Burack WR, Stock JL, Kortum R, Chaika OV, Afkarian M, Muller WJ, Murphy KM, Morrison DK, Lewis RE, McNeish J, Shaw AS (2002) Ki-

- nase suppressor of ras (ksr) is a scaffold which facilitates mitogen-activated protein kinase activation in vivo. *Molecular and Cellular Biology* 22(9):3035–3045
- Niesen FH, Berglund H, Vedadi M (2007) The use of differential scanning fluorimetry to detect ligand interactions that promote protein stability. *Nat Protocols* 2(9):2212–2221
- Nilges M, Macias MJ, O’Donoghue SI, Oschkinat H (1997) Automated noesy interpretation with ambiguous distance restraints: the refined nmr solution structure of the pleckstrin homology domain from [beta]-spectrin. *Journal of Molecular Biology* 269(3):408 – 422
- Otwinowski Z, Minor W (1997) Processing of x-ray diffraction data collected in oscillation mode. *Methods in Enzymology* 276:307–326
- Painter J, Merritt EA (2006a) Optimal description of a protein structure in terms of multiple groups undergoing tls motion. *Acta Crystallographica Section D* 62(4):439–450
- Painter J, Merritt EA (2006b) Tlsmid web server for the generation of multi-group tls models. *Journal of Applied Crystallography* 39(1):109–111
- Pantoliano MW, Petrella EC, Kwasnoski JD, Lobanov VS, Myslik J, Graf E, Carver T, Asel E, Springer BA, Lane P, Salemme FR (2001) High-density miniaturized thermal shift assays as a general strategy for drug discovery. *Journal of Biomolecular Screening* 6(6):429–440

- Pawson T, Gish GD, Nash P (2001) Sh2 domains, interaction modules and cellular wiring. *Trends in Cell Biology* 11(12):504 – 511
- Pei J, Tang M, Grishin NV (2008) Promals3d web server for accurate multiple protein sequence and structure alignments. *Nucleic Acids Research* 36(suppl 2):W30–W34
- Piechotta K, Lu J, Delpire E (2002) Cation chloride cotransporters interact with the stress-related kinases ste20-related proline-alanine-rich kinase (spak) and oxidative stress response 1 (osr1). *Journal of Biological Chemistry* 277(52):50,812–50,819
- Ponce-Coria J, San-Cristobal P, Kahle KT, Vazquez N, Pacheco-Alvarez D, de los Heros P, Juárez P, Muñoz E, Michel G, Bobadilla NA, Gimenez I, Lifton RP, Hebert SC, Gamba G (2008) Regulation of nkcc2 by a chloride-sensing mechanism involving the wnk3 and spak kinases. *Proceedings of the National Academy of Sciences* 105(24):8458–8463
- Reilly RF, Ellison DH (2000) Mammalian distal tubule: Physiology, pathophysiology, and molecular anatomy. *Physiological Reviews* 80(1):277–313
- Richardson C, Alessi DR (2008) The regulation of salt transport and blood pressure by the wnk-spak/osr1 signalling pathway. *Journal of Cell Science* 121(20):3293–3304
- Rohl CA, Strauss CE, Misura KM, Baker D (2004) Protein structure prediction using rosetta. In: Brand L, Johnson ML (eds) *Numerical Computer*

- Methods, Part D, Methods in Enzymology, vol 383, Academic Press, pp 66–93
- Rothweiler U, Åberg E, Johnson KA, Hansen TE, Jørgensen JB, Engh RA (2011) p38 map kinase dimers with swapped activation segments and a novel catalytic loop conformation. *Journal of Molecular Biology* 411(2):474 – 485
- Rupp B (2009) *Biomolecular Crystallography: Principles, Practice, and Application to Structural Biology*, 1st edn. Garland Science, New York
- Sheffield P, Garrard S, Derewenda Z (1999) Overcoming expression and purification problems of rhogdi using a family of "parallel" expression vectors. *Protein Expression and Purification* 15(1):34 – 39
- Shen Y, Delaglio F, Cornilescu G, Bax A (2009) Talos+: a hybrid method for predicting protein backbone torsion angles from nmr chemical shifts. *Journal of Biomolecular NMR* 44:213–223
- Stein N (2008) Chainsaw: a program for mutating pdb files used as templates in molecular replacement. *Journal of Applied Crystallography* 41:641–643
- Stokes JB (1989) Electroneutral nacl transport in the distal tubule. *Kidney Int* 36(3):427–433
- Strange K, Denton J, Nehrke K (2006) Ste20-type kinases: Evolutionarily conserved regulators of ion transport and cell volume. *Physiology* 21(1):61–68

- Strong M, Sawaya MR, Wang S, Phillips M, Cascio D, Eisenberg D (2006) Toward the structural genomics of complexes: Crystal structure of a pe/ppe protein complex from mycobacterium tuberculosis. *Proceedings of the National Academy of Sciences* 103(21):8060–8065
- Tanoue T, Adachi M, Moriguchi T, Nishida E (2000) A conserved docking motif in map kinases common to substrates, activators and regulators. *Nat Cell Biol* 2(2):110–116
- Tatebayashi K, Takekawa M, Saito H (2003) A docking site determining specificity of pbs2 mapkk for ssk2/ssk22 mapkks in the yeast hog pathway. *EMBO J* 22:3624–3634
- Tu Sw, Bugde A, Luby-Phelps K, Cobb MH (2011) Wnk1 is required for mitosis and abscission. *Proceedings of the National Academy of Sciences* 108(4):1385–1390
- Villa F, Goebel J, Rafiqi F, Deak M, Thastrup J, Alessi DR, van Aalten DM (2007) Structural insights into the recognition of substrates and activators by the osr1 kinase. *EMBO Reports* 8(9):839–845
- Wittekind M, Mueller L (1993) Hncacb, a high-sensitivity 3d nmr experiment to correlate amide-proton and nitrogen resonances with the alpha- and beta-carbon resonances in proteins. *Journal of Magnetic Resonance, Series B* 101(2):201 – 205

- Wöll E, Gschwentner M, Fürst J, Hofer S, Buemberger G, Deetjen P, Paulmichl M, Jungwirth A, Frick J (1996) Fluorescence-optical measurements of chloride movements in cells using the membrane-permeable dye diI₁-meq. *Pflügers Archiv European Journal of Physiology* 432:486–493
- Xia Y, Yee A, Arrowsmith C, Gao X (2003) 1h_c and 1h_n total noe correlations in a single 3d nmr experiment. 15n and 13c time-sharing in t1 and t2 dimensions for simultaneous data acquisition. *Journal of Biomolecular NMR* 27:193–203
- Xie X, Gu Y, Fox T, Coll JT, Fleming MA, Markland W, Caron PR, Wilson KP, Su MSS (1998) Crystal structure of jnk3: a kinase implicated in neuronal apoptosis. *Structure* 6(8):983 – 991
- Xu Be, English JM, Wilsbacher JL, Stippec S, Goldsmith EJ, Cobb MH (2000) Wnk1, a novel mammalian serine/threonine protein kinase lacking the catalytic lysine in subdomain ii. *Journal of Biological Chemistry* 275(22):16,795–16,801
- Xu Be, Min X, Stippec S, Lee BH, Goldsmith EJ, Cobb MH (2002) Regulation of wnk1 by an autoinhibitory domain and autophosphorylation. *Journal of Biological Chemistry* 277(50):48,456–48,462
- Yang CL, Liu X, Paliege A, Zhu X, Bachmann S, Dawson DC, Ellison DH (2007) Wnk1 and wnk4 modulate cftr activity. *Biochemical and Biophysical Research Communications* 353(3):535 – 540

Zagorska A, Pozo-Guisado E, Boudeau J, Vitari AC, Rafiqi F, Thastrup J, Deak M, Campbell DG, Morrice NA, Prescott AR, Alessi DR (2006) Regulation of activity and localization of the wnk1 protein kinase by hyperosmotic stress. *Journal of Cell Biology* 176(1):89–100

Zheng J, Trafny EA, Knighton DR, Xuong N, Taylor SS, Ten Eyck LF, Sowadski JM (1993) 2.2 Å refined crystal structure of the catalytic subunit of cAMP-dependent protein kinase complexed with MnATP and a peptide inhibitor. *Acta Crystallographica Section D* 49(3):362–365